The Dissertation Committee for Corey I Ostrove
certifies that this is the approved version of the following dissertation:

Entanglement in Superconducting Heterostructures, and Quantum Circuit Simulation Hardware

Committee:

Linda E. Reichl, Supervisor

Brian R. La Cour

Scott Aaronson

Andrew Potter

Keji Lai

Entanglement in Superconducting Heterostructures, and Quantum Circuit Simulation Hardware

by

Corey I Ostrove

DISSERTATION

Presented to the Faculty of the Graduate School of

The University of Texas at Austin

in Partial Fulfillment

of the Requirements

for the Degree of

DOCTOR OF PHILOSOPHY

THE UNIVERSITY OF TEXAS AT AUSTIN

May 2021

Dedicated in loving memory to my father, Richard Ostrove.

Acknowledgments

I'm incredibly grateful to the many people who have helped me along this journey and brought me to this point in my career. There's no way I could possibly do justice in such a small space to all of the profound ways you've all helped and supported me over these past few years, but I will do my best nonetheless. To my partner, Victoria, the patience, love and support that you've given me throughout my time here at UT has kept me grounded and focused on my goals even during challenging times. I am grateful to my family: my mother Gail, brother Bryan, sister Elyse and stepmother Elizabeth. You've been a constant source of support and care throughout my time at graduate school (and throughout the rest of my life), and I'm not sure I'd have been able to achieve what I have without that love and support. I'm grateful for the many loving memories I have of my father, Richard. While you aren't around to read this, you always made it known that you were proud of me, and the memories of these moments has helped me continue moving forward throughout many challenging times.

I'm grateful to my advisor, Prof. Linda Reichl, for the mentorship she has provided throughout my time at UT. You've shown incredible patience these past five years and have helped me grow in innumerable ways as a researcher and scientist. I've consistently watched you go to bat for me and your other students and advocate on our behalf whenever we've needed it, and this has shaped my own understanding of mentorship and made clear my own desire to act as one for others during my career. I'm grateful to my former supervisor Dr. Brian La Cour for his mentorship throughout my time working at ARL:UT and beyond. The opportunity you gave me as a fledging PhD student to work with you and the many research experiences I had at ARL:UT helped open up the career path in quantum information theory I am currently on. It's not an exaggeration to say that I wouldn't be where I am today if not for my experiences working with you at ARL:UT. I'm grateful to Prof. Scott Aaronson for so graciously welcoming me as a regular attendee and affiliate of the quantum information theory group in the CS department and for the many opportunities he has given me over these past few years to collaborate on teaching and educational projects. The opportunities I've had to collaborate and discuss research with so many brilliant researchers on "the other side of the field" has made me a better rounded quantum information researcher and wouldn't have been possible otherwise.

A special thanks goes out to the members of my dissertation committee: Prof. Linda Reichl, Dr. Brian La Cour, Prof. Scott Aaronson, Prof. Andrew Potter and Prof. Keji Lai. I appreciate you all taking the time to patiently review this dissertation and your participation in the final oral defense process.

Finally, I'd like to thank the many friends and colleagues I've made throughout my time in graduate school. I'd like to especially acknowledge my friends and colleagues: Behzat Ergun, Maxwell Porter, Alex Jentsch, Joshua Nietzl, Ace Furman and Patrick Rall. Be it via board game nights, late-night nerd sniping, or general commiseration, you've all helped make these past seven years memorable and fun. I've grown immensely as a researcher as a result of countless conversations with and presentations from my colleagues at UT and UT:ARL, and the results of these conversations are often reflected directly in this dissertation. I would like to especially acknowledge (in no particular order): James Troupe, Andrew Lanham, Michael Starkey, Travis Cuvelier, Granville Ott, Hans Mark, Maxwell Porter, Behzat Ergun, Patrick Rall, Daniel Liang, William Kretschmer, Prof. Andrew Potter, Prof. Shyam Shankar, Jason Pollack, Andrea Rocchetto, Noah Davis, Thomas Wong, Nai-Hui Chia and Yosi Atia, along with countless others, for the many interesting discussions (research-based or otherwise) we've had and I hope to continue having.

Entanglement in Superconducting Heterostructures, and Quantum Circuit Simulation Hardware

Publication No. ____________________

Corey I Ostrove, Ph.D.
The University of Texas at Austin, 2021

Supervisor: Linda E. Reichl

We begin this dissertation by studying noise correlations in superconducting heterostructures of various geometries. In recent years there has been a resurgence of interest in the nonlocal transport properties of superconducting heterostructures due to the possibility of their serving as a source of electronic entanglement in solid state quantum information processors. Devices designed for this purpose are called Cooper pair splitting devices. The utility of these devices as entanglement sources is known to have connections to the positivity of noise cross correlations in spatially separated leads. In Chapter 1 we outline the theoretical prerequisites for this work, outlining the scattering theory framework based on the Bogoliubov-de Gennes equations we adopt. Within this framework we apply a methodology first introduced by Demers and by Blonder, Tinkham and Klapwijk (BTK) in the early 1980s to find the scattering matrix for our superconducting structures. The current, local and nonlocal shot noise can all be expressed in terms of the underlying scattering processes. This framework allows us to investigate the behavior of the current and noise correlations in the structure as we change the geometry and other key system parameters such as the system size, superconducting phase difference and temperature. We also introduce the Andreev approximation, a commonly used approximation which simplifies the scattering theory for superconducting heterostructures.

In Chapter 2, we study the local and nonlocal shot noise in a quasi-1D normal-superconducting-normal (NSN) geometry using material parameters relevant to high-T_c superconductivity. The scattering and shot noise distributions are studied in the short, intermediate and long system size limits, allowing us to examine the qualitative differences in these three parameter regimes. This allows us to, for example, identify the signatures of over-the-gap geometric resonances in the shot noise distributions that appear in the long system size limit. We also break the nonlocal shot noise distributions down further and study the individual contributions to the nonlocal shot due to particle-particle, hole-hole and particle-hole scattering processes.

In Chapter 3, we extend our investigation of superconducting heterostructures to the more complicated NSNSN geometry. A novel feature introduced in the geometry is the presence of subgap quasibound states, which show up as resonances in the scattering matrix. We show that these quasibound states dramatically impact the nonlocal shot noise distributions in the system. At energies near the quasibound states the dominant transmission channel through the system is a process called particle-hole transmission, which results in sharp positive peaks in the nonlocal shot noise distribution of the system. The behavior of the nonlocal noise correlations as we change the size of the superconducting and normal regions is investigated and it is found that there is a “sweet spot” with respect to the size of the superconducting regions that maximizes the positivity of the nonlocal noise distributions as well as a periodic-like behavior in the positivity of the noise distributions with respect to the normal region size. The results of the full scattering theory for the NSNSN geometry are compared to the results obtained using the Andreev approximation, where we find that the Andreev approximation breaks down at energies close to the quasibound state energies.

In the second half of this dissertation we focus on work related to the development of a prototype special-purpose quantum circuit simulation device based on commercial off-the-shelf high-speed analog signal processing hardware. In Chapter 4 we introduce the embedding scheme used to represent quantum states and quantum gates in the frequency domain of a classical analog voltage signal. Experimental results are presented from an early two-qubit prototype device for the fidelity of the state generation and gate application circuits. In Chapter 5, a more in-depth investigation into the modeling of classical errors within our signal processing based simulation method is performed in terms of the effects this noise has on the results of the quantum computation being simulatied. It is shown, for example, that additive white gaussian noise (AWGN) in our system has the same effect as applying a depolarizing channel to the qubits in the simulation. We then perform a simulation of a simple quantum error correction (QEC) protocol using the device and show that, even in the presence of classical noise in the simulation hardware, an overall enhancement in the performance of gate operations as a result of applying QEC is observed.

Table of Contents

List of Tables

List of Figures

Part I

Noise and Bound States in Superconducting Heterostructures

Chapter 1

Introduction

1.1 Introduction

The potential for superconductors to serve as a source of entangled electron pairs in solid state devices has led to a resurgence in interest in the study of superconducting heterostructures in recent years [20, 46, 53, 100, 116]. The key observation is that the Cooper pairs underlying superconductivity naturally form maximally entangled pairs of electrons, which if spatially separated (say in separate leads of a superconducting heterostructure) would enable these electrons to be used for quantum information processing tasks. Superconducting heterostructures designed with this purpose in mind are referred to as Cooper pair splitters (CPS). With the rapid development of superconducting quantum information processors, there is a need to revisit the dynamical properties of superconducting heterostructures in the context of their applications to the development of these devices.

The usefulness of superconductors as an entanglement source is limited by the ability to spatially separate the entangled electrons comprising the Cooper pairs and thus is determined by the spatially nonlocal transport properties of the structure, which couple different normal metal leads in the system [28]. The primary mechanism responsible for the creation of entangled electron pairs in NSN structures is the crossed Andreev reflection (CAR) process, in which a particle or hole impinges on the superconducting region in one lead and is transmitted as a hole or particle, respectively, in the other lead [18, 28]. An important measure for entanglement generation in these structures, the Cooper pair splitting efficiency η, can be related to the strength of this process in relation to the other non-entanglement generating processes such as specular reflection and normal transmission of particles or holes [20]. Because of this, much of the existing research on CPS has focused on designing architectures that enhance the prevalence of CAR. Proposals include using double quantum dots (QD) [20, 26, 51], spin filtering using ferromagnetic leads [38], anomolous scattering in graphene [17,24,55] and energy filtering in semiconductors [116]. Experimentally, extensive progress has been made with QD-based devices [44, 52]. Additionally, these proposals are not necessarily mutually exclusive, and theoretical and experimental progress has been made with CPS devices that use a combination of double QD and either ferromagnetic leads or external magnetic fields [21, 45, 111, 112, 119].

Alternatively, it is possible to relate the efficiency of formation of entangled pairs to the nonlocal shot noise spectrum of the structure, which is one of the focuses in this paper [23, 46]. As a result of the interest in Cooper pair splitter design, a large amount of work has been done theoretically (see for example, [20, 43, 47, 116, 122]) and experimentally (see [51, 52, 100]) to characterize the nonlocal properties of various NSN structures. Most of this work so far has focused on standard s-wave BCS superconductors, but some theory has also been worked out for systems with anisotropic order parameters [46, 89], such as HTS, and for structures which incorporate quantum Hall edge channels [54].

In this dissertation we adopt the scattering theory framework for quantum electronic transport, developed by Landauer [70] and Buttiker [22]. We make use of an adaptation of this scattering theory approach using the Bogoliubov-de Gennes equations [35] in order to incorporate inelastic scattering processes due to interactions with superconducting regions. Our methods are adapted from the techniques introduced by Demers and Griffin, and Blonder, Tinkham and Klapwijk (BTK) [16, 35, 36]. We obtain exact expressions both with and without the Andreev approximation [7] for the scattering matrix, current, and both local and nonlocal shot noise. Using these expressions, we obtain numerical results for NSN and NSNSN heterostructures using parameters for based on the high-T_c superconductor (HTS) LSCO. The basis of the Andreev approximation is dropping higher order terms in the ratio of the superconducting gap energy Δ_0 and the

Fermi energy E_F from the Bogoliubov-de Gennes equations. Our use of the superconductor LSCO as our model material in the numerics presented in this paper amplifies the differences observed between the full scattering theory and the Andreev approximation in the cross-correlated shot noise distributions because it has a relatively large value of Δ_0/E_F.

High temperature cuprate superconductors (HTS) were discovered in 1986 [12] and, in the decades since, a substantial amount of experimental and theoretical development has occurred regarding the electronic transport properties of these materials [58, 108, 109, 113]. These materials typically have order parameters with d-wave symmetry. Extensive experimental work has been performed on studying mesoscopic d-wave superconductor structures (a review of which can be found in [107]). Additional experimental studies have probed current fluctuations and, in particular, the relation between shot noise and junction bias in mesoscopic d-wave structures [29, 30, 91]. These shot noise studies find strong agreement with the theoretical predictions derived in [6], which were based on the scattering matrix approach. Additional theoretical work on shot noise in d-wave superconductors can be found in [33] and a general review of shot noise in mesoscopic systems can be found in [15].

Building devices using HTS can be challenging, in part due to the difficulty of growing high quality single crystals at the nanoscale. Additionally, dimension limited superconductivity presents its own challenges in the form of dissipative finite-size effects [72, 81], which require substantially lower temperatures to operate at these scales. In recent years, advances in fabrication techniques and HTS material science have enabled the manufacture of high quality single crystal nanowires. These nanowires allow for the study of dimensionality-limited superconductivity with the smallest of the nanowires operating in the quasi 1-d limit. Applications have been proposed for using superconducting nanowire devices in the field of quantum sensing, including those based on superconducting qubit architectures. Typical superconducting qubit devices are constructed using standard Josephson junctions formed from superconductor-insulator-superconductor (SIS) structures

[117]. However, devices have also been constructed by instead using SNS junctions formed by semiconductor nanowires [71, 74], due to their ability to operate at higher magnetic field strengths. Superconducting cuprate nanowires have a number of potential advantages in application areas such as this due to their very high critical magnetic field strengths. Moreover, superconducting nanowire-based devices have been used in proposals to improve the quantum efficiency of single photon detectors [11] and for improving the flux sensitivity of SQUIDs, again due to their high critical magnetic field strengths and small coherence lengths [9,102]. Of all of the HTS, the most effort has been applied to the manufacturing and characterization of nanoscale YBCO ($\mathrm{YBa_2Cu_3O_{7-x}}$). The state of the art for YBCO nanowire size is $\sim$ 10nm [121]. Nanowires of this size are on the order of the coherence length for YBCO, $\xi = 3.4$ nm [118], and smaller than the magnetic penetration depth of $\lambda = 26$nm [118]. In addition to YBCO, nanowires with widths as small as 80nm have been constructed from LSCO ($\mathrm{La_{2-x}Sr_xCuO_4}$) [77] as well as nanowires with widths between 400-600nm for BSCCO ($\mathrm{Bi_2(Sr, La)_2CuO_y}$) [41]. These dimensions are still at least an order of magnitude larger than the coherence length, but it is conceivable that it will be possible within the next few years to reliably construct nanowires with sizes on the order of the coherence length for a number of cuprate HTS.

In Chapter 2 we study the NSN geometry. The full scattering matrix is calculated (the corresponding scattering coefficients are given in Appendix A) without the Andreev approximation and these are used to generate energy distributions for the thermally averaged current. We generate contour plots of the local and nonlocal shot noise and find evidence of electron bunching in both the local and nonlocal noise. The dependence of the total nonlocal shot noise and the individual contributions due to hole-hole, particle-particle and particle-hole interactions is plotted as a function of the system size and as a function of applied bias.

In Chapter 3 we study the NSNSN geometry and find that there is a one-to-one correspondence between the energies of the quasibound states in this system and the regions of positivity in the cross-correlated shot noise energy distribution. We also find that this connection is robust and persists in the presence of multiple quasibound states and for a wide range of system sizes. Moreover, we analyze the noise cross-correlations for the NSN geometry and find that, in contrast to the NSNSN geometry, the total cross-correlated shot noise distribution remains negative over the entire sub-gap energy range of the system. The results for the NSNSN geometry using the full scattering theory are compared to those obtained using the Andreev approximation, and we find that there is a large deviation between the behavior of the cross-correlations at the quasibound state energies.

The remainder of this chapter is organized as follows. In Section 1.2.1, we review the Bogoliubov-de Gennes theory of the superconductor as it applies to superconducting heterostructures. In Section 1.2.2, we describe the scattering theory used to obtain exact expressions for the scattering amplitudes for the NSN and NSNSN systems. In Section 1.2.3.1, we derive the field operators for excitations in the normal regions of the system and include the effect of scattering from the superconducting regions and use this to obtain the expression for the current through the normal regions. In Section 1.2.3.2, we give exact expressions for the local and nonlocal shot noise. Finally, in Section 1.3, we discuss the model material parameters used for the numerics in this work.

1.2 Theoretical Methods

1.2.1 The Bogoliubov-de Gennes Equations

Within the superconductor, the energy eigenstates in real-space are given by solutions to the Bogoliubov-de Gennes equations,

$$\begin{pmatrix} -\frac{\hbar^2\nabla^2}{2m} - E_F & \Delta(\vec{r}) \\ \Delta^*(\vec{r}) & \frac{\hbar^2\nabla^2}{2m} + E_F \end{pmatrix} \begin{pmatrix} u(\vec{r}) \\ v(\vec{r}) \end{pmatrix} = e \begin{pmatrix} u(\vec{r}) \\ v(\vec{r}) \end{pmatrix}, \tag{1.1}$$

Consider a system with a spatially varying gap potential, for example the heterostructure described in Figure 1.1. One commonly used model for the spatial variation of the gap function is a step function potential,

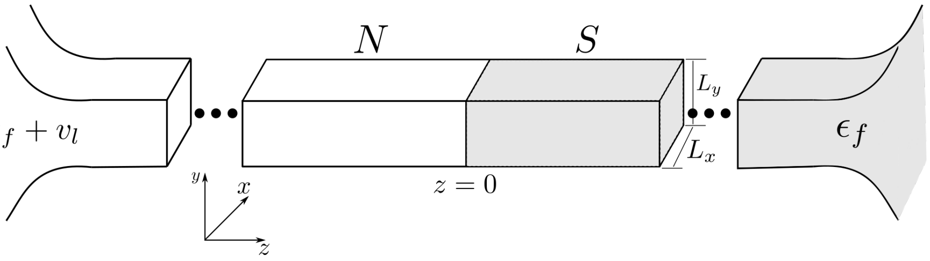

Figure 1.1: The NS junction geometry is among the simplest possible superconducting heterostructures, and we will use it an a guiding example in developing the formalism of the Bogoliubov-de Gennes equations and BTK scattering theory. In Chapters 2 and 3 we will introduce the more complicated NSN and NSNSN geometries studied in this dissertation. The left and right leads are are connected to thermal reservoirs with Fermi energy ϵ_f. We will allow for an additional bias of v_l to be applied to the left lead. More details on the system parameters can be found in Section 1.3 and Table 1.1.

as shown in Equation 1.2. While the step function model in general does not satisfy the self-consistency requirements imposed by BCS theory, it is a common first approximation that works well in many systems. The validity of this step function approximation is addressed in detail in [76] and [61].

$$\Delta(\vec{r}) = \begin{cases} \Delta(z) & z < 0 \\ 0 & z > 0 \end{cases} \tag{1.2}$$

While we will restrict ourselves to the step function model above, previous theoretical work has been done in order to understand the effect self-consistently solving for the superconducting gap function has on the predicted behavior of superconducting heterostructures. Some of the earliest work on this was performed by McMillan, who used Green's function methods to calculate the first-order corrections to the step-function approximation and proposed an experiment using a SNIS structure to experimentally probe the spatial structure of the self-consistent gap function [82]. In [115], van Son, van Kempen and Wyder utilized a qualitative model for the gap function at an NS interface and found that the softening of the discontinuity in the gap function resulted in a dampening of geometrical oscillations in the transmission through an NINS tunnel junction. Martin and Lambert self-consistently calculated the gap function for the NSN structure and used this result along with a transfer matrix based approach to calculate corrections to the differential conductance of the system [80]. The authors found substantial corrections to the differential conductance of the self-consistent NSN system for bias voltages comparable to, and larger than, the maximum gap energy Δ_0, with additional structure at supergap biases directly associated with a gradient in the superconducting phase of the central S region introduced by the self-consistency requirement. Comparable findings to those of Martin and Lambert were found in a series of works by Sánchez-Cañizares and Sols [97–99].

The general strategy for tackling the step function scattering problem is to first solve the bulk BdG equations in each of the layers separately and to then apply the appropriate boundary conditions to stitch together a complete solution. For materials with s-wave symmetry order parameters, the gap function $\Delta(\vec{r})$ reduces to $\Delta_0 e^{i\phi}$ (with Δ_0 real-valued) inside of the superconductor, where $e^{i\phi}$ is the complex phase of the superconductor. The Bogoliubov-de Gennes equations, assuming no magnetic fields or external potential are present, and with an s-wave superconductor, are given by

$$\epsilon u(\vec{r}) = \left[-\frac{\hbar^2}{2m}\vec{\nabla}^2 - \epsilon_f\right] u(\vec{r}) + \Delta_0 e^{i\phi} v(\vec{r}), \tag{1.3}$$

$$\epsilon v(\vec{r}) = \left[\frac{\hbar^2}{2m}\vec{\nabla}^2 + \epsilon_f\right] v(\vec{r}) + \Delta_0 e^{-i\phi} u(\vec{r}), \tag{1.4}$$

where ϵ is the excitation energy and u and v are the spatially varying coherence factors. We then try the trial solution

$$\begin{pmatrix} u(\vec{r}) \\ v(\vec{r}) \end{pmatrix} = \begin{pmatrix} u \\ v e^{i\varphi} \end{pmatrix} e^{i\vec{k}_s \cdot \vec{r}} \tag{1.5}$$

Plugging this into the BdG equations we get

$$\epsilon u e^{i\vec{k}_s\cdot\vec{r}} = \left[-\frac{\hbar^2}{2m}\vec{\nabla}^2(ue^{i\vec{k}_s\cdot\vec{r}}) - \epsilon_f e^{i\vec{k}_s\cdot\vec{r}}\right] + \Delta_0 e^{2i\varphi} v e^{i\vec{k}_s\cdot\vec{r}}, \tag{1.6}$$

$$\epsilon v e^{i\varphi} e^{i\vec{k}_s\cdot\vec{r}} = \left[\frac{\hbar^2}{2m}\vec{\nabla}^2(ve^{i\vec{k}_s\cdot\vec{r}}) + \epsilon_f v e^{i\vec{k}_s\cdot\vec{r}}\right] + \Delta_0 e^{-i\varphi} u e^{i\vec{k}_s\cdot\vec{r}}, \tag{1.7}$$

Next we evaluate the derivatives in Equations 1.6 and 1.7.

$$\epsilon u e^{i\vec{k}_s\cdot\vec{r}} = \frac{\hbar^2}{2m}|\vec{k}_s|^2 u e^{i\vec{k}_s\cdot\vec{r}} - \epsilon_f u e^{i\vec{k}_s\cdot\vec{r}} + \Delta_0 e^{2i\varphi} v e^{i\vec{k}_s\cdot\vec{r}} \tag{1.8}$$

$$\epsilon v e^{i\varphi} e^{i\vec{k}_s\cdot\vec{r}} = \frac{\hbar^2}{2m}|\vec{k}_s|^2 v e^{i\vec{k}_s\cdot\vec{r}} + \epsilon_f v e^{i\vec{k}_s\cdot\vec{r}} + \Delta_0 e^{-i\varphi} u e^{i\vec{k}_s\cdot\vec{r}} \tag{1.9}$$

We can now divide through by $e^{i\vec{k}_s\cdot\vec{r}}$.

$$\epsilon u = \frac{\hbar^2}{2m}|\vec{k}_s|^2 u - \epsilon_f u + \Delta_0 e^{2i\varphi} v \tag{1.10}$$

$$\epsilon v e^{i\varphi} = \frac{\hbar^2}{2m}|\vec{k}_s|^2 v(\theta) + \epsilon_f v + \Delta_0 e^{-i\varphi} u \tag{1.11}$$

Rearranging the above equations we get a linear system to solve, which in matrix form is

$$\begin{pmatrix} \frac{\hbar^2|\vec{k}_s|^2}{2m} - \epsilon_f - \epsilon & \Delta_0 e^{2i\varphi} \\ \Delta_0 e^{2i\varphi} & -\frac{\hbar^2|\vec{k}_s|^2}{2m} + \epsilon_f - \epsilon \end{pmatrix} \begin{pmatrix} u \\ v \end{pmatrix} = 0 \tag{1.12}$$

First, in order to solve for the energy spectrum of the quasiparticle excitation, ϵ, we use the solvability criterion that the determinant of the matrix in Equation 1.12 is zero. This yields the secular equation in Equation 1.13,

$$(\xi - \epsilon)(\xi + \epsilon) + \Delta_0^2 = 0, \tag{1.13}$$

where $\xi = \frac{\hbar^2|\vec{k}_s|^2}{2m} - \epsilon_f$. Solving this for ϵ yields the quasiparticle energy spectrum

$$\epsilon = \sqrt{\xi^2 + \Delta_0^2}, \tag{1.14}$$

where by convention we have taken the quasiparticle energies to be positive. Next we solve for the coherence factors u and v. To do so, we first impose a normalization condition on the coherence factors $u^2 + v^2 = 1$. Taking the first equation of 1.12 and using the normalization condition to eliminate v yields

$$(\xi - \epsilon)u + \Delta_0 e^{2i\varphi}\sqrt{1 - u^2} = 0. \tag{1.15}$$

Solving this equation for u we obtain

$$u = \sqrt{\frac{1}{2}\left(1 + \frac{\xi}{\epsilon}\right)}. \tag{1.16}$$

Likewise, following the same procedure but starting with the second equation in Equation 1.12, we obtain

$$v = \sqrt{\frac{1}{2}\left(1 - \frac{\xi}{\epsilon}\right)}. \tag{1.17}$$

Finally, in order to complete our description of the bulk s-wave order parameter solution we would like to solve for the dispersion relation relating the wavevectors of the plane-wave solutions to the quasiparticle excitation energy. This is done by rearranging the quasiparticle excitation spectrum in Equation 1.14 in terms of ξ,

$$\epsilon^2 = \xi^2 + \Delta_0^2 \rightarrow \xi = \pm\sqrt{\epsilon^2 - \Delta_0^2}. \tag{1.18}$$

Next the definition $\xi = \frac{\hbar^2|\vec{k}_s|^2}{2m} - \epsilon_f$ is substituted in and we solve for $\vec{k}_s$,

$$\vec{k}_s = \pm\sqrt{k_f^2 \pm \frac{2m}{\hbar^2}\sqrt{\epsilon^2 - \Delta_0^2}}. \tag{1.19}$$

We associate with particle-like excitations the solution with the "+" sign inside of the square root in Equation 1.19 and the "−" sign with hole-like quasiparticles. We will later adopt the notation of labeling magnitude of $\vec{k}_s$ as k_p^α for particle-like excitations and k_h^α for hole-like excitations, where α is used to label various regions within the heterostructures.

1.2.2 Scattering Theory Approach to Superconducting Heterostructures

To demonstrate the scattering theory approach to superconducting transport we begin here with the simple case of a normal-superconductor (NS) interface with a single transverse mode, with each region connected to their own respective thermal reservoirs, as shown in Figure 1.1. Let us assume that both particles and holes are incident from the left and particle-like and hole-like excitations from the right. The state in the left normal region, $\psi_L(z)$, and the right superconductor region, $\psi_S(z)$, are respectively

$$\begin{aligned}
\psi_N(z) &= \frac{A_N^p}{\sqrt{q_p^N}}\begin{bmatrix} 1 \\ 0 \end{bmatrix} \mathrm{e}^{iq_p^N z} + \frac{B_N^h}{\sqrt{q_h^N}}\begin{bmatrix} 0 \\ 1 \end{bmatrix} \mathrm{e}^{-iq_h^N z} \\
&\qquad + \frac{C_N^p}{\sqrt{q_p^N}}\begin{bmatrix} 1 \\ 0 \end{bmatrix} \mathrm{e}^{-iq_p^N z} + \frac{D_N^h}{\sqrt{q_h^N}}\begin{bmatrix} 0 \\ 1 \end{bmatrix} \mathrm{e}^{+iq_h^L z}, \\
\psi_S(z) &= \frac{A_S^p}{\sqrt{k_p}}\begin{bmatrix} u \\ v \end{bmatrix} \mathrm{e}^{ik_p z} + \frac{B_S^h}{\sqrt{k_h}}\begin{bmatrix} v \\ u \end{bmatrix} \mathrm{e}^{-ik_h z} \\
&\qquad + \frac{C_S^p}{\sqrt{k_p}}\begin{bmatrix} u \\ v \end{bmatrix} \mathrm{e}^{-ik_p z} + \frac{D_S^h}{\sqrt{k_h}}\begin{bmatrix} v \\ u \end{bmatrix} \mathrm{e}^{+ik_h z},
\end{aligned} \tag{1.20}$$

where (in atomic units, where $\hbar$, the electron mass m_e and the electron charge e_c all equal 1) $q_\beta^N = \sqrt{2m_N^*\left(e \pm \epsilon_F^N\right)}$ with $\beta = p, h$, and where we use the upper sign for particles and the lower sign for holes.

The choice of normalization in Equation 1.20 ensures that our system carries unit current [13]. Next we need to apply the appropriate boundary conditions in order to connect the wavefunctions for the normal and superconducting regions. We are working in the high transparency limit and so we require continuity of the wavefunctions and the derivatives at $z = 0$,

$$\psi_N(0) = \psi_S(0), \quad {\psi'}_N(0) = {\psi'}_S(0). \tag{1.21}$$

The above boundary conditions give a system of four equations which can be used in order to solve for the coefficients of outgoing excitations in terms of the coefficients of the incoming excitations. That is, we solve for the coefficients $C_N^p,\ D_N^h,\ A_S^p,\ B_S^h$ as functions of the coefficients $A_N^p,\ B_N^h,\ C_S^p,\ D_S^h$. This gives the matrix equation

$$\begin{pmatrix} C_N^p \\ D_N^h \\ A_S^p \\ B_S^h \end{pmatrix} = \begin{pmatrix} r_{pp}^{LL} & r_{ph}^{LL} & t_{pp}^{LR} & t_{ph}^{LR} \\ r_{hp}^{LL} & r_{hh}^{LL} & t_{hp}^{LR} & t_{hh}^{LR} \\ t_{pp}^{RL} & t_{ph}^{RL} & r_{pp}^{RR} & r_{ph}^{RR} \\ t_{hp}^{RL} & t_{hh}^{RL} & r_{hp}^{RR} & r_{hh}^{RR} \end{pmatrix} \begin{pmatrix} A_N^p \\ B_N^h \\ C_S^p \\ D_S^h \end{pmatrix}. \tag{1.22}$$

The subscripts and superscripts in the scattering elements above are read from right to left and denote the incoming and outgoing excitation types and leads respectively. In Appendix A we give expressions for the scattering matrix elements for the NSN geometry studied in Chapter 2. Unfortunately, the analytical expressions for the full scattering coefficients for the NSNSN system without the Andreev approximation are far too long to likewise include in print. In any case, we will be focusing mainly on numerical results for the NSN and NSNSN geometries in the following chapters.

A common approximation made when studying scattering through superconducting heterostructures is the Andreev approximation [7]. By including the boundary conditions on the derivatives of the wavefunctions, we are working outside of the Andreev approximation. A more detailed discussion of this point can be found in Section 1.2.4.

1.2.3 Local and Nonlocal Shot Noise

1.2.3.1 Field Operators and Current

Let us now consider the derivation of the local and nonlocal shot noise through a superconducting heterostructure in terms of the underlying scattering processes. To begin, we will need the electron field operator for excitations in the normal system. The left normal lead depicted in Figure 1.1 has a length of L_L and is connected to a reservoir with Fermi energy ϵ_f. For simplicity, we assume that the left normal lead has a rectangular cross-section with infinitely hard walls. The field operator for excitations in the left lead can be written as a two-component spinor

$$\hat{\psi}_{N_L}(x, y, z, t) = \begin{pmatrix} \hat{\psi}^p_{N_L} \\ \hat{\psi}^h_{N_L} \end{pmatrix}, \tag{1.23}$$

where

$$\hat{\psi}^p_{N_L} = \int dE e^{-iEt/\hbar} \sum_{\nu} \phi^L_{\nu}(x, y) \sqrt{\frac{m}{2\pi\hbar^2 q^N_{p\nu}(E)}} \left[\hat{a}_{L\nu p}(E) e^{iq^N_{p\nu}(E)z} + \hat{b}_{L\nu p}(E) e^{-iq^N_{p\nu}(E)z}\right] \tag{1.24}$$

and

$$\hat{\psi}^h_{N_L} = \int dE e^{iEt/\hbar} \sum_{\nu} \phi^L_{\nu}(x, y) \sqrt{\frac{m}{2\pi\hbar^2 q^N_{h\nu}(E)}} \left[\hat{a}_{L\nu h}(E) e^{-iq^N_{h\nu}(E)z} + \hat{b}_{L\nu h}(E) e^{iq^N_{h\nu}(E)z}\right]. \tag{1.25}$$

Here $\nu = \{n_x, n_y\}$ denotes the transverse modes, and

$$\phi_{\nu}(x, y) = \frac{2}{\sqrt{\mathrm{L}_x \mathrm{L}_y}} \sin\left(\frac{n_x \pi x}{L_x}\right) \sin\left(\frac{n_y \pi y}{L_y}\right) \tag{1.26}$$

is the normalized wave function for the transverse modes [6]. We assume that $L_L \gg L_x > L_y$. The annihilation operators, $\hat{a}_{\alpha,\nu,\beta}(E)$, annihilate an excitation of type $\beta \in \{p, h\}$ in the α^{th} normal lead ($\alpha \in$

$\{L, R\}$), in the ν^{th} transverse channel and with energy E, with the same convention used for the creation operators. The operator $\hat{b}_{\alpha\nu\beta}(E)$ is short hand for the set of annihilation operators associated with excitations in the α^{th} lead that travel towards the reservoir, either due to reflection or because they are transmitted from the other reservoir. For holes our convention for the energy label denotes how far below the Fermi energy the excitation is, and thus is a positive value. We assume that no impurities are present that can couple different transverse channels. Below we will include all of the different scattering channels that give rise to excitations moving in the $-z$ direction.

Rewriting the operator $\hat{b}_{L\nu p}(E)$ in terms of scattering processes giving rise to left-moving particles yields

$$\hat{b}_{L\nu p}(E) = r_{pp}^{LL}(E,\nu)\hat{a}_{L\nu p}(E) + r_{ph}^{LL}(E,\nu)\hat{a}_{L\nu h}(E) + t_{pp}^{LR}(E,\nu)\hat{a}_{R\nu p}(E) + t_{ph}^{LR}(E,\nu)\hat{a}_{R\nu h}(E). \tag{1.27}$$

More generally we can write

$$\hat{b}_{i\nu\beta}(E) = r_{\beta\beta}^{ii}(E,\nu)\hat{a}_{i\nu\beta}(E) + r_{\beta\beta'}^{ii}(E,\nu)\hat{a}_{i\nu\beta'}(E) + t_{\beta\beta}^{ij}(E,\nu)\hat{a}_{j\nu\beta}(E) + t_{\beta\beta'}^{ij}(E,\nu)\hat{a}_{j\nu\beta'}(E), \tag{1.28}$$

where $j = R$ when $i = L$ and vice-versa, and where $\beta' = h$ when $\beta = p$ and vice-versa. In anticipation of the later restriction to a single transverse mode, and given our assumption about the lack of impurities coupling different transverse modes, we will drop the mode label ν wherever it does not lead to confusion. With this we can rewrite the field operators in Equations 1.24 and 1.25 in terms of the individual scattering processes as shown below.

$$\hat{\psi}^p_{N_L} = \int dE e^{-iEt/\hbar} \sqrt{\frac{m_L}{2\pi\hbar^2 q^N_p(E)}} \Big[\hat{a}_{Lp}(E) e^{iq^N_p(E)z} + r^{LL}_{pp}(E)\hat{a}_{Lp}(E) e^{-iq^N_p(E)z} + r^{LL}_{ph}(E)\hat{a}_{Lh}(E) e^{-iq^N_p(E)z}$$
$$+ t^{LR}_{pp}(E)\hat{a}_{Rp}(E) e^{-iq^N_p(E)z} + t^{LR}_{ph}(E)\hat{a}_{Rh}(E) e^{-iq^N_p(E)z}\Big] \tag{1.29}$$

$$\hat{\psi}^h_{N_L} = \int dE e^{iEt/\hbar} \sqrt{\frac{m_L}{2\pi\hbar^2 q^N_h(E)}} \Big[\hat{a}_{Lh}(E) e^{-iq^N_h(E)z} + r^{LL}_{hh}(E)\hat{a}_{Lh}(E) e^{iq^N_h(E)z} + r^{LL}_{hp}(E)\hat{a}_{Lp}(E) e^{iq^N_h(E)z}$$
$$+ t^{LR}_{hh}(E)\hat{a}_{Rh}(E) e^{iq^N_h(E)z} + t^{LR}_{hp}(E)\hat{a}_{Rp}(E) e^{iq^N_h(E)z}\Big] \tag{1.30}$$

Given the field operator $\hat{\psi}_{N_L}(z,t)$ for the left lead, we can write the corresponding current operator for the left lead using the relation

$$\hat{J}_L(z,t) = \frac{\hbar e_c}{2im_L}\bigg(\hat{\psi}^\dagger_{N_L}(z,t)\frac{d\hat{\psi}_{N_L}(z,t)}{dz} - \frac{d\hat{\psi}^\dagger_{N_L}(z,t)}{dz}\hat{\psi}_{N_L}(z,t)\bigg), \tag{1.31}$$

where e_c is the electron charge and m_L is the effective mass of electrons in the left lead. In order to obtain the local and nonlocal shot noise we will also need the thermal average of the current operator. Plugging the expressions for the particle and hole field operators from Equations 1.29 and 1.30 into Equation 1.31 and taking the thermal averages yields

$$\begin{aligned}\langle J_L\rangle = \frac{\mathrm{e}}{h}\int de\ \bigg(&N^L_p(1-|r^{LL}_{pp}|^2) - N^L_h(1-|r^{LL}_{hh}|^2) + N^R_h\ |t^{LR}_{hh}|^2 + N^L_p\ |r^{LL}_{hp}|^2\\ &+ N^R_p\ |t^{LR}_{hp}|^2 - N^L_h\ |r^{LL}_{ph}|^2 - N^R_h\ |t^{LR}_{ph}|^2 - N^R_p\ |t^{LR}_{pp}|^2\bigg).\end{aligned} \tag{1.32}$$

The symbol $\langle\cdot\rangle$ denotes the thermal averaging operation, $\langle A\rangle = \mathrm{Tr}(A\rho)$, where A is some Hermitian operator and ρ is the finite-temperature density matrix for the system. In the above expressions $N^\alpha_\gamma = \langle\hat{a}^{\alpha\dagger}_{e,\gamma}\hat{a}^\alpha_{e,\gamma}\rangle = (1+\mathrm{e}^{\beta(e+\mathrm{sgn}(\gamma)v_\alpha)})^{-1}$, is the Fermi distribution for the thermal reservoir of excitations of type γ connected to lead α, where $\gamma\in\{p,h\}$. β is the standard inverse temperature parameter, $\beta = \frac{1}{k_BT}$, with k_B being the

Boltzmann constant and T the temperature of the system. We define $\mathrm{sgn}(\gamma) = +1$ for $\gamma = p$, $\mathrm{sgn}(\gamma) = -1$ for $\gamma = h$ and $F_\gamma^\alpha = 1 - N_\gamma^\alpha$. We use here the convention of assigning holes positive energy (measured with respect to the Fermi energy), so at zero-bias both electrons and holes have the same thermal distributions, but are shifted in opposite directions in the presence of an applied bias [89]. The average current is zero if the Fermi energies in the left and right reservoirs are equal. However, if the chemical potentials are different in the two reservoirs, there will be a net current flow.

1.2.3.2 Local and Nonlocal Shot Noise Expressions

The shot noise in the left lead is given by the correlation function of fluctuations about the average current in the left lead at different times,

$$S^{LL}(z, y; t, s) = \langle (J_L(z,t) - \langle J_L(z,t)\rangle)(J_L(y,s) - \langle J_L(y,s)\rangle)\rangle. \tag{1.33}$$

We call this the "local" shot noise because it only involves current fluctuations in the left lead. If only the zero frequency limit of this correlation function is kept, we obtain the zero frequency component of the local shot noise

$$S_{tot}^{LL}(\omega = 0) = \int dE\ dS^{LL}(E) = \mathrm{S}_{pp}^{LL} + \mathrm{S}_{hh}^{LL} + \mathrm{S}_{ph}^{LL}. \tag{1.34}$$

In Equation 1.34 we have separated the shot noise into three components, the first two of which, S_{pp}^{LL} and S_{hh}^{LL}, give the contribution to the local shot noise due to correlations between particles and holes, respectively. The third term, S_{ph}^{LL}, gives the contribution to the local shot noise due to correlations between particles and holes in the left lead. These three types of contributions to the local shot noise can be computed explicitly and are given by the following:

$$\begin{aligned}
\mathrm{S}_{pp}^{LL} = \frac{m_L^2}{\pi^2}\int dE \Bigg[& F_p^L\ N_p^L\ (1+2|r_{hp}^{LL}|^2 - 2|r_{pp}^{LL}|^2 - 2|r_{pp}^{LL}|^2|r_{hp}^{LL}|^2 + |r_{pp}^{LL}|^4 + |r_{hp}^{LL}|^4) + F_p^R\ N_p^R\ (|t_{pp}^{LR}|^2 - |t_{hp}^{LR}|^2)^2 \\
&+ (F_p^R\ N_p^L + F_p^L N_p^R)\ (|r_{pp}^{LL}|^2|t_{pp}^{LR}|^2 + |r_{hp}^{LL}|^2|t_{hp}^{LR}|^2 - 2\mathrm{Re}[t_{hp}^{LR*} r_{hp}^{LL} r_{pp}^{LL*} t_{pp}^{LR}])\ \Bigg],
\end{aligned} \tag{1.35}$$

$$\begin{aligned}
\mathrm{S}_{hh}^{LL} = \frac{m_L^2}{\pi^2}\int dE \Bigg[& F_h^L\ N_h^L\ (1-2|r_{hh}^{LL}|^2 + 2|r_{ph}^{LL}|^2 - 2|r_{hh}^{LL}|^2|r_{ph}^{LL}|^2 + |r_{hh}^{LL}|^4 + |r_{ph}^{LL}|^4) + F_h^R\ N_h^R\ (|t_{ph}^{LR}|^2 - |t_{hh}^{LR}|^2)^2 \\
&+ (F_h^R\ N_h^L + F_h^L N_h^R)\ (|t_{ph}^{LR}|^2|r_{ph}^{LL}|^2 + |t_{hh}^{LR}|^2|r_{hh}^{LL}|^2 - 2\mathrm{Re}[t_{ph}^{LR*} r_{ph}^{LL} r_{hh}^{LL*} t_{hh}^{LR}])\ \Bigg],
\end{aligned} \tag{1.36}$$

$$\begin{aligned}
\mathrm{S}_{ph}^{LL} = \frac{m_L^2}{\pi^2}\int dE \Bigg[& (F_p^L\ N_h^L + F_h^L\ N_p^L)\ (|r_{ph}^{LL}|^2|r_{pp}^{LL}|^2 + |r_{hp}^{LL}|^2|r_{hh}^{LL}|^2 - 2\mathrm{Re}[r_{pp}^{LL*} r_{ph}^{LL} r_{hh}^{LL*} r_{hp}^{LL}]) \\
&+ (F_p^R\ N_h^R + F_h^R\ N_p^R)\ (|t_{ph}^{LR}|^2|t_{pp}^{LR}|^2 + |t_{hh}^{LR}|^2|t_{hp}^{LR}|^2 - 2\mathrm{Re}[t_{ph}^{LR*} t_{pp}^{LR} t_{hp}^{LR*} t_{hh}^{LR}]) \\
&+ (F_p^R\ N_h^L + F_h^L N_p^R)\ (|r_{ph}^{LL}|^2|t_{pp}^{LR}|^2 + |r_{hh}^{LL}|^2|t_{hp}^{LR}|^2 - 2\mathrm{Re}[r_{ph}^{LL*} t_{pp}^{LR} t_{hp}^{LR*} r_{hh}^{LL}]) \\
&+ (F_p^L\ N_h^R + F_h^R N_p^L)\ (|t_{ph}^{LR}|^2|r_{pp}^{LL}|^2 + |t_{hh}^{LR}|^2|r_{hp}^{LL}|^2 - 2\mathrm{Re}[t_{ph}^{LR*} r_{pp}^{LL} r_{hp}^{LL*} t_{hh}^{LR}])\ \Bigg].
\end{aligned} \tag{1.37}$$

The cross correlated shot noise is the symmetrized correlation function for fluctuations about the average current at different times and between the left and right leads,

$$\begin{aligned}
S^{LR}(z,y;t,s) = \frac{1}{2}\Big\langle &(\hat{J}_L(z,t) - \langle\hat{J}_L\rangle)(\hat{J}_R(y,s) - \langle\hat{J}_R\rangle) \\
&+ (\hat{J}_R(y,s) - \langle\hat{J}_R\rangle)(\hat{J}_L(z,t) - \langle\hat{J}_L\rangle)\Big\rangle.
\end{aligned} \tag{1.38}$$

Due to its connection to entanglement generation, the main quantity of interest we will explore in this dissertation is the zero frequency limit of the Fourier transformed cross-correlated shot noise [28], which we write as

$$\mathrm{S}_{tot}^{LR} \equiv \int dE\ dS^{LR}(E) = \mathrm{S}_{pp}^{LR} + \mathrm{S}_{hh}^{LR} + \mathrm{S}_{ph}^{LR}. \tag{1.39}$$

As with the local shot noise, S_{tot}^{LR} naturally decomposes into three components, S_{pp}^{LR}, S_{hh}^{LR} and S_{ph}^{LR}, which are respectively the contributions due to correlations between particles in the left and right leads, holes in the left and right leads, and between particles in the left lead and holes in the right lead (and vice-versa), respectively. The expressions for S_{pp}^{LR}, S_{hh}^{LR} and S_{ph}^{LR} in terms of the scattering matrix elements can be written

$$
\begin{aligned}
\mathrm{S}_{pp}^{LR} = \frac{m_L m_R}{\pi^2} \int dE \Big[& F_p^L N_p^L \big((-|r_{hp}^{LL}|^2 + |r_{pp}^{LL}|^2 - 1)\ (-|t_{hp}^{RL}|^2 + |t_{pp}^{RL}|^2) \big) \\
& + F_p^R N_p^R \big((-|r_{hp}^{RR}|^2 + |r_{pp}^{RR}|^2 - 1)(-|t_{hp}^{LR}|^2 + |t_{pp}^{LR}|^2) \big) \\
& + (F_p^L N_p^R + F_p^R N_p^L) \big(\mathrm{Re}\left[r_{hp}^{LL} r_{hp}^{RR} t_{hp}^{LR*} t_{hp}^{RL*} \right] - \mathrm{Re}\left[r_{hp}^{LL*} r_{pp}^{RR*} t_{pp}^{RL} t_{hp}^{LR} \right] \\
& + \mathrm{Re}\left[r_{pp}^{LL} r_{pp}^{RR} t_{pp}^{LR*} t_{pp}^{RL*} \right] - \mathrm{Re}\left[r_{pp}^{LL*} r_{hp}^{RR*} t_{hp}^{RL} t_{pp}^{LR} \right] \big) \Big]
\end{aligned}
\tag{1.40}
$$

$$
\begin{aligned}
\mathrm{S}_{hh}^{LR} = \frac{m_L m_R}{\pi^2} \int dE\ \Big[& F_h^L N_h^L \big((|r_{hh}^{LL}|^2 - |r_{ph}^{LL}|^2 - 1)(|t_{hh}^{RL}|^2 - |t_{ph}^{RL}|^2) \big) \\
& + F_h^R N_h^R \big((|r_{hh}^{RR}|^2 - |r_{ph}^{RR}|^2 - 1)(|t_{hh}^{LR}|^2 - |t_{ph}^{LR}|^2) \big) \\
& + (F_h^L N_h^R + F_h^R N_h^L)\ \big(\mathrm{Re}\left[r_{hh}^{LL} r_{hh}^{RR} t_{hh}^{LR*} t_{hh}^{RL*} \right] - \mathrm{Re}\left[r_{hh}^{LL*} r_{ph}^{RR*} t_{ph}^{RL} t_{hh}^{LR} \right] \\
& + \mathrm{Re}\left[r_{ph}^{LL} r_{ph}^{RR} t_{ph}^{LR*} t_{ph}^{RL*} \right] - \mathrm{Re}\left[r_{ph}^{LL*} r_{hh}^{RR*} t_{hh}^{RL} t_{ph}^{LR} \right] \big)\ \Big]
\end{aligned}
\tag{1.41}
$$

$$
\begin{aligned}
\mathrm{S}_{ph}^{LR} = \frac{m_L m_R}{\pi^2} \int dE \Big[& (F_h^L N_p^L + F_p^L N_h^L) \big(\mathrm{Re}\left[r_{hh}^{LL} r_{hp}^{LL*} t_{hp}^{RL} t_{hh}^{RL*} \right] - \mathrm{Re}\left[r_{hh}^{LL} r_{hp}^{LL*} t_{ph}^{RL*} t_{pp}^{RL} \right] \\
& - \mathrm{Re}\left[r_{ph}^{LL} r_{pp}^{LL*} t_{hh}^{RL*} t_{hp}^{RL} \right] + \mathrm{Re}\left[r_{ph}^{LL} r_{pp}^{LL*} t_{pp}^{RL} t_{ph}^{RL*} \right] \big) \\
& + (F_h^R N_p^R + F_p^R N_h^R)\ \ \big(\mathrm{Re}\left[r_{hh}^{RR} r_{hp}^{RR*} t_{hp}^{LR} t_{hh}^{LR*} \right] - \mathrm{Re}\left[r_{hh}^{RR} r_{hp}^{RR*} t_{ph}^{LR*} t_{pp}^{LR} \right] \\
& - \mathrm{Re}\left[r_{ph}^{RR} r_{pp}^{RR*} t_{hh}^{LR*} t_{hp}^{LR} \right] + \mathrm{Re}\left[r_{ph}^{RR} r_{pp}^{RR*} t_{pp}^{LR} t_{ph}^{LR*} \right]\ \big) \\
& + (F_h^L N_p^R + F_p^R N_h^L)\ \big(\mathrm{Re}\left[r_{hh}^{LL} r_{hp}^{RR} t_{hp}^{LR*} t_{hh}^{RL*} \right] - \mathrm{Re}\left[r_{hh}^{LL*} r_{pp}^{RR*} t_{ph}^{RL} t_{hp}^{LR} \right] \\
& + \mathrm{Re}\left[r_{ph}^{LL} r_{pp}^{RR} t_{pp}^{LR*} t_{ph}^{RL*} \right] - \mathrm{Re}\left[r_{ph}^{LL*} r_{hp}^{RR*} t_{hh}^{RL} t_{pp}^{LR} \right] \big) \\
& + (F_p^L N_h^R + F_h^R N_p^L)\ \big(\mathrm{Re}\left[r_{hp}^{LL} r_{hh}^{RR} t_{hh}^{LR*} t_{hp}^{RL*} \right] - \mathrm{Re}\left[r_{hp}^{LL*} r_{ph}^{RR*} t_{pp}^{RL} t_{hh}^{LR} \right] \\
& + \mathrm{Re}\left[r_{pp}^{LL} r_{ph}^{RR} t_{ph}^{LR*} t_{pp}^{RL*} \right] - \mathrm{Re}\left[r_{pp}^{LL*} r_{hh}^{RR*} t_{hp}^{RL} t_{ph}^{LR} \right] \big)\ \Big]
\end{aligned}
\tag{1.42}
$$

The quantities dS_{α}^{LR} give the energy distributions of these terms.

1.2.4 The Andreev Approximation

We have so far discussed only the full scattering theory and thus far have not looked at the effect of applying the Andreev approximation [7]. The Andreev approximation can be used if the ratio between the gap energy Δ_0 and the Fermi energy E_F, $\frac{\Delta_0}{E_F}$, is sufficiently small. Then, to good approximation, we can drop higher order terms in the ratio $\frac{\Delta_0}{E_F}$ from the BdG equations. Doing so reduces the pair of coupled second order differential equations in Equation 1.1 to a pair of coupled first-order differential equations known as the Andreev equations,

$$\begin{pmatrix} -i\hbar v_F \cdot \nabla & \Delta(\mathbf{r}) \\ \Delta^*(\mathbf{r}) & i\hbar v_F \cdot \nabla \end{pmatrix} \begin{pmatrix} u(\mathbf{r}) \\ v(\mathbf{r}) \end{pmatrix} = e \begin{pmatrix} u(\mathbf{r}) \\ v(\mathbf{r}) \end{pmatrix}, \tag{1.43}$$

where v_f is the Fermi velocity.

Under the Andreev approximation the quasiparticle dynamics of the system are governed by a pair of coupled first order differential equations, and the boundary conditions connecting the different regions reduce to just the continuity of the wavefunctions at the boundary. In the high-transparency limit we consider here, this gives $r_{pp}^{LL} = r_{hh}^{LL} = r_{pp}^{RR} = r_{hh}^{RR} = 0$ as well as $t_{hp}^{LR} = t_{ph}^{LR} = t_{hp}^{RL} = t_{hp}^{RL} = 0$ in the scattering matrix (with the remaining scattering elements modified accordingly). The simplest way to solve for the scattering coefficients under the Andreev approximation is to treat each of the different processes for injecting excitations into the system from each of the thermal reservoirs independently.

As an example of how the calculation of the scattering coefficients with the Andreev approximation proceeds, let us demonstrate by looking at the scattering process in the NSN geometry (see Figure 2.1) in which we have a particle emitted from the left thermal reservoir impinging upon the NS interface in the left-lead and calculate r_{hp}^{LL} and t_{pp}^{RL}. For this process the wavefunction in the left lead is

$$\psi_{N_L}(z) = \begin{bmatrix} 1 \\ 0 \end{bmatrix} \mathrm{e}^{iq_p^N z} + r_{hp}^{LL} \begin{bmatrix} 0 \\ 1 \end{bmatrix} \mathrm{e}^{+iq_h^L z}. \tag{1.44}$$

Next we write the wavefunction in the superconducting region for this process,

$$\psi_S(z) = A_S^p \begin{bmatrix} u \\ v \end{bmatrix} \mathrm{e}^{ik_p z} + D_S^h \begin{bmatrix} v \\ u \end{bmatrix} \mathrm{e}^{+ik_h z}. \tag{1.45}$$

In the superconducting region transmitted electrons from the left normal lead can only couple to electron-like excitations. Backward propagating hole-like excitations in the superconducting region arise due to Andreev reflection at the second NS interface with the right normal lead. Finally, the wavefunction in the right normal lead for this process is given by

$$\psi_{N_R}(z) = t_{pp}^{RL} \begin{bmatrix} 1 \\ 0 \end{bmatrix} \mathrm{e}^{iq_p^N z}. \tag{1.46}$$

We next apply the continuity conditions at each of the interfaces,

$$\psi_L(0) = \psi_S(0), \quad \psi_S(h) = \psi_R(h), \tag{1.47}$$

which gives is a system of four equations,

$$\begin{aligned} 1 &= A_S^p u + D_S^h v, & r_{hp}^{LL} &= A_S^p v + D_S^h u, \\ t_{pp}^{RL} e^{iq_p^N h} &= A_S^p u e^{ik_p h} + D_S^h v e^{+ik_h h}, & 0 &= A_S^p v e^{ik_p h} + D_S^h u e^{+ik_h h}. \end{aligned} \tag{1.48}$$

With a bit of algebra, these four equations can be used to eliminate the coefficients in the superconducting region A_S^p and D_S^h, and to solve for r_{hp}^{LL} and t_{pp}^{RL}. The resulting scattering coefficients are

$$\begin{aligned} r^{LL}_{hp} &= \frac{(e^{ik_h h} - e^{ik_p h})uv}{e^{ik_h h}u^2 - e^{ik_p h}v^2} \\ t^{RL}_{pp} &= \frac{e^{ih(k_h + k_p - q^N_p)}}{e^{ik_h h}u^2 - e^{ik_p h}v^2} \end{aligned} \tag{1.49}$$

Note that this approach, starting from the Andreev equations and then solving for the scattering matrix using just the continuity of the wavefunctions at the interface, appears to be different than the approach described in the original BTK paper [16], which starts from the full scattering matrix of the system and takes the limit $q^\alpha_p = q^\alpha_h = k^\alpha_p = k^\alpha_h = k_F$, where α is a placeholder for the various region labels. We have found, by direct calculation, that using the BTK approach gives results exactly identical to those found using the Andreev equations directly as we did above. Perhaps the key advantage of applying the Andreev approximation is that it vastly simplifies the resulting expressions for the scattering coefficients and noise. For example, when using the full set of boundary conditions for the NSNSN system described in Chapter 3, we can obtain exact expressions for the scattering matrix elements, but these expressions turn out to be so large as to make printing them impractical. With the Andreev approximation applied it is possible to write down the explicit expressions for the scattering elements, and they are given in Appendix B along with the simplified cross-correlated shot noise.

1.3 Model System Material Parameters

In this work we restrict ourselves to the quasi-1D limit and as such only consider the first propagating channel of the waveguide [43, 46]. Our choice of model system parameters is guided by two aims, the first of which is to select a set of realistic material parameters which allow for transport in the quasi-1D limit. This will allow us to avoid the additional complications of dealing with multiple transverse modes and any potential coupling between different modes. Additionally, later on in Chapter 3 one of our goals will be to compare the results for the NSNSN geometry using the full scattering theory to those obtained using the

Andreev approximation in the presence of quasibound states. The basis of the Andreev approximation is dropping higher order terms in the ratio of the superconducting gap energy Δ_0 and the Fermi energy ϵ_f from the Bogoliubov-de Gennes equations. As such, it is desirable to select model materials that have a relatively large value of Δ_0/ϵ_f. One family of materials with many members satisfying both of these properties are high-T_c cuprate superconductors, and this is the family of materials we will base our model system on for our numerics. We express all quantities in atomic units, where $\hbar$, the electron mass m_e and the electron charge e_c all equal 1. With these choices, energy is measured in Hartrees, E_H, with $E_H \approx 27.2eV$ and length is measured in Bohr radii, $a_B \approx 0.53\text{Å}$.

Let us consider some typical high-T_c materials. The gap in cuprates is anisotropic and can vary greatly depending on orientation [79, 105]. As an approximation we use estimates for the maximum gap value (for $\theta = 0$) based on BCS theory. The BCS estimate of the superconducting gap is $\Delta_0 = 1.77 k_B T_c$, where k_B is Boltzmann's constant. In atomic units this is

$$\Delta_0 = \left(5.572{\times}10^{-6}\ \frac{E_h}{K}\right) T_c, \tag{1.50}$$

where T_c is measured in Kelvins. The Fermi velocity is

$$v_f = \xi\pi\Delta_0 = \left(1.75{\times}10^{-5}\ \frac{E_h}{K}\right) \xi T_c, \tag{1.51}$$

where the coherence length, ξ, is measured in atomic units. The Fermi energy is

$$\epsilon_f = \frac{1}{2} m^* v_f^2 = \left(1.532{\times}10^{-10}\ \frac{E_h}{K^2}\right)\ m^* \xi^2 T_c^2, \tag{1.52}$$

where m^* is the effective mass. We will fix the Fermi energy such that it lies at the center of the energy interval defined by the first propagating channel in the waveguide. We will also assume that $L_x = 1.2 L_y$, so the second transverse channel opens along the x-direction. The value of L_y can be determined from the condition that

$$\epsilon_f = \frac{1}{2}(E_{1,1} + E_{2,1}) = \frac{1}{4m^*}\left(5\left(\frac{\pi}{1.2L_y}\right)^2 + 2\left(\frac{\pi}{L_y}\right)^2\right). \tag{1.53}$$

If we use Equation 1.52, we obtain

$$L_y = \frac{2.97{\times}10^5}{m^*\xi T_c}\ a_B{\cdot}K. \tag{1.54}$$

We can now evaluate these quantities for several known high T_c superconducting materials, where for simplicity we will take the effective mass $m^* = 1$ in all three materials. As mentioned above, we also want to set our parameters such that the transport is restricted to just the first transverse mode of the system. We achieve this by setting a cutoff energy, $\epsilon_{\max}$, which is simply the energy at which the second transverse mode opens measured with respect to the Fermi energy, $E^{tr}_{2,1}$. The transverse energy for the mode (n_x, n_y) is given by $E^{tr}_{n_x,n_y} = \frac{\hbar^2}{2m^*}\left(\frac{n_x^2\pi^2}{L_x^2} + \frac{n_y^2\pi^2}{L_y^2}\right)$. The Fermi distribution for particles and holes is $N_p(E) = N_h(E) = (1 + \mathrm{e}^{E/k_BT})^{-1}$. To ensure confinement to the first transverse mode, let us require that $(1 + \mathrm{e}^{\delta_0\epsilon_{\max}/(k_BT_0)})^{-1} = 0.001$, so the distribution of particles and holes has decayed to approximately zero at the cutoff energy, and then solve for the corresponding temperature T_0. Values for all these parameters for a variety of high-T_c materials are given in Table 1.1.

The system size is small enough and temperature low enough that electron transport in the quasi-1D wire is assumed to be ballistic. We also assume that a phase difference of ϕ can be induced between the superconducting segments, although this is not essential for our main results.

For the results presented in Chapters 2 and 3 we will use the the superconductor $La_{2-x}Sr_xCuO_4$ (LSCO) as our model material. For LSCO the temperature of the system, T_0, is 16.3K and the maximum

Material	$YBa_2Cu_3O_{7-x}$(a)	$La_{1.45}Nd_{0.4}Sr_{0.15}CuO_{4+\delta}$(a)	$Nd_{1.85}Ce_{0.15}CuO_{4-\delta}$(a)
T_c (K)	88.8	24	26.2
ξ (a_B)	64.3	91	101
Δ (E_H)	0.000495	0.000134	0.000146
ϵ_f (E_H)	0.00499	0.000726	0.00107
$\epsilon_{\max}$ (E_H)	0.00190	0.000276	0.000406
L_y (a_B)	52	136.4	113
T_0 (K)	43.4	6.32	9.28

Material	$La_{2-x}Sr_xCuO_4$ (b)	$Bi_2(Sr, La)_2CuO_y$ (a)	$Y_{0.9}Ca_{0.1}Ba_2Cu_3O_y$ (a)
T_c (K)	38	28.3	80.6
ξ (a_B)	65	76	64
Δ (E_H)	0.000212	0.000158	0.00045
ϵ_f (E_H)	0.000935	0.000701	0.00411
$\epsilon_{\max}$ (E_H)	0.000356	0.000267	0.00156
L_y (a_B)	120	139	57
T_0 (K)	16.3	6.1	35.8

Table 1.1: Cuprate materials with coherence length of order of the width of the nanowire. The temperature T_0 allows the Fermi distribution to spread over the entire energy range up to $\epsilon_{\max}$. Based on data for T_c and ξ from (a) [118], Table 9.1 and (b) [34], Table 7.4.

energy $\epsilon_{\max}$ is $.000356E_H$. The Fermi distribution of the thermal reservoirs at this temperature is shown in Figure 1.2.

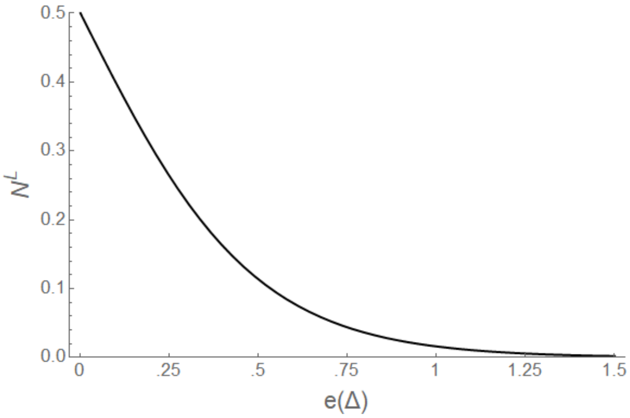

Figure 1.2: Plot of the Fermi distribution, N^L, with zero bias and $T_0 = 16.3K$. Energy is measured in units of the gap energy of LSCO.

Chapter 2

Local and Nonlocal Noise in the NSN High-Tc Nanowire Regime

In this chapter[1] we calculate the exact scattering matrix (without the Andreev approximation) for the NSN structure based on the BTK scattering theory described in Section 1.2.2 and use these expressions to get numerical results for current and both local and nonlocal shot noise using parameters based on LSCO. In Section 2.1, we describe the specifics of the application of BTK scattering theory to obtain the scattering amplitudes for the NSN geometry. (The expressions for the exact scattering amplitudes for the NSN junction are given in Appendix A). In this section we also give numerical results for some of the scattering coefficients. In Section 2.2, we utilize the expressions for the average current in the wire, and for the local shot noise from Sections 1.2.3.1 and 1.2.3.2 and present numerical results. In Section 2.3 we repeat this analysis for the nonlocal noise. Finally, in Section 2.4, we make some concluding remarks.

2.1 The Scattering System

In Figure 2.1 we sketch the geometry of the NSN junction discussed in this chapter. We will model the gap function for the system sketched in Figure 2.1 using a step function potential,

$$\Delta(\theta) = \begin{cases} \Delta(\theta) & 0 < z < h \\ 0 & x < 0 \;\; x > h \end{cases} \tag{2.1}$$

---

[1] The results presented here are based on the research article: C. Ostrove and L. E. Reichl, *Local and nonlocal shot noise in high-TC superconducting nanowires*, Physica B: Condensed Matter **561**, 79-89 (2019). L. E. Reichl suggested, supervised, performed many of the theoretical calculations for the project and shared in the writing for this paper. C. Ostrove performed most of the numerical calculations, generated most of the figures and shared in the writing.

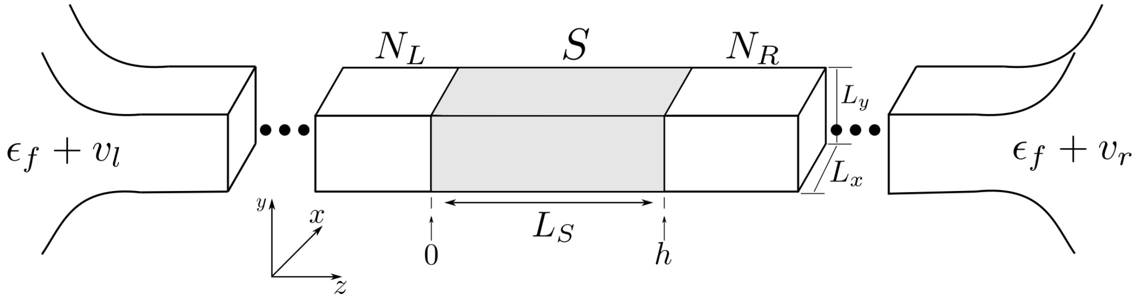

Figure 2.1: Sketch of the NSN geometry studied in this chapter. The normal leads are connected to thermal reservoirs with the same Fermi energy ϵ_f, but with potentially different applied biases, v_l and v_r. The central superconducting region has a length of L_S, the same Fermi energy as the normal metal leads and is assumed to be grounded with respect to the Fermi energy.

Note that in the equation for the gap above we have included an explicit spatial dependence. For the most common HTS materials, such as the cuprates, the order parameter is actually anisotropic, with the most common form for the anisotropy having what is known as d-wave pairing symmetry. The functional form of the d-wave order parameter is given by $\Delta(\theta) = \Delta_0 \cos(2\theta)$, where Δ_0 is the maximum value of the gap and θ is the direction of travel through the superconductor as measured with respect to the a-crystal axis (which we will fix to lie along the z axis). In this dissertation we will often refer to θ as the "orientation" of the order parameter and the angular dependence of the quantities which depend on Δ is implied.

Let us assume that both a particle and a hole are incident from the thermal reservoirs on the left and on the right. The solutions to the Bogoliubov-de Gennes equations in the left normal region, $\psi_L(z)$, the middle superconductor region, $\psi_S(z)$, and the right normal region, $\psi_R(z)$, are respectively

$$
\begin{aligned}
\psi_L(z) &= \frac{A_L^p}{\sqrt{q_p^L}}\begin{bmatrix}1\\0\end{bmatrix}\mathrm{e}^{iq_p^L z} + \frac{B_L^h}{\sqrt{q_h^L}}\begin{bmatrix}0\\1\end{bmatrix}\mathrm{e}^{-iq_h^L z}\\
&\qquad\qquad + \frac{C_L^p}{\sqrt{q_p^L}}\begin{bmatrix}1\\0\end{bmatrix}\mathrm{e}^{-iq_p^L z} + \frac{D_L^h}{\sqrt{q_h^L}}\begin{bmatrix}0\\1\end{bmatrix}\mathrm{e}^{+iq_h^L z},\\
\psi_S(z) &= \frac{A_S^p}{\sqrt{k_p}}\begin{bmatrix}u_o\\v_o\end{bmatrix}\mathrm{e}^{ik_p z} + \frac{B_S^h}{\sqrt{k_h}}\begin{bmatrix}v_o\\u_o\end{bmatrix}\mathrm{e}^{-ik_h z}\\
&\qquad\qquad + \frac{C_S^p}{\sqrt{k_p}}\begin{bmatrix}u_o\\v_o\end{bmatrix}\mathrm{e}^{-ik_p z} + \frac{D_S^h}{\sqrt{k_h}}\begin{bmatrix}v_o\\u_o\end{bmatrix}\mathrm{e}^{+ik_h z},\\
\psi_R(z) &= \frac{A_R^p}{\sqrt{q_p^R}}\begin{bmatrix}1\\0\end{bmatrix}\mathrm{e}^{iq_p^R z} + \frac{B_R^h}{\sqrt{q_h^R}}\begin{bmatrix}0\\1\end{bmatrix}\mathrm{e}^{-iq_h^R z}\\
&\qquad\qquad + \frac{C_R^p}{\sqrt{q_p^R}}\begin{bmatrix}1\\0\end{bmatrix}\mathrm{e}^{-iq_p^R z} + \frac{D_R^h}{\sqrt{q_h^R}}\begin{bmatrix}0\\1\end{bmatrix}\mathrm{e}^{+iq_h^R z},
\end{aligned}
\tag{2.2}
$$

where $q_\beta^\alpha = \sqrt{2m_\alpha^*\left(e \pm \epsilon_f^\alpha\right)}$ with $\alpha = L, R$ and $\beta = p, h$ and where we use the upper sign for particles and the lower sign for holes. Using Equation 2.2, we can determine the scattering amplitudes for electrons to transmit through, and be reflected from, the superconducting region. The boundary conditions for the wavefunctions in the high-transparency limit are continuity at $z = 0$ and $z = \mathrm{L}_s$, and continuity of the derivatives at those points. Thus

$$
\psi_L(0) = \psi_S(0), \quad {\psi'}_L(0) = {\psi'}_S(0), \quad \psi_S(L_S) = \psi_R(L_S), \quad {\psi'}_S(L_S) = {\psi'}_R(L_S) \tag{2.3}
$$

Using these equations, we can eliminate the coefficients $A_S^p,\ B_S^h,\ C_S^p,\ D_S^h$ and write $C_L^p,\ D_L^h,\ A_R^p,\ B_R^h$ as functions of $A_L^p,\ B_L^h,\ C_R^p,\ D_R^h$. This gives the matrix equation

$$
\begin{pmatrix} C_L^p \\ D_L^h \\ A_R^p \\ B_R^h \end{pmatrix} = \begin{pmatrix} r_{pp}^{LL} & r_{ph}^{LL} & t_{pp}^{LR} & t_{ph}^{LR} \\ r_{hp}^{LL} & r_{hh}^{LL} & t_{hp}^{LR} & t_{hh}^{LR} \\ t_{pp}^{RL} & t_{ph}^{RL} & r_{pp}^{RR} & r_{ph}^{RR} \\ t_{hp}^{RL} & t_{hh}^{RL} & r_{hp}^{RR} & r_{hh}^{RR} \end{pmatrix} \cdot \begin{pmatrix} A_L^p \\ B_L^h \\ C_R^p \\ D_R^h \end{pmatrix} \tag{2.4}
$$

Explicit expressions for these transmission and reflection amplitudes are given in Appendix A.

In Figure 2.2, we plot the magnitude of the transmission and reflection amplitudes for LSCO using parameters from Table 1.1, with a superconducting segment of lengths $L_S = 1.9\xi$, $L_S = 7.7\xi$ and $L_S = 77\xi$.

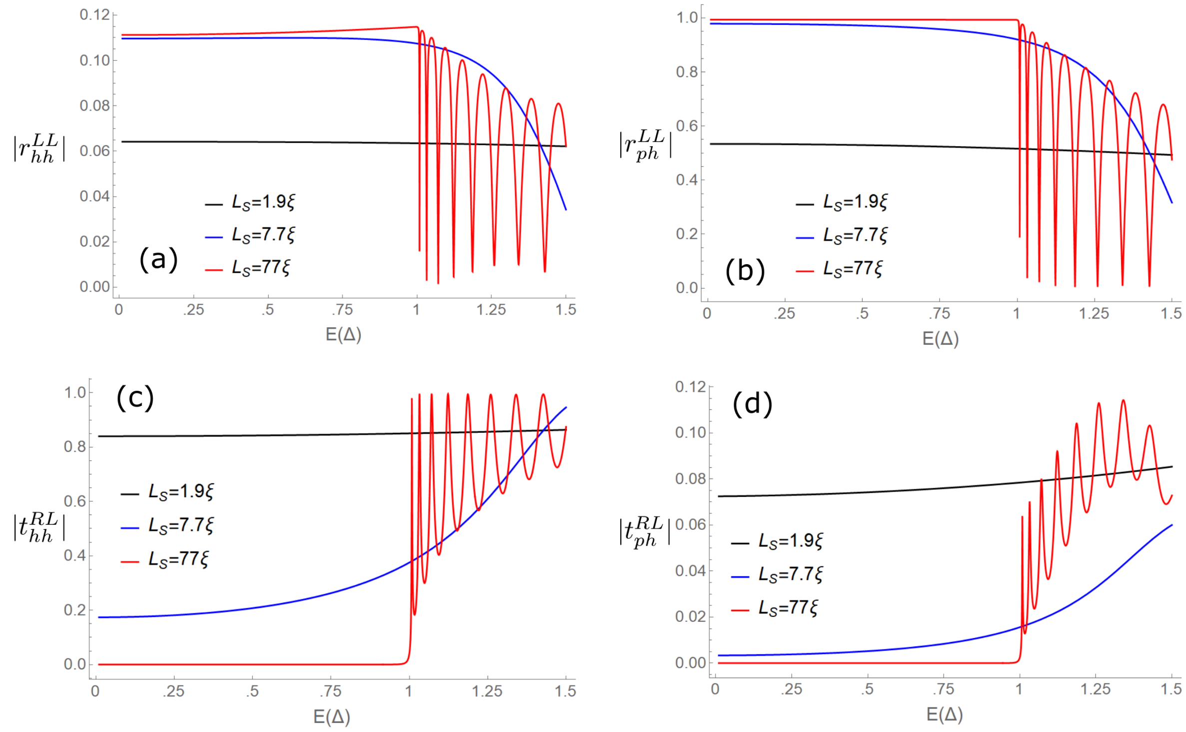

Figure 2.2: Scattering amplitudes (a) r_{hh}^{LL}, (b) r_{ph}^{LL}, (c) t_{hh}^{RL}, (d) t_{ph}^{RL}. Because we take the effective mass to be the same in all three parts of the wire, $|r_{pp}^{LL}| \approx |r_{hh}^{LL}|$, $|t_{pp}^{RL}| \approx |t_{hh}^{RL}|$, $|r_{hp}^{LL}| \approx |r_{ph}^{LL}|$, and $|t_{hp}^{RL}| \approx |t_{ph}^{RL}|$.

Figure 2.2(a) shows the amplitude for a particle (hole) to leave the left reservoir and reflect back into the left lead as a particle (hole). Figure 2.2(c) shows the amplitude for a particle (hole) to leave the left reservoir and reflect back into the left lead as a hole (particle). Figure 2.2(c) shows the amplitude for a particle (hole) to leave the right reservoir and transmit through the superconductor and enter the left lead as a particle (hole). Figure 2.2(d) shows the amplitude for a particle (hole) to leave the right reservoir and transmit into the left lead as a hole (particle). When the energy is less than the gap energy, the probability of Andreev reflection and of particle or hole transmission through the superconductor is nearly unity. For the largest system size we can see that at energies above the gap we have a large number of resonances appear in the scattering coefficients, which we will see signatures of in the energy distributions of the current and both local and nonlocal noise energy distributions in the next sections.

2.2 Current and Local Shot Noise in the Left Lead

We now consider the current and local shot noise for the case when the chemical potentials in the left and right reservoirs differ by $.1\Delta_0$. We consider three lengths of the superconducting segment, $L_S = 1.9\xi, 7.7\xi$ and 77ξ, and we assume that the temperature of the system is $T = 16.3\ K$. We start with the energy distributions for the thermally averaged current through the left lead in Figure 2.3. For all three system sizes we have a peak in the current through the left lead at zero energy with the magnitude falling off at higher energies, as one would expect due to the decrease in electron and hole populations at higher energy values. For $L_S = 77\xi$ we can see additional signatures in the current energy distribution at energies above the gap due to the over-the-gap transmission resonances we saw in Figure 2.2.

In Figure 2.4, we show contour plots of the energy distribution of the local shot noise in the left lead, which we will denote dS^{LL}, as a function of gap angle θ and energy. Figure 2.4(a) is for a superconducting segment of length $L_S = 1.9\xi$, Figure 2.4(b) for $L_S = 7.7\xi$ and Figure 2.4(c) for $L_S = 77\xi$. Figures 2.5(a)-(c)

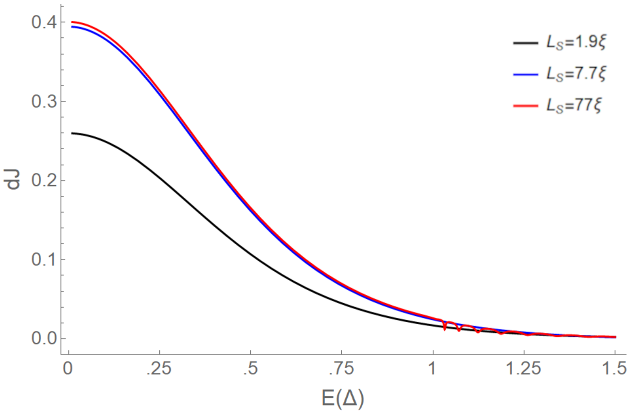

Figure 2.3: Plots of the energy distribution of the thermally averaged current in the left lead, dJ, for $\theta = 0$ and $v_l = .1\Delta_0$, $v_r = v_s = 0$.

show slices through the contour plots in Figure 2.4 at angles $\theta = 0$ and $\theta = \pi/5$ for each of the lengths. In all cases the local shot noise is positive, which is a signature of electron bunching due to their interaction with the superconducting region [50, 88].

For energies below the gap energy, the local shot noise is non-zero and decreases in magnitude with increasing energy. This contribution to the shot noise is due to particles and holes in the left lead that are involved with Andreev reflection from the superconductor. The decreasing magnitude of the noise is due to the decrease in the particle and hole Fermi distributions with increasing energy. With increasing energy, there are fewer particles and holes available to contribute to the shot noise. For energies above the gap for $L_S = 77\xi$, there are numerous peaks in the magnitude of the noise. These are due to scattering resonances inside the superconductor for energies above the gap, which allows selective transmission of particles and holes into and out of the superconductor.

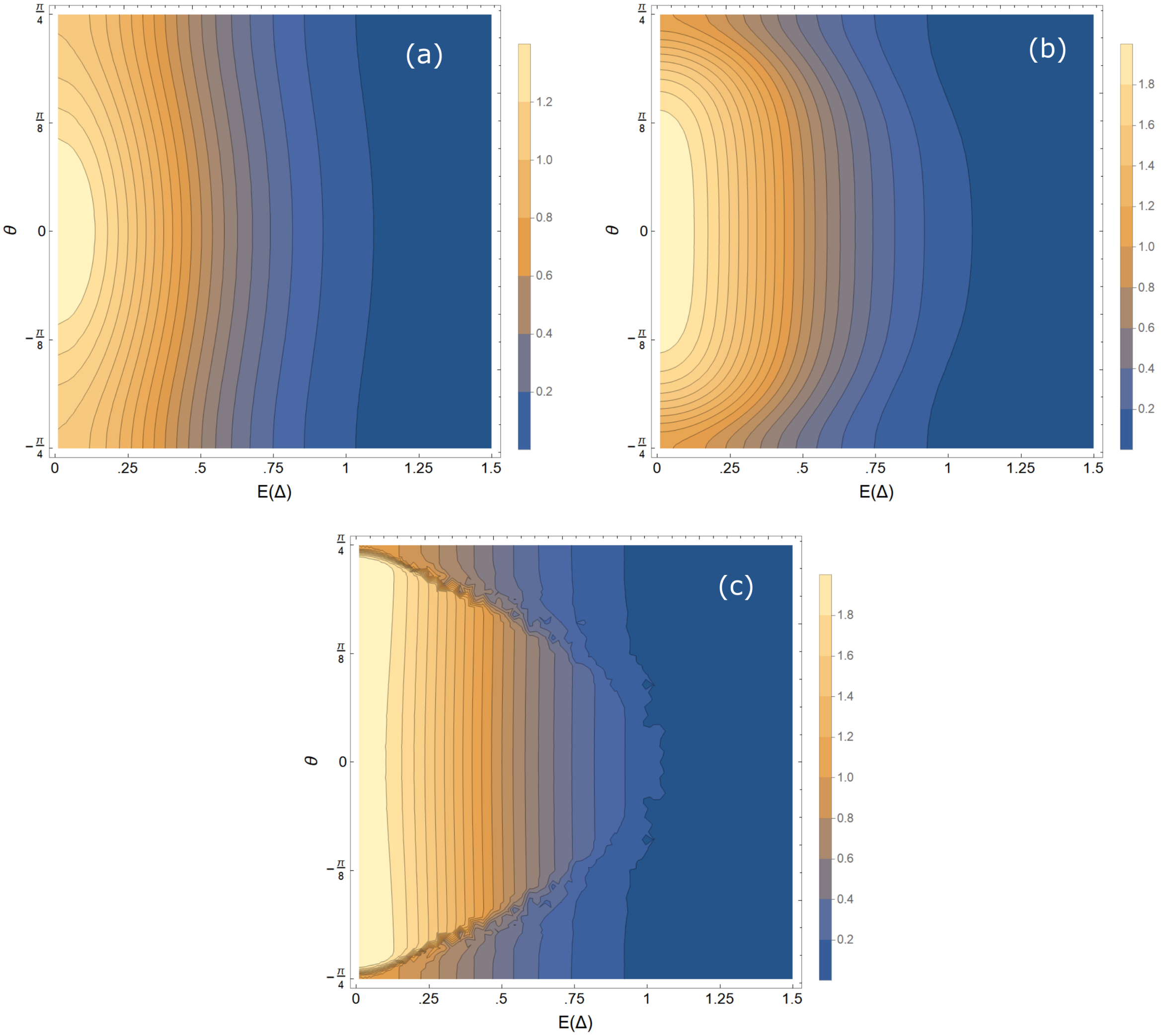

Figure 2.4: Contour plots of the total local differential shot noise dS^{LL} as a function of energy and the orientation of the order parameter, θ. (a) $L_S = 1.9\xi$, (b) $L_S = 7.7\xi$ and (c)$L_S = 77\xi$.

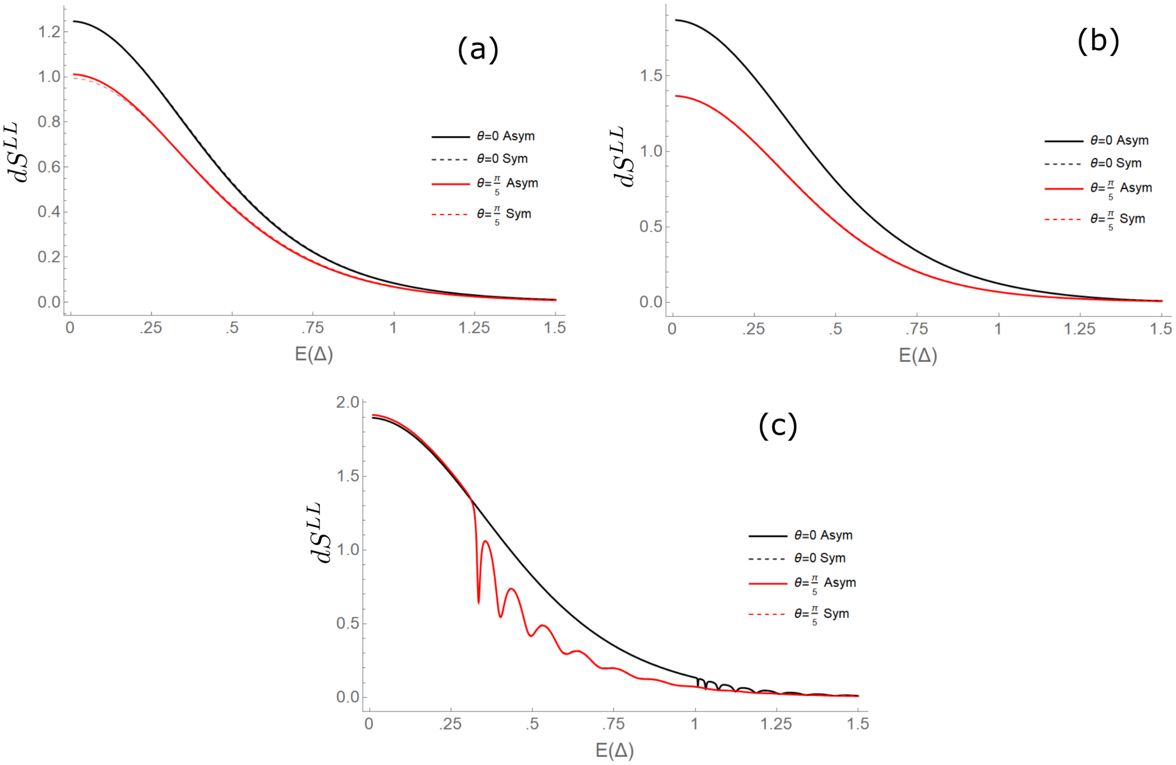

Figure 2.5: Plots of the total local differential shot noise dS^{LL} as a function of energy for $\theta = 0$ and $\theta = \frac{\pi}{5}$ with both asymmetric and symmetric biasing applied. (a) $L_S = 1.9\xi$, (b) $L_S = 7.7\xi$ and (c) $L_S = 77\xi$. (These slices are marked in Fig. 2.4).

2.3 Cross Correlated Shot Noise

We start our investigation of the behavior of the nonlocal shot noise energy distribution, denoted $dS^{LR} \equiv dS^{LR}/de$, by generating contour plots of dS^{LR} as a function of the orientation of the order parameter θ and the energy. In Figure 2.6 we show contour plots for dS^{LR} over the range of angles $\theta \in [-\pi/4, \pi/4]$ and for energies up to the edge of the first transverse mode. This is done for three different lengths for the superconducting region, L_S, with Figure 2.6(a) corresponding to $L_S = 1.9\xi$, Figure 2.6(b) to $L_S = 7.7\xi$ and Figure 2.6(c) to $L_S = 77\xi$. In addition, we evaluated two different schemes for biasing the junction: asymmetrically, by setting the potential in the left lead $v_l = .1\Delta_0$ and by grounding the superconductor and right lead ($v_s = v_r = 0$), and symmetrically by setting $v_l = v_r = .1\Delta_0$ and grounding the superconductor. In Figure 2.7 we give the plots of dS^{LR} corresponding to cross-sectional slices through the contour plots in Figure 2.6 for $\theta = 0$ and $\theta = \pi/5$. Figure 2.7(a) contains the $\theta = 0$ and $\theta = \pi/5$ slice for $L_S = 1.9\xi$, Figure 2.7(b) for $L_S = 7.7\xi$ and Figure 2.7(c) for $L_S = 77\xi$.

The nonlocal shot noise can be partitioned into the three components S_{pp}, S_{hh} and S_{ph}. In Figure 2.8 plots of dS^{LR}_{hh}, dS^{LR}_{pp} and dS^{LR}_{ph} are given for $\theta = 0$ and $\theta = \pi/5$ and with asymmetric biasing applied. (While the two different biasing schemes differ somewhat quantitatively, they share the same qualitative behavior). Superconducting region lengths of $L_S = 1.9\xi, 7.7\xi$ and 77ξ are plotted in Figures 2.8(a)-(c) respectively. One key feature we immediately notice is that while the S^{LR}_{hh} and S^{LR}_{pp} terms are always negative for all energies, the S^{LR}_{ph} term is strictly positive for the full energy range. Positive values of the nonlocal noise indicate electron bunching and are often associated with the generation of entanglement in CPS devices.

Also of interest is how the nonlocal noise changes as a function of the length of the superconducting region. In Figure 2.9 we plot the total nonlocal noise as well as the S^{LR}_{hh} and S^{LR}_{ph} contributions versus the length of the superconducting region with respect to a fixed value of $v_l = .1\Delta_0, v_r = v_s = 0$. What we find for the total nonlocal shot noise is that it monotonically increases, approaching zero from below as the

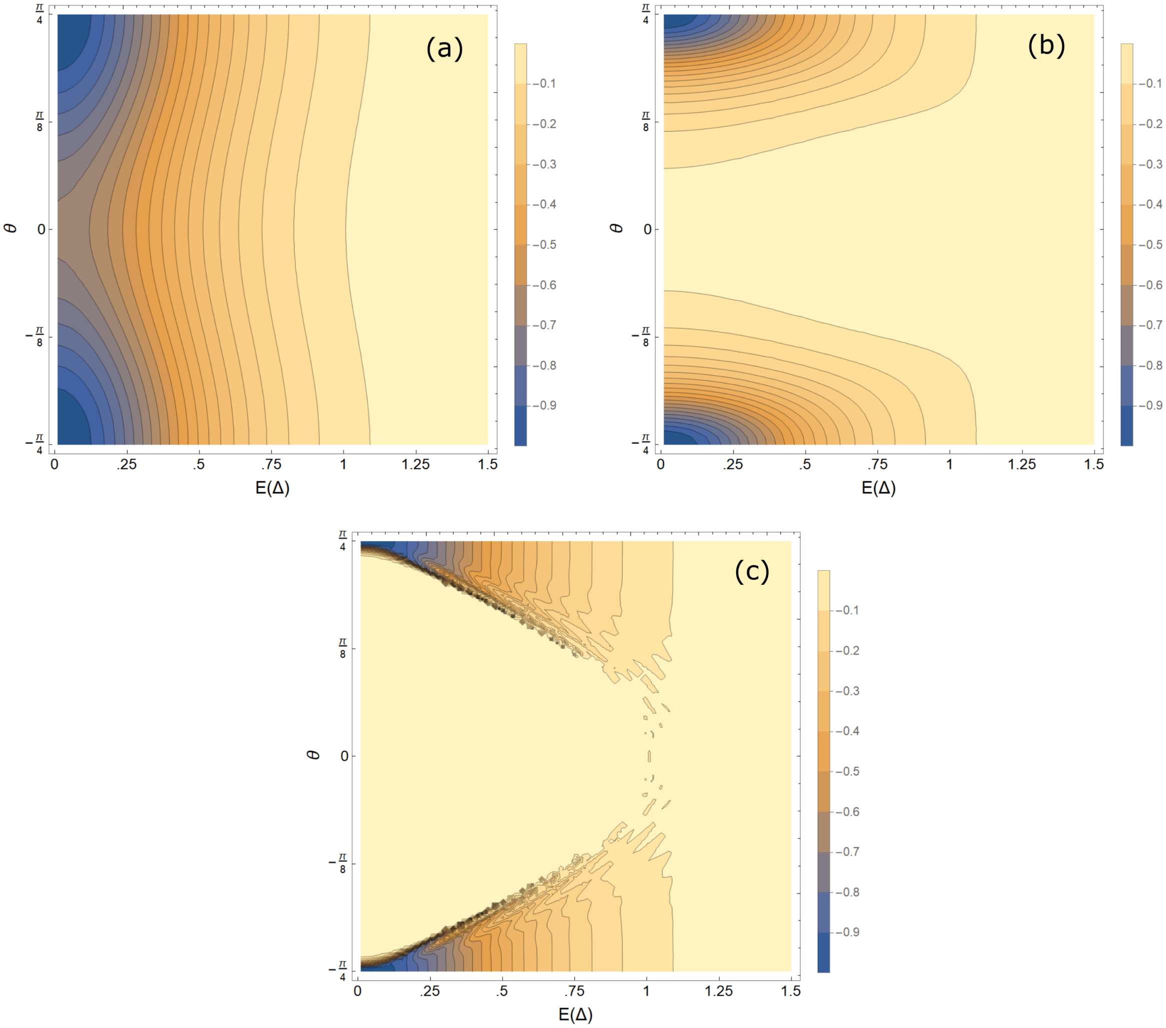

Figure 2.6: Contour plot of the total differential nonlocal shot noise dS^{LR} as a function of energy and the orientation of the order parameter, θ. (a) $L_S = 1.9\xi$, (b) $L_S = 7.7\xi$, (c) $L_S = 77\xi$.

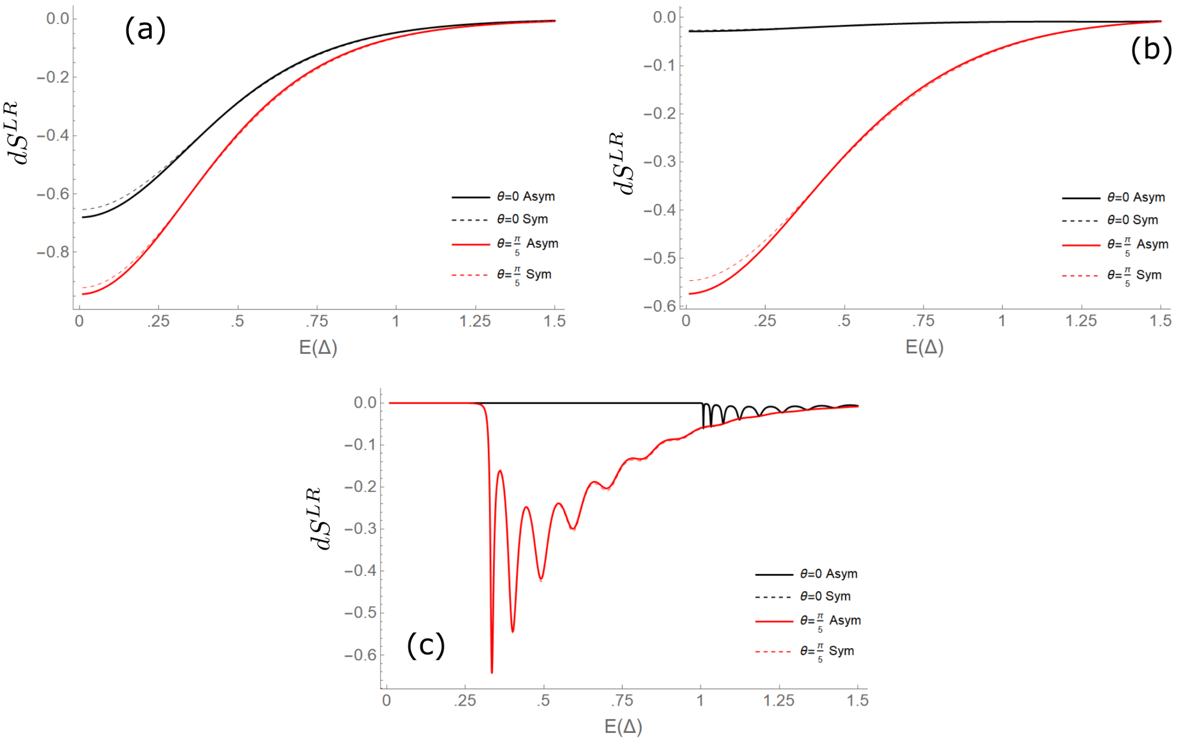

Figure 2.7: Plots of the total non-local differential shot noise dS^{LR} as a function of energy corresponding to the cross-sectional slices $\theta = 0$ and $\theta = \pi/5$ through the contour plots shown in Figure 2.6 with (a) $L_S = 1.9\xi$, (b) $L_S = 7.7\xi$ and (c) $L_S = 77\xi$. For each case we show the non-local shot noise for both symmetric and asymmetric biasing.

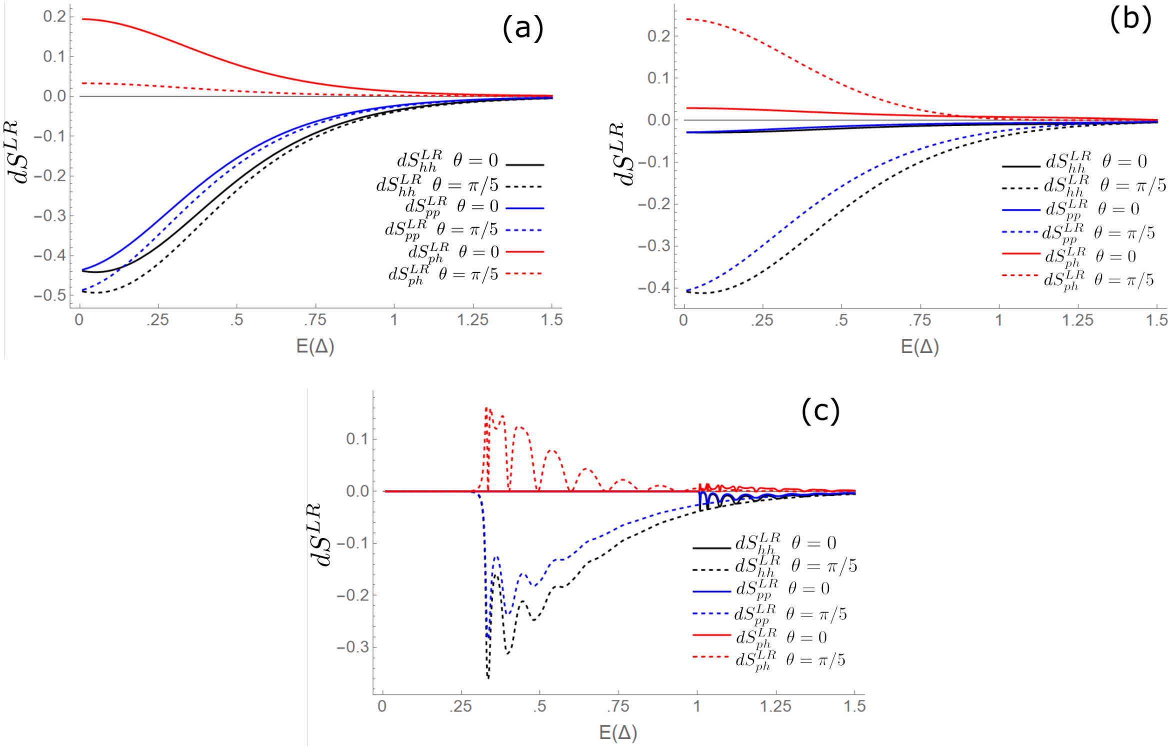

Figure 2.8: Plots of the nonlocal differential shot noise components dS_{hh}^{LR}, dS_{pp}^{LR} and dS_{ph}^{LR} as a function of energy for $\theta = 0$ and for $\theta = \pi/5$. (a) $L_S = 1.9\xi$. (b) $L_S = 7.7\xi$ and (c) $L_S = 77\xi$.

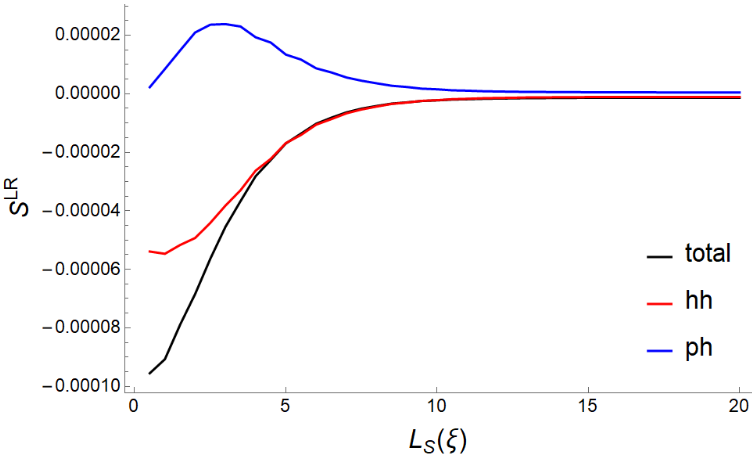

Figure 2.9: Plot of the total nonlocal shot noise S^{LR} as well as the components S^{LR}_{hh} and S^{LR}_{ph} as a function of the length of the superconducting region L_S measured in units of the superconducting coherence length ξ.

system size increases; likewise for the S^{LR}_{hh} and S^{LR}_{pp} contributions. The S^{LR}_{ph} contribution, however, displays a non-monotonic behavior, with a maximum at $L_S \approx 3\xi$ before again approaching zero.

Finally, we plot in Figures 2.10(a)-(c) the total cross-correlated shot noise as a function of the applied bias in the left lead for all three superconducting region lengths, $L_S = 1.9\xi, 7.7\xi$ and 77ξ.

For all three system sizes we see that the contribution due to S^{LR}_{hh} decreases with increased applied bias and the contribution from S^{LR}_{ph} increases with increased applied bias. When looking at the total cross-correlated shot noise S^{LR}, however, we see that there is a difference in behavior between the smallest system size, $L_S = 1.9\xi$ shown in Figure 2.10(a), and the larger system sizes in Figures 2.10(b) and (c). For $L_S = 1.9\xi$ the total nonlocal shot noise increases overall with increased applied bias, whereas for $L_S = 7.7\xi$ and 77ξ it decreases overall with increased applied bias.

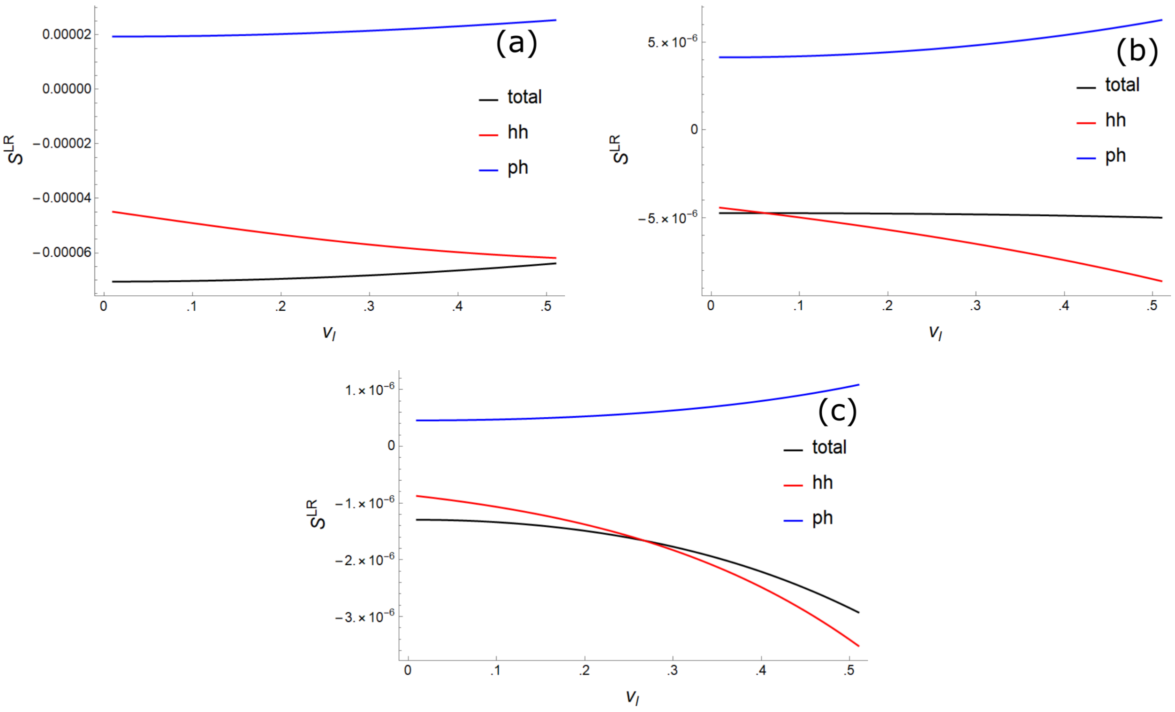

Figure 2.10: Plots of the total nonlocal differential shot noise S^{LR} and the components S^{LR}_{hh} and S^{LR}_{ph} as a function of energy for $\theta = 0$ and for $\theta = \pi/5$. (a) $L_S = 1.9\xi$. (b) $L_S = 7.7\xi$ and (c) $L_S = 77\xi$.

2.4 Conclusions

Exact expressions for the scattering matrix of a quasi-1D NSN junction have been found using scattering theory. These expressions correspond to the high transparency limit and are done without the Andreev approximation. Using realistic parameters for LSCO, we have investigated the local and nonlocal shot noise properties of the NSN structure. We have found that the local shot noise is always positive, as is expected because of bunching due to interactions between the electrons and the superconducting region. The total nonlocal shot noise is negative over the full energy range of the system; However, if we look at the various contributions separately we find the presence of scattering processes indicative of electron bunching (regions with positive shot noise contributions) due to the correlations between electrons and holes at opposite ends of the superconducting segment.

Acknowledgments

This work was supported by the Robert A. Welch Foundation (Grant No. F-1051).

Chapter 3

Cross-correlated Noise and Quasibound States in the NSNSN Geometry

This chapter[1] is organized as follows. In Section 1.2.2, we derive the scattering matrix for the NSNSN system. In Section 3.2 we list the properties of LSCO, the high-T_c superconductor that is used in our analysis. In Section 3.3 we present results for the cross-correlated shot noise energy distributions, and in Section 3.4 we describe the behavior of the scattering amplitudes. In Section 3.5 we focus on the resonances in the scattering coefficients and the connection between the quasibound states and the positive peaks in the cross-correlated shot noise energy distribution. In Section 3.6, we break down the dominant contributions to the positive cross-correlated shot noise at the resonances in our system. In Section 3.7, we compare the results for the NSNSN system to those of the NSN geometry and we also look at the system size dependence of the NSNSN geometry. In Section 3.8 we look at how the behavior of the cross-correlated shot noise changes as we decrease the system temperature. In Section 3.9, we compare the results of the full scattering theory used throughout this paper to those obtained using the Andreev approximation. Finally, in Section 3.10 we will summarize our results.

---

[1] The results presented here are based on a research article: C. Ostrove and L. E. Reichl, *Positive Cross-Correlated Shot Noise and Quasibound States in an NSNSN Geometry* [90]. L.E. Reichl suggested and advised the project, wrote an initial draft, and provided feedback and revisions on later versions of the paper. C. Ostrove performed the theoretical and numerical calculations for the project, generated the figures and contributed writing for additional sections and later revisions.

3.1 Scattering Theory

In Section 1.2.2 we introduced the general BTK approach to scattering theory in superconducting hetrostructures. In this section we provide a brief overview of the specific application to the NSNSN system as displayed in Figure 3.1.

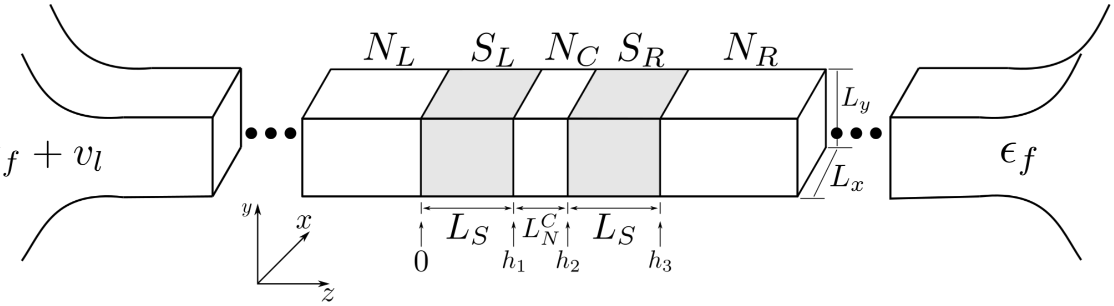

Figure 3.1: NSNSN geometry studied in this work. The left and right leads are much longer than the central SNS region and are connected to thermal reservoirs with Fermi energy ϵ_f with an additional bias of v_l applied to the left lead. More details on the system parameters used can be found in Section 1.3 and Table 3.1.

With reference to the points labeled in Figure 3.1, the gap function for this system (utilizing the standard step-function potential) is given by:

$$\Delta(\mathbf{r}) = \begin{cases} 0 & z < 0, \;\; h_1 < z < h_2, \;\; h_3 < z \\ \Delta_0 & 0 \le z \le h_1 \\ \Delta_0 e^{i\phi} & h_2 \le z \le h_3. \end{cases} \tag{3.1}$$

With this gap function, the wavefunctions in each of the 5 regions are given by:

$$\begin{aligned} \psi_{N_\alpha}(z) = {} & \frac{A^p_{N_\alpha}}{\sqrt{q^\alpha_p}} \begin{pmatrix} 1 \\ 0 \end{pmatrix} e^{iq^\alpha_p z} + \frac{B^h_{N_\alpha}}{\sqrt{q^\alpha_h}} \begin{pmatrix} 0 \\ 1 \end{pmatrix} e^{-iq^\alpha_h z} \\ & + \frac{C^p_{N_\alpha}}{\sqrt{q^\alpha_p}} \begin{pmatrix} 1 \\ 0 \end{pmatrix} e^{-iq^\alpha_p z} + \frac{D^h_{N_\alpha}}{\sqrt{q^\alpha_h}} \begin{pmatrix} 0 \\ 1 \end{pmatrix} e^{+iq^\alpha_h z}, \\ \psi_{S_\alpha}(z) = {} & \frac{A^p_{S_\alpha}}{\sqrt{k^\alpha_p}} \begin{pmatrix} u_o \\ v_o \end{pmatrix} e^{ik^\alpha_p z} + \frac{B^h_{S_\alpha}}{\sqrt{k^\alpha_h}} \begin{pmatrix} v_o \\ u_o \end{pmatrix} e^{-ik^\alpha_h z} \\ & + \frac{C^p_{S_\alpha}}{\sqrt{k^\alpha_p}} \begin{pmatrix} u_o \\ v_o \end{pmatrix} e^{-ik^\alpha_p z} + \frac{D^h_{S_\alpha}}{\sqrt{k^\alpha_h}} \begin{pmatrix} v_o \\ u_o \end{pmatrix} e^{+ik^\alpha_h z}, \end{aligned} \tag{3.2}$$

with $\alpha \in \{L, C, R\}$ for the normal regions and $\alpha \in \{L, R\}$ for the superconductors. The coherence factors u_0 and v_0, and the wavevectors k_p and k_h are given by

$$\begin{aligned} u_0 &= \sqrt{\frac{1}{2}\left(1 + \frac{\sqrt{e^2 - \Delta_0^2}}{e}\right)} & v_0 &= e^{i\varphi}\sqrt{\frac{1}{2}\left(1 - \frac{\sqrt{e^2 - \Delta_0^2}}{e}\right)} \\ k_p &= k_f\sqrt{1 + \sqrt{\frac{e^2 - \Delta_0^2}{\epsilon_f^2}}} & k_h &= k_f\sqrt{1 - \sqrt{\frac{e^2 - \Delta_0^2}{(\epsilon_f)^2}}}. \end{aligned} \tag{3.3}$$

In the normal regions where the gap function is zero the wavevectors q_p and q_h are now

$$q_p = k_F\sqrt{1 + \frac{e}{\epsilon_f}} \quad \text{and} \quad q_h = k_f\sqrt{1 - \frac{e}{\epsilon_f}}. \tag{3.4}$$

.

We are working in the high-transparency limit, so we require that the wavefunctions in Equation 3.2 and their derivatives are continuous at the interfaces between the normal regions and superconductors. The explicit boundary conditions are:

$$\begin{aligned} &\psi_{N_L}(0) = \psi_{S_L}(0), \quad \psi_{S_L}(h_1) = \psi_{N_C}(h_1), \quad \psi_{N_C}(h_2) = \psi_{S_R}(h_2), \quad \psi_{S_R}(h_3) = \psi_{N_R}(h_3), \\ &\dot{\psi}_{N_L}(0) = \dot{\psi}_{S_L}(0), \quad \dot{\psi}_{S_L}(h_1) = \dot{\psi}_{N_C}(h_1), \quad \dot{\psi}_{N_C}(h_2) = \dot{\psi}_{S_R}(h_2), \quad \dot{\psi}_{S_R}(h_3) = \dot{\psi}_{N_R}(h_3). \end{aligned} \tag{3.5}$$

These boundary conditions give us a system of 16 equations, which we can use to eliminate the coefficients for the S_L, N_C and S_R regions. Once we have eliminated the three central regions we can write the coefficients corresponding to outgoing particles and holes in terms of the coefficients of incoming particles and holes. Doing so we obtain the scattering matrix of the system,

$$\begin{pmatrix} C^p_{N_L} \\ D^h_{N_L} \\ A^p_{N_R} \\ B^h_{N_R} \end{pmatrix} = \begin{pmatrix} r^{LL}_{pp} & r^{LL}_{ph} & t^{LR}_{pp} & t^{LR}_{ph} \\ r^{LL}_{hp} & r^{LL}_{hh} & t^{LR}_{hp} & t^{LR}_{hh} \\ t^{RL}_{pp} & t^{RL}_{ph} & r^{RR}_{pp} & r^{RR}_{ph} \\ t^{RL}_{hp} & t^{RL}_{hh} & r^{RR}_{hp} & r^{RR}_{hh} \end{pmatrix} \begin{pmatrix} A^p_{N_L} \\ B^h_{N_L} \\ C^p_{N_R} \\ D^h_{N_R} \end{pmatrix}. \tag{3.6}$$

The scattering matrix elements are all functions of the energy of the particles and holes and the phase difference between the superconducting regions, ϕ. The subscripts on the scattering elements denote the outgoing and incoming excitation types, respectively, and the superscripts denote the outgoing and incoming leads, respectively.

3.2 System Parameters

For our model system we use parameters based on the high-T_c superconductor LSCO. The system parameters for LSCO are given in Table 1.1 and are reproduced in Table 3.1 for convenience. The temperature of the system, T_0, is $16.3K$ and the maximum energy $\epsilon_{\max}$ is $.000356E_H$. The Fermi distribution of the thermal reservoirs at this temperature is reproduced in Figure 3.2. The choice of temperature is such that one propagating mode exists in the device. We will generally bias the leftmost normal lead and we will be setting $v_l = .1\Delta_0$ for all of our numerical results. Unless explicitly stated otherwise, the numerical results will be for $L_S = 6\xi$ and $L_N^C = 2.75\xi$, where ξ is the superconducting coherence length. We also assume that a phase difference of ϕ can be induced between the superconducting segments, although this is not essential for our main results.

T_c (K)	38
ξ (a_B)	65
Δ (E_H)	0.000212
ϵ_f (E_H)	0.000935
$\epsilon_{\max}$ (E_H)	0.000356
T_0 (K)	16.3
L_y	1.85ξ
L_x	$1.2L_y$

Table 3.1: System parameters for LSCO, taken from [34], Table 7.4

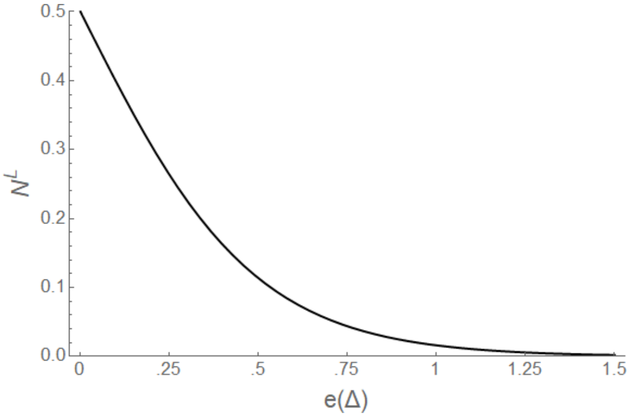

Figure 3.2: Plot of the Fermi distribution, N^L, with zero bias and $T_0 = 16.3K$.

3.3 Cross-Correlated Shot Noise for NSNSN

Figure 3.3 shows plots of the shot noise distribution $dS^{LR}(e)$ and average current $dJ(e)$ as a function of energy for $L_S = 6\xi$ and $L_N^C = 2.75\xi$. We can see that there is a subgap energy interval where the cross-correlated shot noise is positive. In Figure 3.3(b) we plot the energy distribution of the current. Vertical lines have been drawn in to highlight the overlap between these distributions in the region of positive cross-correlated shot noise. We can see that a nontrivial fraction of the current is indeed carried by electrons in this energy interval.

The size of the superconducting regions affects the behavior of the cross-correlated shot noise. In Figures 3.4(a) and 3.4(b) we plot the cross-correlated noise energy distributions for superconducting regions ranging in length from $L_S = 1\xi$ to $L_S = 9\xi$ with L_N^C fixed at 2.75ξ. For small values of L_S ($1\xi{\le}L_S{\le}4\xi$) shown in Figure 3.4(a)) we see no energy intervals of positive cross-correlated shot noise. For larger values of L_S, ($4\xi{\le}L_S{\le}9\xi$) shown in Figure 3.4(b), we do see energy intervals with positive cross-correlated shot noise. The maximum values of the positive peak decreases as we increase L_S beyond $L_S = 6\xi$. At intermediate values of L_S ($4\xi{\le}L_S{\le}6\xi$), we find large positive peaks in the positive cross-correlated shot noise with finite

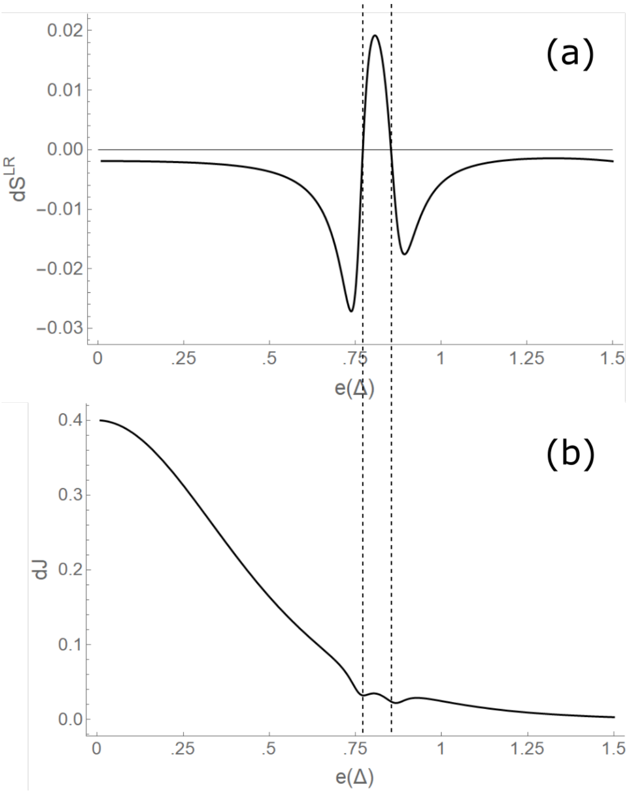

Figure 3.3: Energy distribution for the (a) cross correlated shot noise and (b) current with $L_S = 6\xi$, $L_N^C = 2.75\xi$ and $\phi = 0$. Lines have been drawn on the current plot to highlight the overlap between the current distribution and the positive region of the cross correlated shot noise.

energy width. In Section 3.7 we will evaluate the relationship between the positive cross-correlated noise and the size of L_S and L_N^C in more detail.

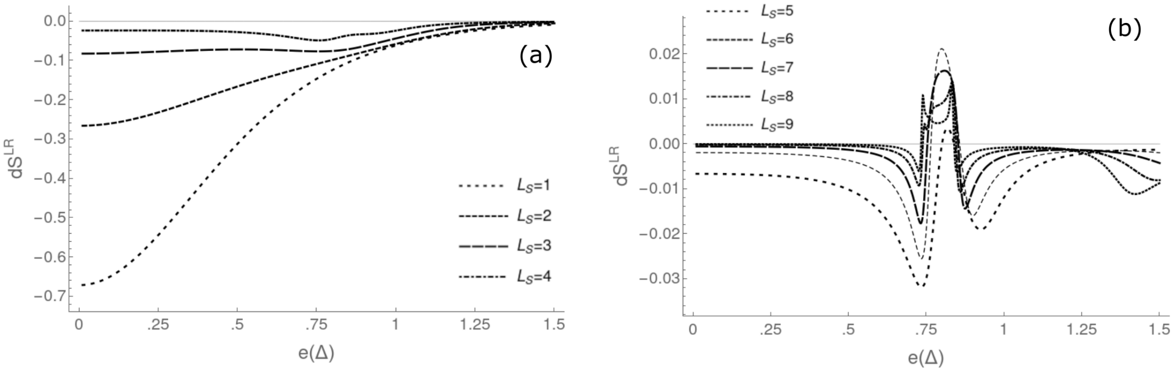

Figure 3.4: Differential cross-correlated shot noise for a number of different superconducting region sizes. In (a) we plot $L_S = 1 - 4\xi$ and in (b) we plot $L_S = 5 - 9\xi$. For both (a) and (b) the size of the central normal region is 2.75ξ.

3.4 Scattering Amplitudes for NSNSN

In Figure 3.5 we give plots of $|t^{LR}_{pp}|$, $|t^{LR}_{hh}|$ and $|t^{LR}_{ph}|$ for a few different values of L_S and ϕ. For Figures 3.5(a)-(c) $L_S = 6\xi$ and $L_N^C = 2.75\xi$. The phase differences between the two superconducting regions in Figures 3.5(a)-3.5(c) are 0, $\frac{\pi}{6}$ and $-\frac{\pi}{6}$ respectively. In Figure 3.5(d), $L_S = 8\xi$, $L_N^C = 2.75\xi$ and $\phi = \frac{\pi}{6}$.

In Figure 3.5(a), there is a pair of resonances in the transmission amplitudes with peaks in t^{RL}_{pp}, t^{RL}_{hh} and t^{RL}_{hp} below the gap energy. There is a small shift in the peaks of the particle-particle and hole-hole resonances due to the small momentum difference between particles and holes with the same energy. There is also a resonance in t^{RL}_{hp}. As we change the phase difference ϕ, the offset in the positions of the t^{RL}_{pp} and t^{RL}_{hh} resonances increases, with the positions of the peaks for t^{RL}_{pp} and t^{RL}_{hh} dependent on the sign of the phase difference. At the same time, as we increase ϕ the magnitude of the second resonance in t^{RL}_{pp} and t^{RL}_{hh} markedly decreases.

In Figure 3.5(d) we see that increasing the size of the superconducting regions results in sharper

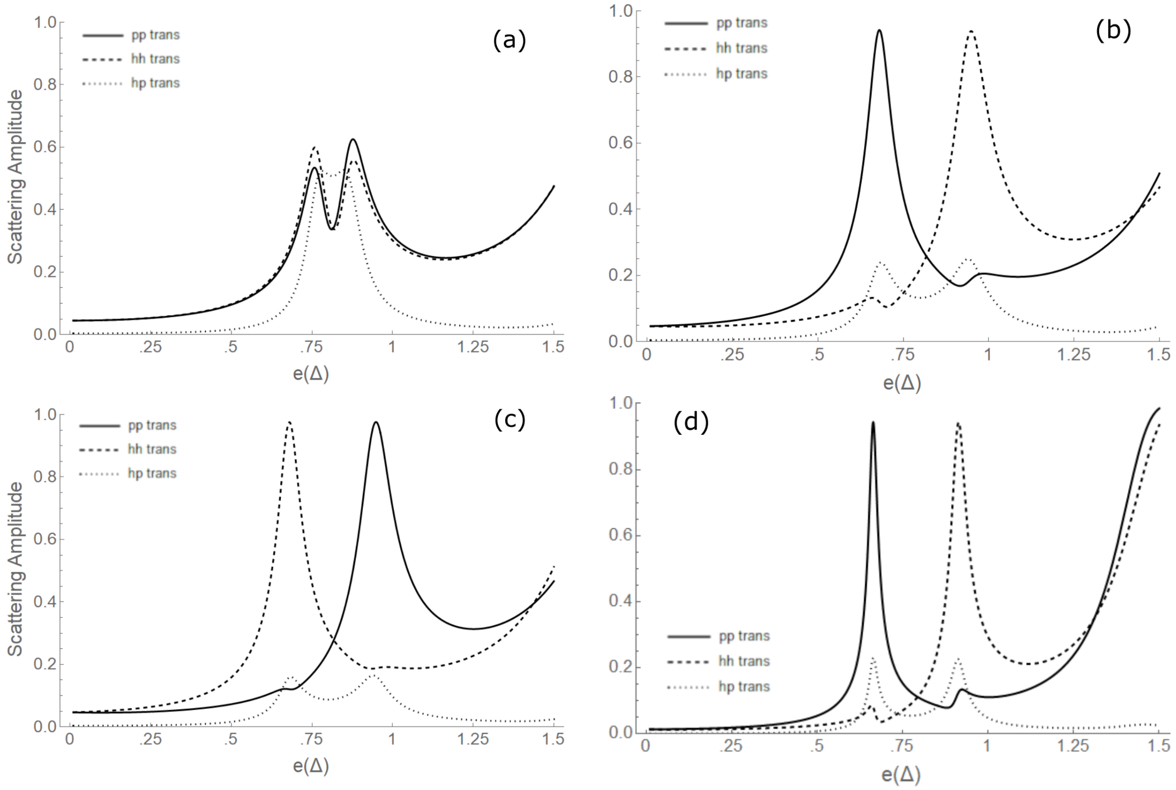

Figure 3.5: Plots of the magnitudes of the particle-particle, hole-hole and particle-hole transmission coefficients for a variety of system parameters. (a) $L_S = 6\xi$ and $\phi = 0$, (b) $L_S = 6\xi$ and $\phi = \frac{\pi}{6}$, (c)$L_S = 6\xi$ and $\phi = -\frac{\pi}{6}$, (d) $L_S = 8\xi$ and $\phi = \frac{\pi}{6}$.

resonances. Whereas it appears in Figures 3.5(a)-(c) that t_{ph}^{RL} has a centrally located resonance in-between the t_{pp}^{RL} and t_{hh}^{RL} resonances, t_{ph}^{RL} actually has a pair of resonances at the same energies as the t_{pp}^{RL} and t_{hh}^{RL} resonances. A key feature we see in the scattering plots is that for $L_S = 6\xi$ at small values of ϕ there is a small energy interval in-between the resonances in t_{pp}^{RL} and t_{hh}^{RL} where t_{ph}^{RL} becomes the dominant transmission term. This energy interval corresponds nearly exactly to the energy interval in which we observed a positive peak for $dS^{LR}(e)$ in Figure 3.3(a).

3.5 Quasibound States and Pole Structure

We saw in Figure 3.5 clear evidence for the existence of resonances in the plots of t_{pp}^{RL}, t_{hh}^{RL} and t_{hp}^{RL}. Below the gap, excitations in the central normal region are confined by repeated Andreev reflections at each of the interfaces. In the NSNSN geometry, this produces quasibound states, as the finite size of the superconducting regions allow particles and holes to tunnel out at a nonzero rate.

In Figure 3.6(a) we plot $|t_{pp}^{RL}|$ for complex energy values and for the same parameters used in Figure 3.5(a). The contour plot in Figure 3.6 shows that the resonances in t_{pp}^{RL} in Figure 3.5(a) are due to a pair of closely spaced poles in the complex energy plane.

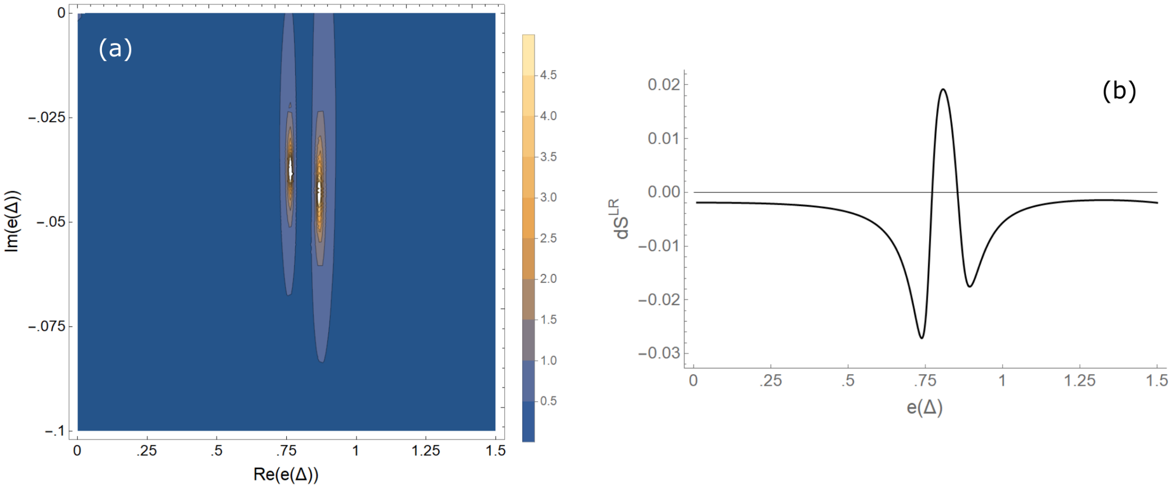

Figure 3.6: (a) Plot of $|t_{pp}^{LR}|$ in the complex energy plane for $L_S = 6\xi$ and $L_C^N = 2.75\xi$. The poles correspond to the quasibound state resonances in Figure 3.5(a). (b) Corresponding plot of $dS^{LR}(e)$.

In Figure 3.6(b) we have the corresponding plot of $dS^{LR}(e)$. Away from the quasibound states $dS^{LR}(e)$ is entirely negative. At the quasibound state energy, however, there is a large positive peak in the value of $dS^{LR}(e)$. This connection between the positivity of $dS^{LR}(e)$ and the positions of the quasibound states is fairly general as well. In Figure 3.7 we plot the complex poles and the cross-correlated noise for a longer central normal region, $L_S = 6\xi$ and $L_N^C = 5\xi$. Increasing L_N^C has the effect of decreasing the real and imaginary parts of the quasibound state energies. In Figure 3.7(b) the energy interval with positive cross-correlated shot noise has shifted to the left in accordance with the movement of the quasibound states.

For sufficiently large values of L_N^C we can start to have additional quasibound states emerge which results in additional scattering resonances and additional positive peaks in the plots of $dS^{LR}(e)$. This can be seen in Figure 3.8, where we plot $dS^{LR}(e)$ and the transmission coefficients for $L_S = 6\xi$ and $L_N^C = 13\xi$.

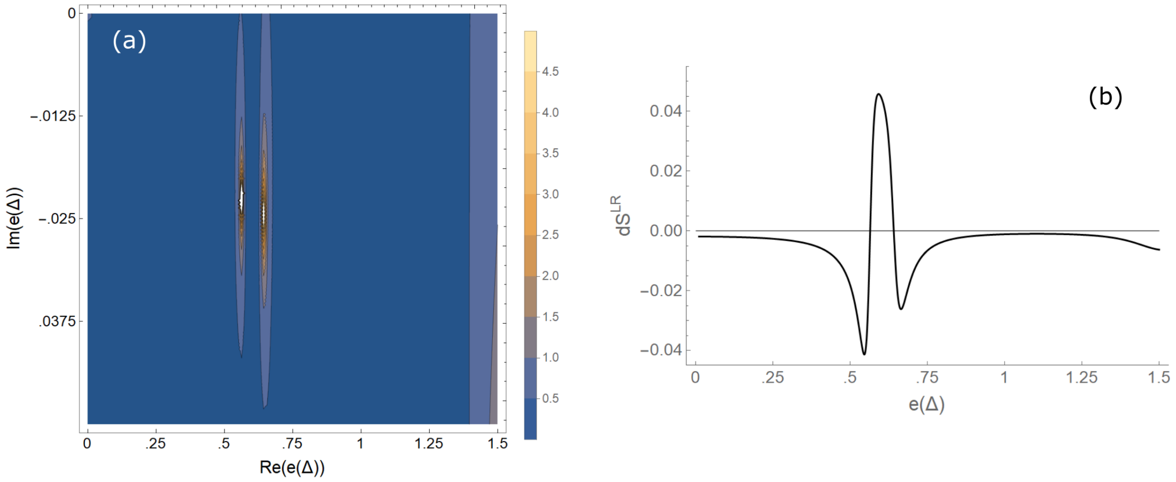

Figure 3.7: (a) Magnitude of $|t_{pp}^{LR}|$ in the complex energy plane for $L_S = 6\xi$ and $L_C^N = 5\xi$. (b) Corresponding plot of $dS^{LR}(e)$.

In addition to modifying the quasibound state energies by changing L_N^C, we can also change ϕ. In Figure 3.9 we plot the poles of t_{pp}^{LR} with (a) $\phi = \frac{\pi}{12}$ and (b) $\phi = -\frac{\pi}{12}$. Increasing the phase difference in the positive direction shifts the real energy of the pole on the left and shrinks the size of the pole on the right. With a negative phase difference it is now the pole on the left that shifts its real energy and shrinks. However, while it is possible to shift the positions of the quasibound states by adjusting the value of ϕ, this can have the effect of reducing the positivity of the noise correlations. This is seen in Fig 3.10, where $dS^{LR}(e)$ is plotted as a function of both the energy, e, and the phase difference ϕ. Positive values of $dS^{LR}(e)$ are localized about a small range of ϕ values near zero. This suggests that for the goal of maximizing the

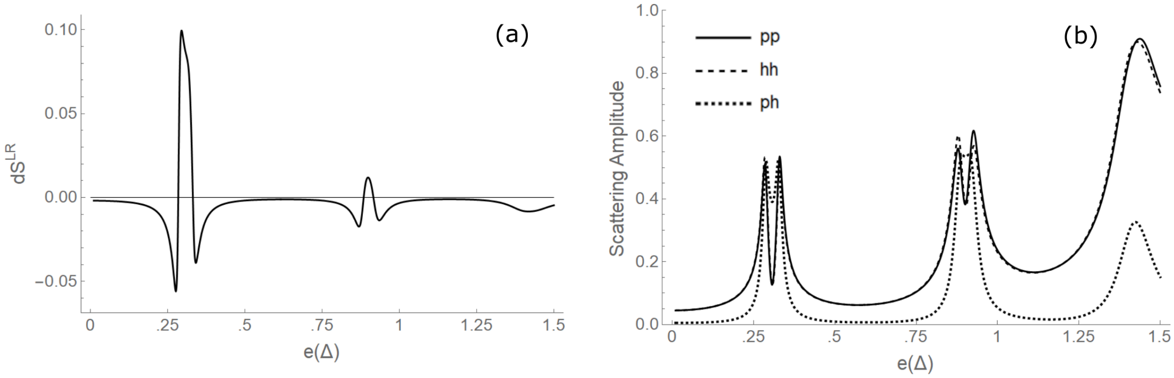

Figure 3.8: (a) Plot of $dS^{LR}(e)$ for $L_S = 6\xi$ and $L_C^N = 13\xi$. Note the existence of multiple positive peaks in the energy distribution. (b) Corresponding plots of $|t_{pp}^{LR}|$, $|t_{hh}^{RL}|$ and $|t_{hp}^{RL}|$. There is a one-to-one correspondence between the resonances and the positive noise correlations.

positivity of $dS^{LR}(e)$ it is best to set $\phi = 0$.

3.6 Origin of Positive Noise Cross-Correlation

In the previous section, we observed a connection between the location of the quasibound state poles and the energy intervals of positive cross-correlated shot noise. In this section, we show the origin of the positive contributions to the cross-correlated shot noise at the resonance energies.

In Fig. 3.11, we plot the three terms, dS_{pp}^{LR}, dS_{hh}^{LR} and dS_{ph}^{LR} separately. Away from the resonances the only term which goes positive is dS_{ph}^{LR}. However, at the resonance we see that dS_{pp}^{LR}, dS_{hh}^{LR} and dS_{ph}^{LR} switch behaviors and now there is an overall negative contribution due to dS_{ph}^{LR} and an overall positive contribution due to dS_{pp}^{LR} and dS_{hh}^{LR}. Since dS_{pp}^{LR} and dS_{hh}^{LR} have similar qualitative behavior we will focus on just the positive contributions arising from dS_{pp}^{LR}.

The contribution to the shot noise from dS_{pp}^{LR} is given in Eq. 1.40. It can be split into three terms, each with a different dependence on the thermal reservoirs. They are as follows:

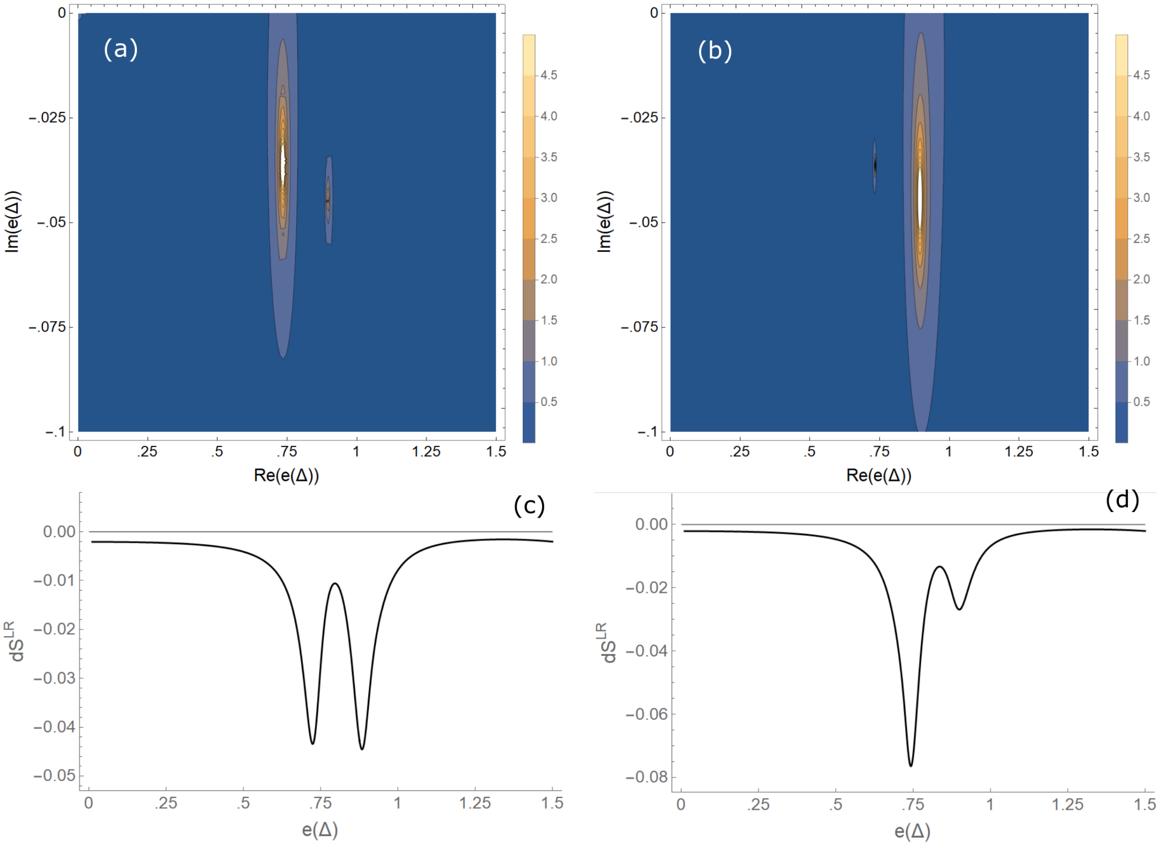

Figure 3.9: Poles of $|t_{pp}^{LR}|$ for (a) $\phi = \frac{\pi}{12}$ and (b) $\phi = -\frac{\pi}{12}$, with the corresponding plots of $dS^{LR}(e)$ given in (c) and (d) respectively. As we change the phase difference the second resonance we saw in Figure 3.6 becomes smaller and eventually disappears entirely.

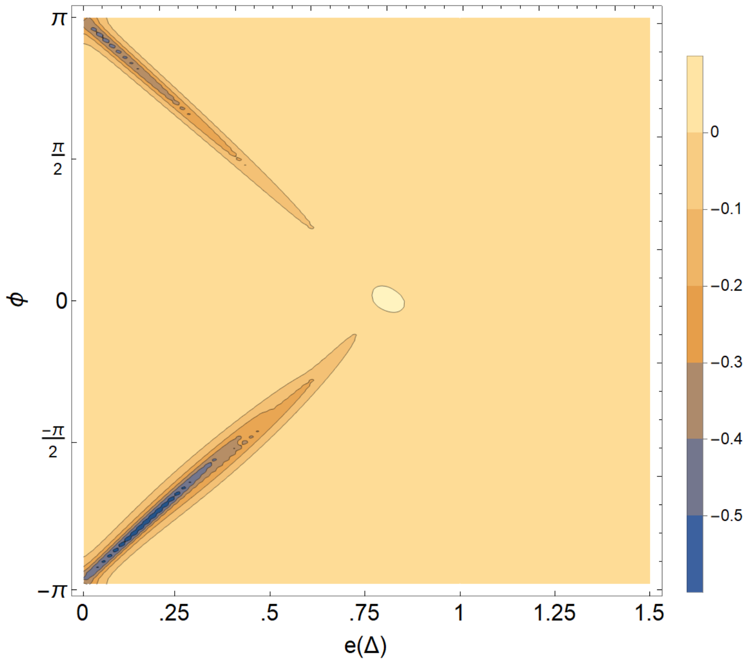

Figure 3.10: Phase dependence of the cross-correlated shot noise. We can see that the region of positive shot noise is localized around the value $\phi = 0$, and is maximized at that point in general.

$$dS_{pp}^{LR}(1) = \frac{m_L m_R}{\pi^2 \hbar^4} F_p^L N_p^L \big((-|r_{hp}^{LL}|^2 + |r_{pp}^{LL}|^2 - 1)\ (-|t_{hp}^{RL}|^2 + |t_{pp}^{RL}|^2) \big) \tag{3.7}$$

$$dS_{pp}^{LR}(2) = \frac{m_L m_R}{\pi^2 \hbar^4} F_p^R N_p^R \big((-|r_{hp}^{RR}|^2 + |r_{pp}^{RR}|^2 - 1)(-|t_{hp}^{LR}|^2 + |t_{pp}^{LR}|^2) \big) \tag{3.8}$$

$$\begin{aligned} dS_{pp}^{LR}(3) =& \frac{m_L m_R}{\pi^2 \hbar^4} (F_p^L N_p^R + F_p^R N_p^L) \big(\mathrm{Re}\left[r_{hp}^{LL} r_{hp}^{RR} t_{hp}^{LR*} t_{hp}^{RL*} \right] - \mathrm{Re}\left[r_{hp}^{LL*} r_{pp}^{RR*} t_{pp}^{RL} t_{hp}^{LR} \right] \\ &+ \mathrm{Re}\left[r_{pp}^{LL} r_{pp}^{RR} t_{pp}^{LR*} t_{pp}^{RL*} \right] - \mathrm{Re}\left[r_{pp}^{LL*} r_{hp}^{RR*} t_{hp}^{RL} t_{pp}^{LR} \right] \big) \end{aligned} \tag{3.9}$$

In Figures 3.12(a)-(c) we plot each of these 3 terms separately.

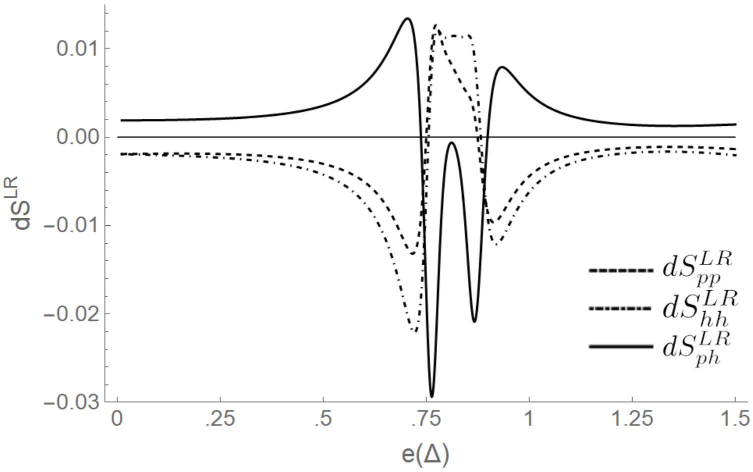

Figure 3.11: Contributions to the differential cross-correlated shot noise dS_{pp}^{LR}, dS_{hh}^{LR} and dS_{ph}^{LR} (plotted separately), for $L_S = 6\xi$ and $L_N^C = 2.75\xi$. Away from the resonance dS_{pp}^{LR} and dS_{hh}^{LR} are negative and dS_{ph}^{LR} is positive. At the resonance dS_{pp}^{LR} and dS_{hh}^{LR} are positive and dS_{ph}^{LR} is negative.

We now focus on $dS_{pp}^{LR}(1)$. Expanded out fully, $dS_{pp}^{LR}(1)$ has six separate components, three of which give rise to positive correlations at the resonance. These three terms are (neglecting the Fermi distribution prefactors) $\Sigma_1 = |t_{pp}^{RL}|^2 |r_{pp}^{LL}|^2$, $\Sigma_2 = |t_{hp}^{RL}|^2$ and $\Sigma_3 = |t_{hp}^{RL}|^2 |r_{hp}^{LL}|^2$. In Figure 3.12(d)-(f) we give their respective plots. The largest of the three contributions is due to the Σ_1 term, which corresponds to the CAR

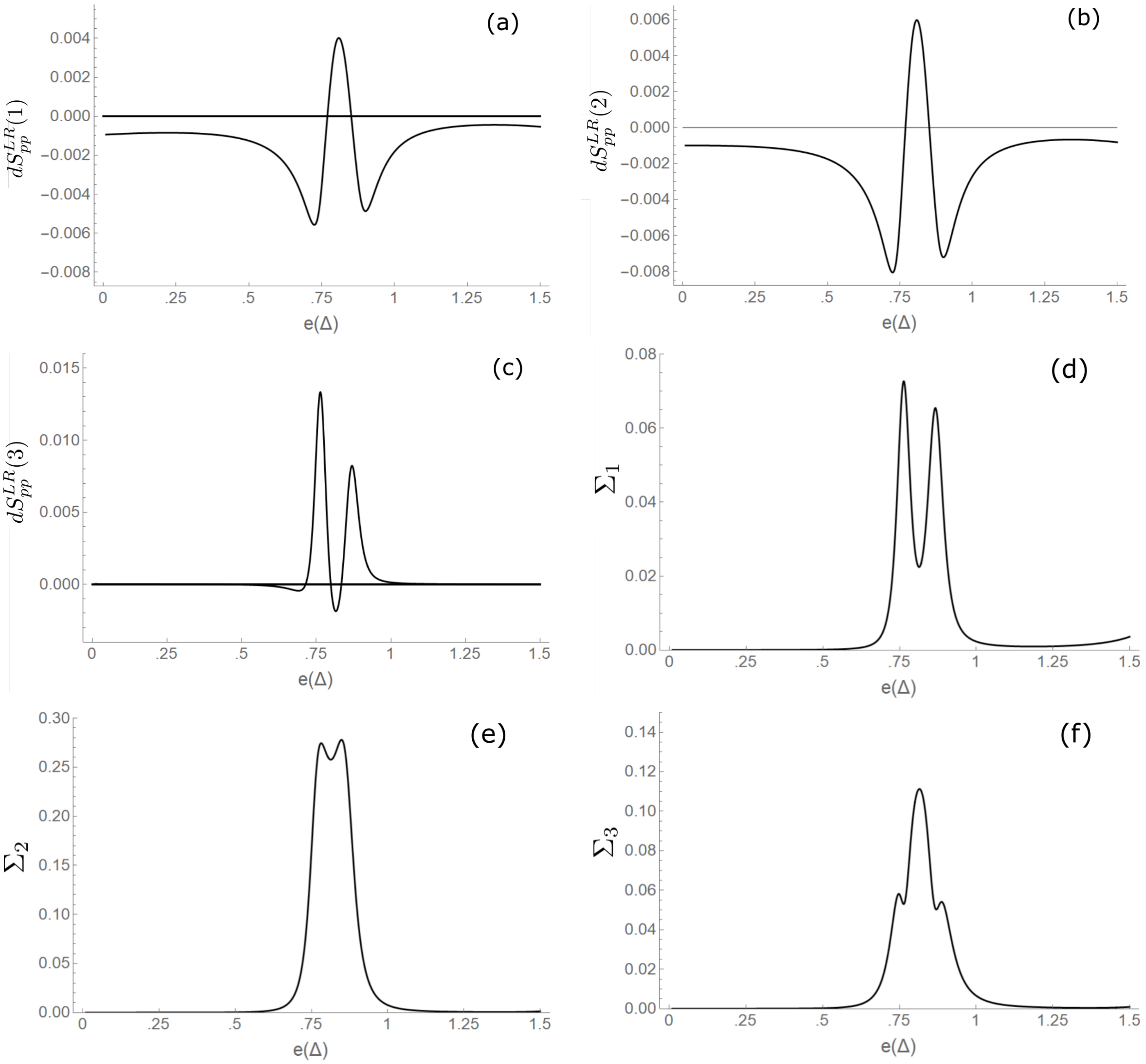

Figure 3.12: Plots of components of dS_{pp}^{LR} for $L_S = 6\xi$ and $L_N^C = 2.75\xi$. (a) $dS_{pp}^{LR}(1)$. (b) $dS_{pp}^{LR}(2)$. (c) $dS_{pp}^{LR}(3)$. All three components are negative away from the resonance but contribute positively at the resonance energies. Additionally, plots of the 3 components of $dS_{pp}^{LR}(1)$ which give rise to positive correlations, (d) $\Sigma_1 = |t_{pp}^{RL}|^2|r_{pp}^{LL}|^2$, (e) $\Sigma_2 = |t_{hp}^{RL}|^2$, (f) $\Sigma_3 = |t_{hp}^{RL}|^2|r_{hp}^{LL}|^2$.

process [28]. The remaining two terms are characterized using a scheme based on [43] and [42]. Each of the higher-order products of scattering coefficients consists of two reflection coefficients, either normal reflection (NR) (r_{pp} or r_{hh}) or Andreev reflection (AR) (r_{ph} and r_{hp}), and two transmission coefficients, either elastic cotunneling (EC) (t_{pp} or t_{hh}) or crossed Andreev reflection (CAR) (t_{ph} or t_{hp}). Using this scheme, Σ_1 is called an EC-NR term, as it consists of two normal transmission and two normal reflection coefficients, and Σ_3 is called a CAR-AR term, as it consists of two Andreev reflection and two crossed Andreev reflection coefficents.

In contrast to [43] and [42], which found that at $T = 0$ EC-NR and CAR-AR terms always result in negative correlations, at finite temperatures in the NSNSN system these terms can indeed give positive contributions, as seen in Figures 3.12(d) and (f). The EC-NR term arises microscopically due to correlations induced by the elastic cotunneling scattering processes [43]. The CAR-AR term arises microscopically from a process referred to as synchronized Andreev reflection (AR-AR), a higher-order process in which a pair of Andreev reflections (from particle to hole or vice versa) at the leftmost and rightmost interfaces occur in a coherent fashion [106].

3.7 System Size Dependence and Comparison to NSN Geometry

It is important to compare results for the NSNSN system with those of the simpler NSN geometry. In particular, we are interested in comparing results in the case where the size of the central superconducting region S in the NSN geometry is the same size as the central SNS structure in the NSNSN geometry. In Figure 3.13(a) we plot the cross-correlated noise distributions for an NSNSN system with $L_S = 6\xi$ and $L_N^C = 2.75\xi$ and an NSN system with $L_S = 14.75\xi$. Unlike the NSNSN system, for the NSN system we no longer see any energy intervals in which dS^{LR} goes positive. This is not just the case for this choice of system size either. In Figure 3.13(b) we plot dS^{LR} for a range of superconducting region sizes for the NSN

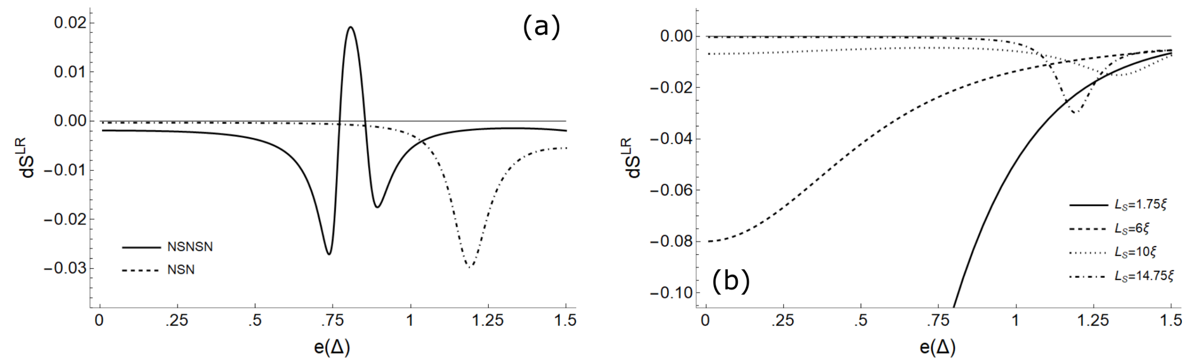

Figure 3.13: (a) Comparison $dS^{LR}(e)$ for the NSNSN and NSN geometries. For the NSNSN system $L_S = 6\xi$ and $L_N^C = 2.75\xi$ and for the NSN system $L_S^{NSN} = 14.75\xi$. (b) Plot of dS^{LR} for the NSN system with $L_S^{NSN} = 1.75\xi$, 6ξ, 10ξ and 14.75ξ. The total cross-correlated noise energy distribution remains negative over the entire energy interval.

system ranging from $L_S^{NSN} = 1.75\xi$ to Ł$_S^{NSN} = 14.75\xi$, and for all of these system sizes we see that the total cross-correlated noise distribution remains negative over the full energy range of the system.

We will now readdress the relationship between the system size and the positivity of dS^{LR} discussed in Section 3.3 (specifically in Figure 3.4). To do so we will define the quantity

$$S_+^{LR} = \int de\ \mathrm{clip}_+(dS^{LR}(e)), \tag{3.10}$$

where

$$\mathrm{clip}_+(x) = \begin{cases} 0 & x < 0 \\ x & x \geq 0. \end{cases} \tag{3.11}$$

This expression corresponds to the total area of the positive regions of dS^{LR} and gives us a simple measure with which to compare the positivity of the cross-correlated noise for different values of L_S and L_N^C. In Figure 3.14 we have a contour plot of S_+^{LR} as a function L_S and L_N^C. One feature we immediately recover which we saw indications of in Fig. 3.4 is the existence of a “sweet spot” for the value of L_S which maximizes S_+^{LR}. This behavior of the NSNSN system, namely zero positivity in the noise cross-correlations for both very small and large values of L_S, appears to be a general feature of the NSNSN geometry. Also, Figure 3.14 shows a periodic-like relationship between S_+^{LR} and L_N^C, in which a series of peaks in S_+^{LR} is separated by troughs where S_+^{LR} is nearly zero. As we increase L_N^C the maximum value of S_+^{LR} increases accordingly. An interesting question for future analysis is whether the maximum values of S_+^{LR} continue to grow monotonically as we increase L_N^C further.

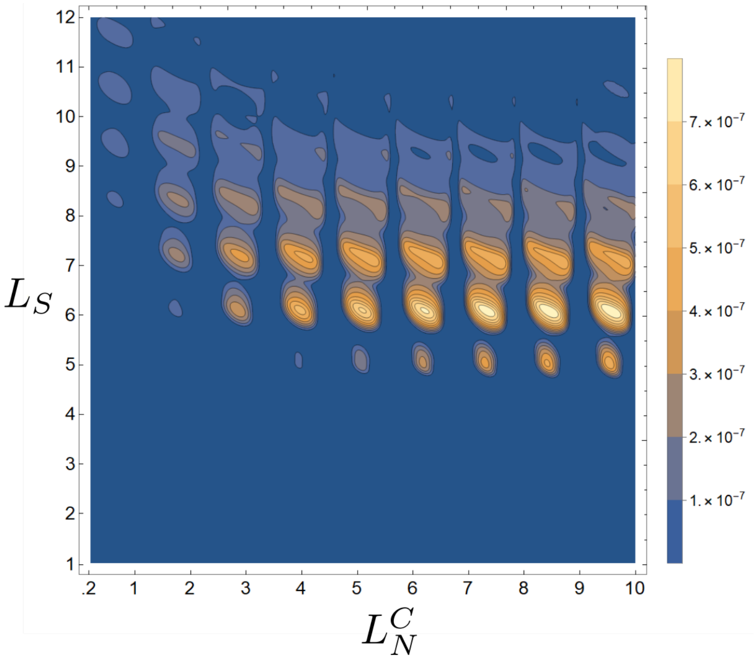

Figure 3.14: Area of the region of positive noise correlations, S_+^{LR}, as a function of the system size, with values of L_S along the y-axis and values of L_N^C along the x-axis.

3.8 Temperature Dependence

In Section 3.2 we explained that the choice of temperature $T_0 = 16.3K$ was based on ensuring that the transport was effectively restricted to the first transverse mode of the system (so as to simplify our calculations) balanced with the requirement that there was a nontrivial population of excitations throughout the full energy range comprising the first transverse mode of the system. The balancing of these two requirements can be seen in the Fermi distribution of the leftmost lead plotted in Figure 3.2. It is interesting to consider the cross-correlated noise of the system as we lower the temperature of the system.

In Figure 3.15(a) we show a plot of the cross-correlated shot noise as a function of both energy and system temperature, T_0, for temperatures ranging from $0K$ to $16.3K$, and for $L_N^C = 2.75\xi$, $L_S = 6\xi$ and $v_l = .1\Delta_0$. From Figure 3.15(a) we can see that the behavior of the cross-correlated noise energy distribution as a function of temperature breaks into roughly three regimes. At close to $T_0 = 16.3K$ the distribution is heavily dependent on the quasibound state located roughly halfway through the energy range of the system. At intermediate temperatures the population of excitations at energies near the quasibound state is suppressed and, while we still see a positive peak at the quasibound state as seen in Figure 3.15(b) for $T_0 = 8.15$K, the magnitude of that peak is nearly twenty times smaller than what was seen in Figure 3.6(b).

Finally, at very low temperatures we see a new behavior in which we have a positive peak in the shot noise distribution at energies just below the bias energy $v_l = .1\Delta_0$. This behavior is demonstrated in Figure 3.15(c), where we have set $T_0 = 1$K. This peak is not associated with any quasibound states of the system and can be traced back to a specific subcomponent of dS_{ph}^{LR}, $\Sigma_4 = -(F_h^L N_p^R + F_p^R N_h^L)\mathrm{Re}[r_{ph}^{LL*} r_{ph}^{RR*} t_{pp}^{LR} t_{hh}^{RL}]$, which is plotted alongside the total cross-correlated noise distribution in Figure 3.15(c). Using the classification scheme discussed in Section 3.6 the term $-(F_h^L N_p^R + F_p^R N_h^L)\mathrm{Re}[r_{ph}^{LL*} r_{ph}^{RR*} t_{pp}^{LR} t_{hh}^{RL}]$ corresponds to an EC-AR term. It was shown in [42, 43] that EC-AR terms in the cross-correlated noise correspond microscopically to a process called synchronized Andreev and inverse Andreev reflection (AR-$\overline{\text{AR}}$), a higher-order process in which an Andreev reflection (from particle to hole) at one interface and an inverse Andreev reflection (from hole to particle) at the other interface occur in a coherent fashion. Due to the simultaneous exchange of two fermions, the correlations resulting from this process can be boson-like, and as such positive.

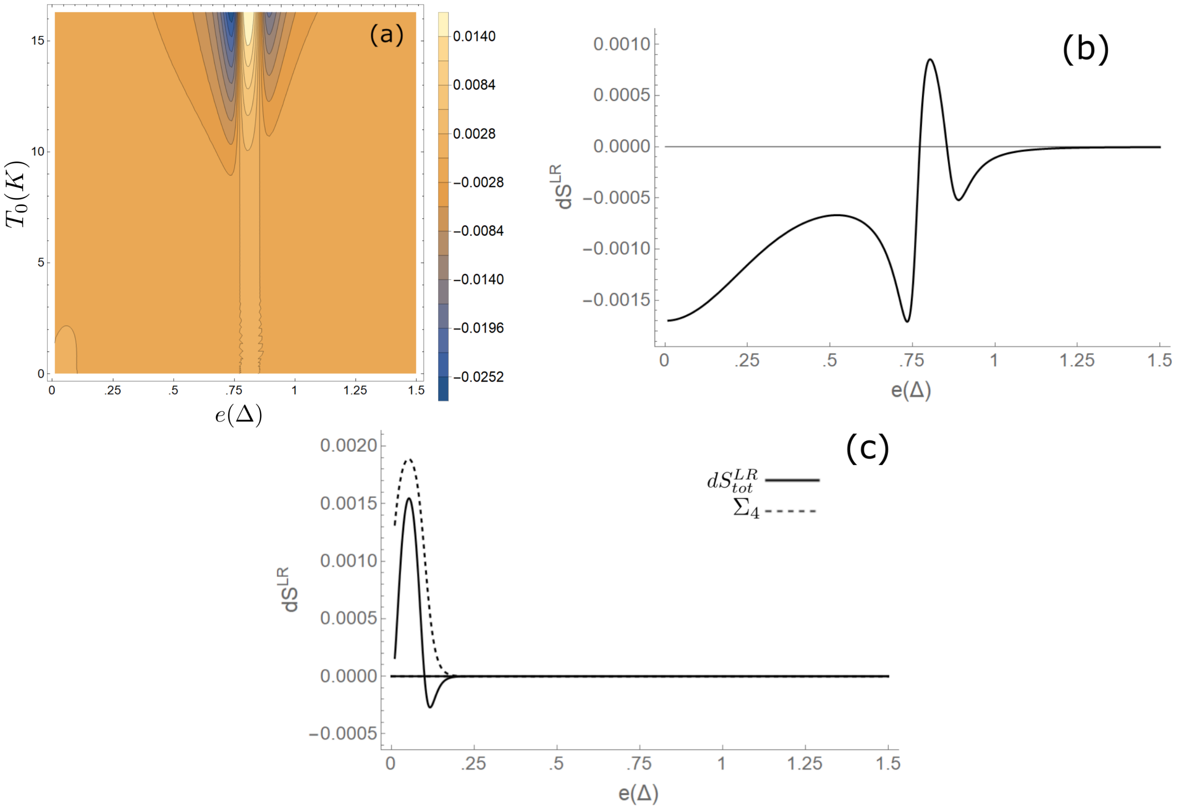

Figure 3.15: (a) Plot of the cross-correlated shot noise distribution as a function of the system temperature, T_0, and energy e with $L_N^C = 2.75\xi$ and $L_S = 6\xi$. (b) Cross-correlated shot noise distribution for $T_0 = 8.15$K. (c) Cross-correlated shot noise distribution for $T_0 = 1$K plotted alongside the subterm $\Sigma_4 = -(F_h^L N_p^R + F_p^R N_h^L)\mathrm{Re}[r_{ph}^{LL*} r_{ph}^{RR*} t_{pp}^{LR} t_{hh}^{RL}]$, which is the primary positive contribution.

3.9 The Andreev Approximation

We have so far presented results of the full scattering theory and thus far have not looked at the effect of applying the Andreev approximation [7]. We introduced the Andreev approximation in more detail in Section 1.2.4, but we will recap very briefly here. The Andreev approximation can be used if the ratio between the gap energy Δ_0 and the Fermi energy ϵ_f, $\frac{\Delta_0}{\epsilon_f}$, is sufficiently small that to good approximation we can drop higher order terms in the ratio $\frac{\Delta_0}{\epsilon_f}$ from the BdG equations, reducing them to a pair of coupled first-order differential equations known as the Andreev equations. In the high-transparency limit we consider here, this gives $r_{pp}^{LL} = r_{hh}^{LL} = r_{pp}^{RR} = r_{hh}^{RR} = 0$ as well as $t_{hp}^{LR} = t_{ph}^{LR} = t_{hp}^{RL} = t_{hp}^{RL} = 0$ in the scattering matrix (with the remaining scattering elements modified accordingly). With the Andreev approximation applied it is possible to write down the explicit expressions for the scattering elements, and they are given in Appendix B along with the simplified cross-correlated shot noise.

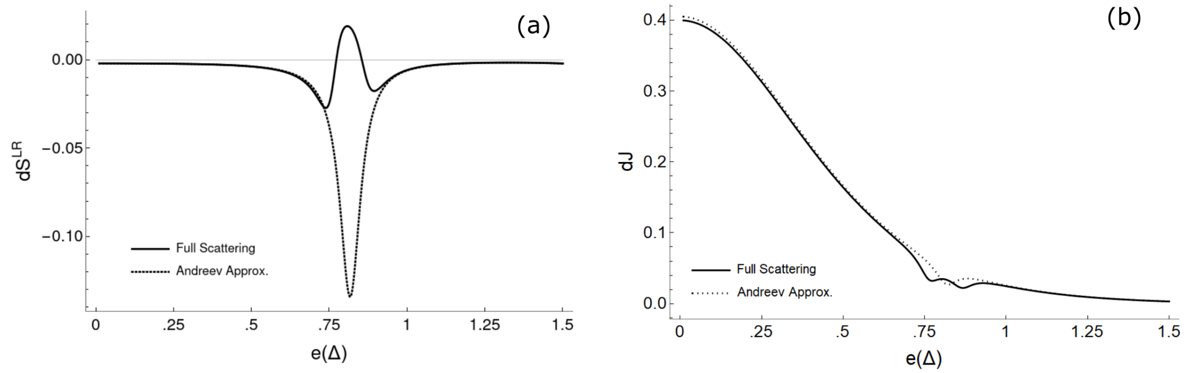

Figure 3.16: Comparison between the full scattering theory and results using the Andreev approximation. In (a) the differential cross-correlated shot noise and in (b) the magnitude of the current. While the results agree well away from the resonance, at the resonance we see that the Andreev approximation breaks down badly for the noise.

In Figure 3.16 we compare the cross-correlated shot noise and current distributions from the full scattering theory and using the Andreev approximation. Away from the resonance the results using the Andreev approximation are nearly indistinguishable qualitatively from the full scattering theory. At energies close to the resonance, however, we see from Figure 3.16(a) that the behavior of $dS^{LR}(e)$ strongly diverges. Whereas there is a clear positive peak in the noise distribution in the full scattering theory results, using the Andreev approximation the noise distribution remains purely negative and instead has a large negative dip at the resonance. The choice to use LSCO's parameters in our model system was motivated partly by it having one of the largest values of $\frac{\Delta_0}{\epsilon_f}$ among commonly studied superconductors, so it is an ideal substance for analyzing the Andreev approximation. The key issue here is the fact that the Andreev approximation treats terms such as $|t_{ph}^{LR}|$ and $|r_{pp}^{LL}|$ as negligible, while in reality these terms are nontrivial for the NSNSN system and are components of the main positive contributions to the cross-correlated noise, as seen in Figure 3.12.

There are also some qualitative differences to be found in the results for the quasibound states of the system. In Figure 3.17 we plot the poles of $|t_{pp}^{LR}|$ using the Andreev approximation. While the energy of this pole is comparable to what was found using the full scattering scattering theory in Figure 3.6(a), we now find only a single pole as opposed to the pair of poles.

3.10 Conclusions

In this chapter we studied the scattering properties and the current and cross-correlated shot noise distributions of an NSNSN system. We have obtained analytical expressions for the scattering matrix of the system without the Andreev approximation. We then used the scattering matrix elements to calculate the current and cross-correlated shot noise energy distributions and have used numerics to plot these quantities for a variety of system parameters. We find a one-to-one correspondence between the energies of quasibound states in the system and regions of positive correlations in the cross-correlated shot noise distributions. This connection between the positions of the quasibound states and the positive noise correlations is robust and is shown to be the case even as we introduce multiple quasibound states by increasing our system size.

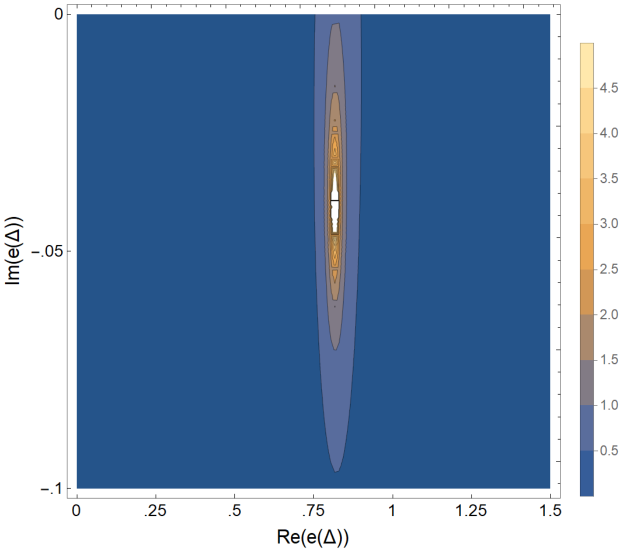

Figure 3.17: Quasibound state pole using the Andreev approximation. While at approximately the same energy, we do not see the double poles we did in Figures 3.6 and 3.7.

Moreover, we find that while the Andreev approximation gives strong qualitative agreement for the current and cross-correlated shot noise at energies away from the quasibound states, it breaks down notably at the quasibound state energies. We also find differences between the results of the full scattering theory and the Andreev approximation when looking at the poles of the scattering matrix in the complex energy plane.

Acknowledgments

This work was supported by the Robert A. Welch Foundation (Grant No. F-1051).

Part II

Quantum Circuit Simulation Using Signal Processing Based Hardware

Chapter 4

Signal Processing Based Special Purpose Quantum Circuit Simulation

4.1 Introduction

In 1980, Paul Benioff first introduced the concept of a quantum computer by demonstrating that a closed quantum system could be used to model the general process of computation [14]. The idea was later formalized by David Deutsch through the concept of a universal quantum computer as a generalization of a classical Turing machine [37]. Nearly a decade later, Peter Shor demonstrated that quantum computers could be used to factor large numbers more efficiently than any known classical algorithm and that such devices could be designed with fault tolerance [103, 104]. Quantum computers thereby offer a challenge to the strong Church-Turing thesis that one can do no better than a classical Turing machine [1, 114].

Current approaches to quantum computing are based on a variety of physical platforms, such as photonics, trapped ions, or superconducting circuits [85, 110]. All of these approaches rely upon maintaining a highly coherent quantum state through a series of gate operations in order to achieve a computational advantage. Preparing and manipulating such systems can be quite difficult, as small interactions with the environment quickly lead to decoherence of the state and, consequently, a significant loss in performance [57].

Among the most exciting recent developments in the field of quantum information is the rapid development of theoretical and experimental progress in demonstrating quantum computational supremacy. There are currently two leading proposals for demonstrating quantum computational supremacy, random circuit sampling (RCS) [3, 4], and boson sampling [2], specifically, the related offshoot gaussian boson sampling [48]. Both of these proposals have recently seen experimental demonstrations which appear to have successfully demonstrated the quantum computational supremacy of the underlying quantum systems. The demonstration of RCS was performed by the group of John Martinis at Google using 53 superconducting transmon qubits on their “Sycamore” chip [10]. Gaussian boson sampling was demonstrated with a maximum of 73 detected photons by the group of Jian-Wei Pan and Chao-Yang Liu at USTC using their reconfigurable Jiuzhang photonic device [126]. Both of these experiments are highly impressive, but they also highlight an important challenge in the development of large scale quantum computers operating in the quantum supremacy regime, verification and validation of the correctness of the quantum computer’s results. The most naive and straightforward approach to such a verification would be to directly calculate the full list of amplitudes for all possible output states and to use this to directly verify that the quantum computer is indeed sampling from the induced probability distribution. In Google’s paper, however, they showed that this naive approach to verification, using an algorithm such as the one proposed in [3], would take $\sim 10,000$ years using all of the RAM available on Oak Ridge National Lab’s Summit supercomputer. This was later refined by IBM Q in an analysis that showed that, in principle at least, this verification could be done in a few days by leveraging Summit’s secondary storage to store the full list of amplitudes on disk [92]. Regardless, it is clear that storage requirements, energy use—IBM did not include an estimate here, but using Summit’s rated power consumption of 13MW with IBM’s 60h estimated run time yields roughly 780MWH of energy consumption—and financial costs render such an approach to simulation and verification untenable for routine use at the scale of these early supremacy experiments.

Motivated by this insight, we have developed a novel approach to simulate quantum circuits using classical analog signal processing[1]. This approach uses a signal model which admits a Hilbert space descrip-

---

[1] The results in this chapter are based on the research paper: B. R. La Cour, C. Ostrove, G. Ott, M. J. Starkey and G. R. Wilson, *Classical emulation of a quantum computer*, International Journal of Quantum Information, **14**, 04 (2016). C. Ostrove ran the experiments, performed simulations and data analysis, generated the figures in Sections 4.3 and 4.4 and contributed to

tion that is mathematically equivalent to a multi-qubit, gate-based quantum computer [31]. Within this model, we have devised a novel scheme for addressing individual qubits, or groups of qubits, and applying gate operations upon them using analog electronic adders, multipliers, and filters. We furthermore have constructed a model of quantum measurement gates based on performing signal projection operations as well as phenomenological models based on amplitude threshold detections that are capable of simulating phenomena such as quantum contextuality and entanglement, important to quantum computing [64, 65]. Thus, using this approach it is possible to simulate any particular quantum computing algorithm or protocol, including Shor's factoring algorithm, Grover's search algorithm, fault-tolerant quantum error correction, and even quantum teleportation. Finally, a hardware demonstration system has been constructed that is capable of simulating a two-qubit quantum device.

We will discuss the practical considerations of this approach further in Section 4.5, but to be completely clear, just as existing digital quantum circuit simulations have exponential resource scaling in the form of, say, memory or computation time, the signal processing approach described in this chapter has exponentially scaling resource requirements in the form of the signal's bandwidth. Similarly, the complexity of the comb-like filters needed to perform the crucial subspace projection operation described in Section 4.2.3 scales similarly as we increase the number of qubits in our simulation. There are also challenges imposed by the intrinsic noisiness of the underlying analog hardware. Nonetheless, there are a number of intrinsic advantages to this approach as well, for example the ability to perform one and two-qubit gate operations in a single time step independent of the number of qubits in the simulation. Moreover, it has been projected that this approach would have substantially lower energy requirements as compared to a comparably sized digital simulation [31].

---

the writing of these sections. B. R. La Cour suggested and advised the experiments, and contributed most of the writing for the rest of the paper. M. J. Starkey and G. Ott contributed to the design and operation of the hardware prototype.

In Section 4.2 we describe the basic physical representation for our quantum simulation scheme and then turn to a hardware implementation of a two-qubit device in Section 4.3. The fidelity of this device is analyzed in Section 4.4, and the prospects for a larger-scale device are discussed in Section 4.5.

4.2 Physical Representation

This section describes the notional physical representation of quantum states and various gate operations. These are described in more detail elsewhere. [31] Here, we summarize the description for completeness and, later, turn to a specific hardware implementation. We begin with a description of the mathematical Hilbert space of an n-qubit quantum system, then relate these mathematical constructs to a classical, signal-based representation.

4.2.1 Hilbert Space Description

The state of an n-qubit quantum computer may be represented by an element $|\psi\rangle$ of a 2^n-dimensional Hilbert space $\mathcal{H}$ taking on the particular form of a tensor product of n two-dimensional Hilbert spaces $\mathcal{H}_0, \ldots, \mathcal{H}_{n-1}$ such that $\mathcal{H} = \mathcal{H}_{n-1} \otimes \cdots \otimes \mathcal{H}_0$, where $\otimes$ is the tensor product. A single element of one of the n constituent Hilbert spaces constitutes a qubit. The specification of an inner product $\langle \phi \rangle \, \psi$ between states $|\phi\rangle$ and $|\psi\rangle$ in $\mathcal{H}$ completes the Hilbert-space description.

We shall denote by $|0\rangle_i$ and $|1\rangle_i$ a pair of orthonormal basis states, termed the computational basis, for $\mathcal{H}_i$ and $i \in \{0, \ldots, n-1\}$. Taking tensor products of these individual basis states, we obtain a set of 2^n orthonormal basis states for the product space, $\mathcal{H}$. A particular binary sequence $x_0, \ldots, x_{n-1}$ therefore corresponds to a single basis state $|x_{n-1}\rangle_{n-1} \otimes \cdots \otimes |x_0\rangle_0$. For brevity, this binary sequence may be represented by its decimal form, $x = x_0 2^0 + \cdots + x_{n-1} 2^{n-1} \in \{0, \ldots, 2^n - 1\}$, so that the corresponding basis state may be written succinctly as $|x\rangle$ or, more explicitly, as $|x_{n-1} \cdots x_0\rangle$. Let $\langle x \rangle \, \psi = \alpha_x \in \mathbb{C}$ for a given state $|\psi\rangle \in \mathcal{H}$ and basis state $|x\rangle$. This state may then be written

$$|\psi\rangle = \sum_{x=0}^{2^n-1} \alpha_x |x\rangle \ . \tag{4.1}$$

4.2.2 Signal-based Representation

A key concept in our classical representation of a quantum state is the notion of *in-phase* and *quadrature* signals, which may be used to encode two distinct signals within one signal. Suppose we have a complex number $\alpha = a + jb$, with $a, b \in \mathbb{R}$. Physically, the real and imaginary values may be represented by, say, a pair of distinct direct current (DC) voltages. It is also possible to encode them in a single alternating current (AC) voltage signal $s(t)$ of carrier frequency $\omega_c > 0$ such that

$$s(t) = \text{Re}[\alpha e^{j\omega_c t}] = a\cos(\omega_c t) - b\sin(\omega_c t) \ . \tag{4.2}$$

Given $s(t)$, the parameters a and b can be recovered by the following procedure. First, we split the signal into two copies, then multiply each by $2\cos(\omega_c t)$ and $-2\sin(\omega_c t)$, respectively, to obtain

$$2\cos(\omega_c t)\, s(t) = a + \big[a\cos(2\omega_c t) - b\sin(2\omega_c t)\big] \tag{4.3a}$$

$$-2\sin(\omega_c t)\, s(t) = b - \big[b\cos(2\omega_c t) + a\sin(2\omega_c t)\big] \ . \tag{4.3b}$$

Multiplication by the quadrature components thus creates signals at the sum and difference frequencies $2\omega_c$ and 0 (i.e., DC). Low-pass filtering these two signals, then, yields the coefficients a and b, as desired.

A similar approach may be used to encode two complex numbers α and β, and hence a single qubit, using the complex quadrature signals $e^{j\omega_0 t}$ and $e^{-j\omega_0 t}$. Physically such a choice would, again, correspond to using two distinct real signals, each representing the real and imaginary parts, to realize the complex signal. With this “dual rail” representation, the corresponding complex signal is given by

$$\psi(t) = \alpha e^{j\omega_0 t} + \beta e^{-j\omega_0 t} \ . \tag{4.4}$$

As before, the coefficients α and β may be recovered (as pairs of DC voltages) by multiplying copies of $\psi(t)$ by $e^{-j\omega_0 t}$ and $e^{j\omega_0 t}$, respectively, and then low-pass filtering. Note that multiplication, in this case, is *complex* multiplication between two dual-rail signals, which results in a dual-rail output.

More generally, we may identify the single-qubit basis states $|0\rangle_i$ and $|1\rangle_i$, for qubit i, with the basis functions $\phi_0^{\omega_i}$ and $\phi_1^{\omega_i}$, where $\phi_0^{\omega_i}(t) = e^{j\omega_i t}$ and $\phi_1^{\omega_i}(t) = e^{-j\omega_i t}$ are the in-phase and quadrature signals, respectively. For n qubits, the basis state $|x\rangle$ is represented by the basis signal ϕ_x composed of a product of n single-qubit signals as follows:

$$\phi_x(t) = \phi_{x_{n-1}}^{\omega_{n-1}}(t) \ \cdots \ \phi_{x_1}^{\omega_1}(t) \ \cdot \ \phi_{x_0}^{\omega_0}(t) \ , \tag{4.5}$$

where $\phi_0^{\omega_i}(t)$ and $\phi_1^{\omega_i}(t)$ are defined above. Thus, function multiplication serves as a tensor product between qubits. Unlike the Kronecker product of matrices, though, the order is unimportant, as the qubits are distinguished by their distinct frequencies. Note that the spectrum of ϕ_x will consist of the 2^n sums and differences of the n component frequencies, which represent the Hilbert space. We refer to this description as the quadrature modulated tonals (QMT) representation.

By way of convention, we take $0 < \omega_0 < \cdots < \omega_{n-1}$, where $\omega_i = 2^i \omega_0$, and refer to this as the *octave spacing scheme*. The quantum state $|\psi\rangle$ can now be represented as a complex, n-qubit signal ψ which, at time t, is given by

$$\psi(t) = \sum_{x=0}^{2^n-1} \alpha_x \phi_x(t) \ . \tag{4.6}$$

For two such signals ϕ and ψ, the inner product is defined to be

$$\langle \phi \rangle \, \psi = \frac{1}{T} \int_0^T \phi(t)^* \psi(t) dt \ , \tag{4.7}$$

where T is a multiple of the period $2\pi/\omega_0$ of the signal. Note that the inner product corresponds to a low-pass filter, and $\langle \phi_x \rangle \, \psi = \alpha_x$ represents a pair of DC values giving the components of the quantum state for the $|x\rangle$ basis state. This completes the Hilbert space description, thereby demonstrating the mathematical equivalence of this representation to that of a multi-qubit quantum system.

4.2.3 Gate Operations

In our approach, subspace projections are used for performing gate operations. Given a quantum state $|\psi\rangle \in \mathcal{H}$, we can mathematically decompose it into the two orthogonal subspaces corresponding to, say, qubit i as follows:

$$|\psi\rangle = \Pi_0^{(i)} |\psi\rangle + \Pi_1^{(i)} |\psi\rangle = |0\rangle_i \otimes \left|\psi_0^{(i)}\right\rangle + |1\rangle_i \otimes \left|\psi_1^{(i)}\right\rangle \ , \tag{4.8}$$

where $\left|\psi_0^{(i)}\right\rangle$ and $\left|\psi_1^{(i)}\right\rangle$ are the $(n-1)$-qubit *partial projection* states.

A linear gate operation on a single qubit may be represented by a complex 2×2 matrix U, where

$$U = \begin{pmatrix} U_{0,0} & U_{0,1} \\ U_{1,0} & U_{1,1} \end{pmatrix} \ . \tag{4.9}$$

If U acts on qubit i of state $|\psi\rangle$, then the transformed state is

$$|\psi'\rangle = \Big[U_{0,0}\,|0\rangle_i + U_{1,0}\,|1\rangle_i\Big] \otimes \left|\psi_0^{(i)}\right\rangle + \Big[U_{0,1}\,|0\rangle_i + U_{1,1}\,|1\rangle_i\Big] \otimes \left|\psi_1^{(i)}\right\rangle \tag{4.10}$$

Thus, the gate operation is applied only to the addressed qubit basis states, not to the partial projections. This, of course, is only a mathematical operation. A physical method of construction is needed to realize the transformation.

In our QMT representation, a pair of complex signals $\psi_0^{(i)}(t)$ and $\psi_1^{(i)}(t)$ corresponding to the partial projection states $\left|\psi_0^{(i)}\right\rangle$ and $\left|\psi_1^{(i)}\right\rangle$ are produced by taking the initial complex signal $\psi(t)$, multiplying copies of it by $\phi_0^{\omega_i}(t)$ and $\phi_1^{\omega_i}(t)$, respectively, and passing them through a pair of specialized bandpass filters that output the desired projection signals [31]. Given this pair of complex signals, along with the complex, single-qubit basis signals $\phi_0^{\omega_i}(t)$ and $\phi_1^{\omega_i}(t)$, we may construct the transformed signal $\psi'(t)$ using analog multiplication and addition operations as follows:

$$\psi'(t) = \Big[U_{0,0}\,\phi_0^{\omega_i}(t) + U_{1,0}\,\phi_1^{\omega_i}(t)\Big]\psi_0^{(i)}(t) + \Big[U_{0,1}\,\phi_0^{\omega_i}(t) + U_{1,1}\,\phi_1^{\omega_i}(t)\Big]\psi_1^{(i)}(t)\ . \tag{4.11}$$

Two-qubit gate operations, such as Controlled NOT (CNOT) gates, may be constructed similarly.

Importantly, this approach to performing gate operations requires only a single subspace decomposition of the original signal into two constituent signals and does not require a full spectral decomposition, as would be required if one were performing an explicit matrix multiplication operation over the entire 2^n-component state. This approach provides a significant practical advantage to implementation and more closely emulates the intrinsic parallelism of a true quantum system.

4.2.4 Measurement Gates

The procedure for performing measurements is quite similar to that for performing gate operations. To perform a measurement on, say, qubit i, we construct the partial projection signals $\psi_0^{(i)}(t)$ and $\psi_1^{(i)}(t)$, as before, and measure their root-mean-square (RMS) values, given by

$$q_0^{(i)} = \frac{1}{T}\int_0^T \left|\psi_0^{(i)}(t)\right|^2 dt\ , \quad q_1^{(i)} = \frac{1}{T}\int_0^T \left|\psi_1^{(i)}(t)\right|^2 dt\ . \tag{4.12}$$

This can be done most easily by adding the real and imaginary parts of, say, $\psi_0^{(i)}(t)$, measuring the RMS value of the sum, and then squaring the result, since

$$\frac{1}{T}\int_0^T \Big[\mathrm{Re}\,\psi_0^{(i)}(t) + \mathrm{Im}\,\psi_0^{(i)}(t)\Big]\,dt = q_0^{(i)}\ . \tag{4.13}$$

According to the generalized Born rule, the outcomes 0 and 1 occur with probability $p_0^{(i)} \propto q_0^{(i)}$ and $p_1^{(i)} \propto q_1^{(i)}$, and these probabilities may be computed explicitly through analog sum and division operations. For each such qubit measurement, a random input DC voltage representing a random number u_i, chosen uniformly in the interval $[0,1]$, may be input to a comparator device such that when $u_i > p_0^{(i)}$ a binary outcome of 1 is obtained with a probability given by the Born rule.

To measure a second qubit, the same procedure is followed but using the (unnormalized) "collapsed" state $\Pi_0^{(i)} |\psi\rangle$ or $\Pi_1^{(i)} |\psi\rangle$, depending upon whether outcome 0 or 1, respectively, was obtained in the first measurement. The selection of the collapsed state may be implemented through a simple switch controlled by the binary measurement output. This procedure may be repeated until all n qubits are measured. Doing so results in an n-bit digital output whose distribution follows the quantum mechanical predictions, at least to the limits of hardware fidelity.

4.3 Hardware Implementation

The results of this chapter come from an early hardware prototype device capable of initializing the system into an arbitrary two-qubit state and operating using a universal set of gate operations. In Chapter 5 we will present results based on a later prototype. A picture of the hardware setup is shown in Figure 4.1. We use a signal generator to produce a baseline 1000 Hz tonal, from which all other signals are generated and thereby phase coherent. The lower frequency qubit, labeled B, is taken from the signal generator, with a separate, 90-degree phase-shifted signal used to represent the imaginary component. The higher frequency qubit, labeled A, is derived from qubit B via complex multiplication, which results in frequency doubling. Thus, $\omega_A = 2\pi(2000 \text{ Hz})$ and $\omega_B = 2\pi(1000 \text{ Hz})$. The two single-qubit signals are multiplied to produce the four basis signals $\phi_{00}(t) = e^{j(\omega_A+\omega_B)t}$, $\phi_{01}(t) = e^{j(\omega_A-\omega_B)t}$, $\phi_{10}(t) = e^{j(-\omega_A+\omega_B)t}$, and $\phi_{11}(t) = e^{j(-\omega_A-\omega_B)t}$ centered at frequencies $+3000$ Hz, $+1000$ Hz, -1000 Hz, and -3000 Hz, respectively.

State synthesis is performed by multiplying these four basis signals by four complex coefficients α_{00}, α_{01}, α_{10}, and α_{11}, each represented by pairs of DC voltages, and adding the results to produce the final, synthesized signal $\psi(t)$ representing the quantum state $|\psi\rangle$. An example of a synthesized signal is given in Fig. 4.2, which shows the ideal pair of signals, representing the real and imaginary parts of $\psi(t)$, and the recorded signals generated in the hardware. In this example, the state is specified by the complex coefficients

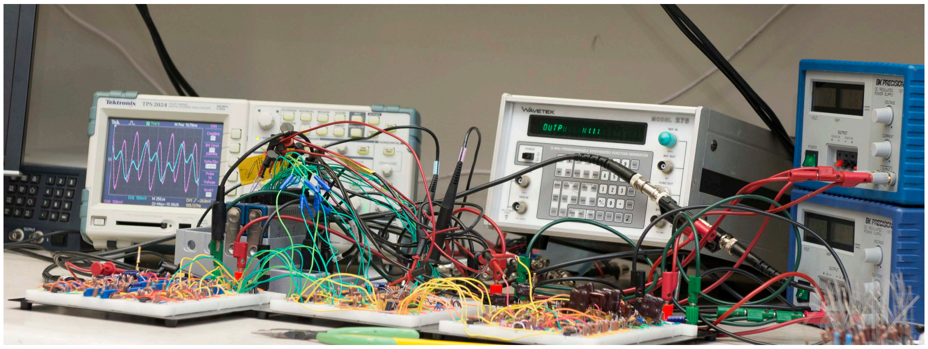

Figure 4.1: Photograph of an early prototype hardware setup. The three breadboards correspond to basis signal generation (left), state synthesis (center), and gate operations (right). The devices in the background are an oscilloscope (left), a signal generator (center), and a DC power supply (right). The electronics are interfaced via a desktop computer (to the left, not shown).

$\alpha_{00} = 0.6579 - 0.2895j$, $\alpha_{01} = 0.5385 + 0.1383j$, $\alpha_{10} = -0.2280 + 0.3953j$, and $\alpha_{11} = -0.2460 - 0.4277j$.

To implement gate operations, we use a set of analog four-quadrant multipliers, filters and operational amplifiers to realize the mathematical operations described previously. For example, to perform a gate operation on qubit A, we use a pair of low-pass filters to remove the 2000 Hz component from $e^{\pm j\omega_A t}\psi(t)$. The resulting partial projections $\psi_0^{(A)}(t)$ and $\psi_1^{(A)}(t)$ are a pair of 1000 Hz signals corresponding to qubit B. To perform the gate operation, we take a matrix U, given by, say,

$$U = \begin{bmatrix} U_{00} & U_{01} \\ U_{10} & U_{11} \end{bmatrix} = \begin{bmatrix} 0.1759 + 0.1836j & 0.4346 + 0.8460j \\ -0.4346 + 0.8640j & 0.1759 - 0.1836j \end{bmatrix} \tag{4.14}$$

and use it to construct two qubit-A signals of the form $U_{00}e^{j\omega_A t} + U_{10}e^{-j\omega_A t}$ and $U_{01}e^{j\omega_A t} + U_{11}e^{-j\omega_A t}$. These, in turn, are multiplied by the corresponding partial projections and added to form the final signal $\psi'(t)$, given by

$$\psi'(t) = \left(U_{00}e^{j\omega_A t} + U_{10}e^{-j\omega_A t}\right)\psi_0^{(A)}(t) + \left(U_{10}e^{j\omega_A t} + U_{11}e^{-j\omega_A t}\right)\psi_1^{(A)}(t)\ . \tag{4.15}$$

The resulting output using the gate specified in Equation 4.14 applied to the signal in Figure 4.2 is shown in Figure 4.3.

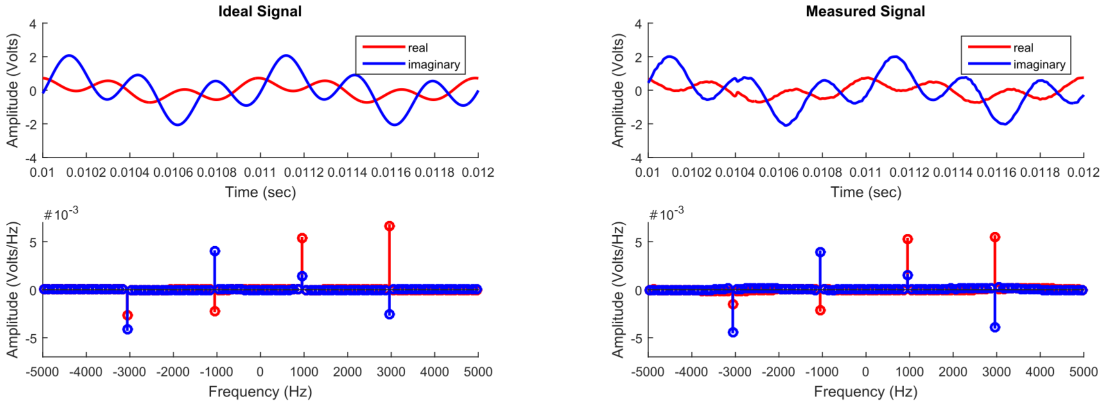

Figure 4.2: Plot of two complex signals representing a quantum state with coefficients $\alpha_{00} = 0.6579 - 0.2895j$, $\alpha_{01} = 0.5385 + 0.1383j$, $\alpha_{10} = -0.2280 + 0.3953j$, and $\alpha_{11} = -0.2460 - 0.4277j$. The left plot shows the ideal signal, while The right plot shows that recorded signal generated by the hardware. The colors red and blue indicate the real and imaginary parts, respectively. The top plots show the time-domain signals, while the bottom plots show the frequency-domain signals.

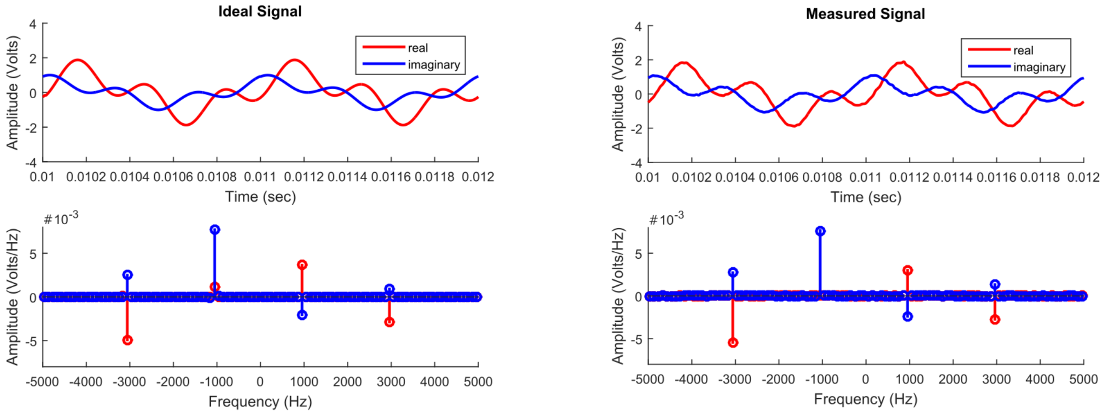

Figure 4.3: Plot of two complex signals representing the output of a quantum gate operation. The input signal is that shown in Figure 4.2, and the gate, operating on qubit A, is given by Equation 4.14.

4.4 Fidelity Analysis

The quality of a quantum state or gate operation is typically measured in terms of the gate fidelity, which is a number between 0 and 1, where 1 is ideal. For an ideal state $|\psi\rangle$ and recorded state $\left|\hat{\psi}\right\rangle$, the fidelity is

$$F(\hat{\psi},\psi) = \frac{|\langle\hat{\psi}|\psi\rangle|}{\|\hat{\psi}\|\,\|\psi\|}\ . \tag{4.16}$$

Using this definition, we can measure the fidelity of a state synthesis or gate operation over an ensemble of random realizations.

As an illustration, we performed synthesis of the entangled singlet state $|\psi\rangle = [|01\rangle - |10\rangle]/\sqrt{2}$ and examined the fidelity of the signal used to emulate this state (just prior to performing a gate operation on it). Using Equation 4.16, we compared the ideal quantum state to the actual signal, using the recorded signal to compute the inner product $\langle\hat{\psi}\rangle\,\psi$ and the normalization $\|\hat{\psi}\|$. Figure 4.4 shows the results of this analysis, where a histogram of fidelity over 500 realizations of the signal is shown. In this example, we find a mean state fidelity of $0.991 \approx 99\%$.

The definition of fidelity given by Equation 4.16 assumes a pure initial and final state; in general, the states may be mixed. A mixed state may be thought of as a random ensemble of pure states; for n-qubit states a mixed state may be represented by a $2^n \times 2^n$ positive semidefinite matrix ρ. In our classical simulation, a single pure state is always realized and can be known, but in a true quantum system this is not so. Instead, one must infer the quantum state through a variety of measurements. One widely accepted approach uses quantum state tomography (QST) to estimate the quantum state from a complete set of orthonormal measurements. In our case, we use the 16 pair-combinations of four Pauli spin matrices, normalized to unity with respect to the Hilbert-Schmidt inner product [84]. To fairly compare our system with a true quantum system, then, we can also perform QST to obtain an estimated quantum state $\hat{\rho}$ and

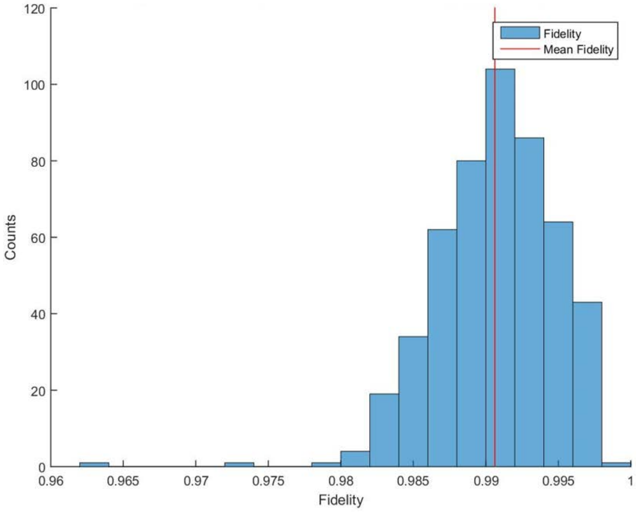

Figure 4.4: Histogram of signal fidelity for 500 realizations of an initial entangled state of the form $|\psi\rangle = [|01\rangle - |10\rangle]/\sqrt{2}$. The mean fidelity, indicated by the red vertical line, is about 0.991.

thereby compute the fidelity compared to the ideal quantum state $\rho = |\psi\rangle\langle\psi|$ using the formula [56]

$$F(\hat{\rho}, \rho) = \frac{\mathrm{Tr}\left(\sqrt{\sqrt{\rho}\,\hat{\rho}\sqrt{\rho}}\right)}{\sqrt{\mathrm{Tr}(\rho)\,\mathrm{Tr}(\hat{\rho})}} \,. \tag{4.17}$$

These measurement outcomes are in a maximum likelihood QST calculation to obtain the estimated quantum state ρ' and, from this, the measured fidelity $F(\rho', \rho)$ [5, 63, 65]. For the ideal singlet state and a sample size of 1000, for example, we obtained a measured fidelity of about $0.998 \approx 99\%$, comparable to what was found earlier through a direct calculation of $F(\psi', \psi)$.

A similar technique was used to measure gate fidelity. Given a pure singlet state, we applied a random ensemble of unitary gates on qubit A. For each realization of a gate U, the ideal quantum state is $|\psi'\rangle = U|\psi\rangle$. If we denote the recorded state by $\hat{\psi}'$, then the gate fidelity will be $F(\hat{\psi}', \psi')$. The results for this example are summarized in Figure 4.5 where, over an ensemble of 500 runs, a mean fidelity of $0.989 \approx 99\%$ was obtained.

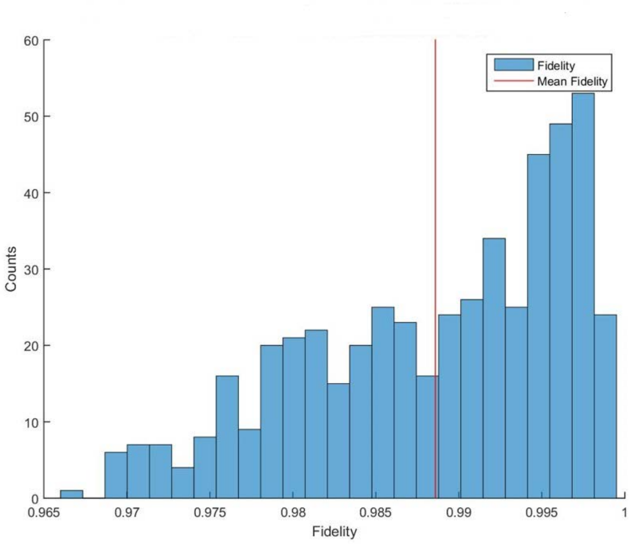

Figure 4.5: Histogram of gate fidelity for a random set of 500 unitary gates applied to qubit A on an initial entangled state of the form $|\psi\rangle = [|01\rangle - |10\rangle]/\sqrt{2}$. The mean fidelity, indicated by the red vertical line, is about 0.989.

4.5 Practical Considerations

The device as currently implemented is limited to two qubits. Additional qubits are straightforward to implement but require additional bandwidth that scales exponentially with the number of qubits. The complexity of the filters needed to perform the subspace projection operations increases similarly. Using current integrated circuit technology, a device of up to 20 qubits could easily fit on single chip, while 40 qubits would seem to be a practical upper limit [31].

Current development efforts are focused on building a set of programmable one- and two-qubit gates. Once these are completed, we will have the ability to initialize an emulated quantum state and operate on it with a programmable sequence of universal gates to execute any particular quantum computing algorithm. Future work will focus on scaling up the number of qubits and migrating from a simple breadboard setup to a more sophisticated, chip-based implementation. Classical error sources, such as additive noise, can be modeled as a quantum operations, such as a depolarizing channel, and this is discussed in the next chapter.

We envision a device based on the concepts described above that would interface with a traditional digital computer and serve as an analog co-processor, much as is done in our current prototype. Thus, a digital computer, tasked with solving a particular problem, perhaps as a subroutine to a larger computation, would designate an initial quantum state and sequence of gate operations to be performed on this state through a digital-to-analog converter (DAC) interface. The co-processor would produce a final state (i.e., a signal) which would then be subject to a sequence of measurement gate operations. The result would be a particular binary outcome, which would then be reported back to the digital computer via an analog-to-digital (A/D) converter.

The price paid for the computational efficiency of the analog co-processor lies in the hardware complexity needed to implement the device. Each single-qubit projection operation on an n-qubit state requires a pair of distinct, comb-like filters with $2^n/4$ (positive) passband frequencies, while each two-qubit operation requires the ability to perform $n(n-1)$ different projection operations. A key part of the development for a larger scale device would consist of the design of tunable bandpass filters with multiple nulls for the subspace projection operations.

The number of qubits will also be limited by the available bandwidth and the lowest frequency ω_0 (or period T) of the signal. Under the octave spacing scheme, n qubits would require a frequency band from ω_0 to $2^n\omega_0$. Each gate operation would require a time $\mathcal{O}(T)$ to complete, and any useful algorithm would have a number of gates that grows only polynomially in n. Thus, for a base qubit frequency of, say, 1 MHz, a single gate operation acting simultaneously on all 2^{10} digital states of a 10-qubit signal would take about $T = 1$ μs. If we compare this to a nominal single-core, 1 GHz digital processor, the time to process all $N = 2^{10} \sim 10^6$ inputs would also be about 1 μs. Thus, a mere 10 qubits would give a processing step time comparable to that of a modern digital processor.

Acknowledgments

This work was supported by an Internal Research and Development grant from Applied Research Laboratories, The University of Texas at Austin. Additional support was provided by the Office of Naval Research under Grant No. N00014-14-1-0323.

Chapter 5

Improving the Performance of a Signal Based Quantum Circuit Simulator Using Quantum Error Correction

5.1 Introduction

Underlying the usefulness of quantum systems for information processing is the ability to scale up what are now small laboratory scale prototype devices to the sizes necessary for addressing problems that cannot already be tackled with classical hardware. Before the discovery of techniques for performing quantum error-correction (QEC), it was thought that the inherent fragility of quantum coherent systems would make scaling up to these sizes virtually impossible in practice. This was not unlike the situation in the early days of digital computing, when real-time error correction techniques were first contemplated [94]. Beginning with the discovery of Shor's famous 9-qubit code in 1994, and followed by subsequent advances within the field of QEC, a path towards large-scale fault-tolerant quantum computers now exists [39, 75].

Experimental implementations of many of the components that go into the performance of QEC protocols have been tested for most of the potential candidate platforms for quantum computing. Ion-trap quantum computing experiments have been performed that tested the performance of a three-qubit stabilizer code using a system comprised of the hyperfine levels of three trapped beryllium atoms with intentionally induced errors and found a reduction in the gate error by as much as 0.3 for large error probabilities [27]. Further ion-trap experiments have looked at multiple rounds of QEC using the three-qubit phase-flip code on a system of three calcium ions under the influence of intentionally induced errors between each round, which found a degradation in fidelity consistent with first-order insensitivity to induced errors [101]. Experiments performed using logical qubit states encoded as "cat-states" of a superconducting quantum oscillator reported a 10% enhancement in coherence time using QEC over the longest lived physical qubit comprising the composite system and a factor of 20 times longer than the shortest lived component (a transmon qubit) [87]. A demonstration of a universal set of one-qubit gate operations acting on logically encoded qubit states in a superconducting quantum oscillator has shown an average fidelity for logical gate operations of 0.985 [49]. For superconducting transmon qubits experimental tests have verified first-order insensitivity to induced phase-flip and bit-flip errors using three-qubit repetition codes; however those same experiments also found that for low error probability the overhead of QEC actually reduced overall performance [95]. Experiments on transmons have also demonstrated the implementation of stabilizer measurements of the type necessary for the fault-tolerant implementation of QEC with stabilizer codes [96]. Recent experiments on transmon qubits have also demonstrated a reduction in the failure rate of input state retrieval by as much as a factor of 8.5 using multiple rounds of QEC as compared to rates for unencoded qubits [59].

In nuclear magnetic resonance (NMR) systems, experimental tests of logical operations on a system of five nuclear spins encoded in the 5-qubit Perfect code in the presence of induced errors found that the average gate performance was enhanced relative to what would be expected for an unencoded qubit subject to the same noise [125]. Furthermore, experiments on NMR systems have also demonstrated an improvement using QEC for a system subjected to phase noise and encoded in a 3-qubit phase-flip repetition code [19]. In nitrogen vacancy center qubits, an experimental implementation of the 3-qubit phase-flip code under the influence of induced noise found a reduction in error for large induced-error probabilities [32]. Finally, in photonic systems, tests have been performed using both single-photon and continuous-variable (CV) settings. In the CV setting, an experimental test of a CV generalization of the Shor 9-qubit code in the presence of induced noise found an enhancement using QEC for each of the induced error modes [8]. In the single-photon setting experimental tests of a simple code for protection from coherence loss from spurious Z basis measurements was found to recover the original state following intentionally induced measurements with a fidelity of 0.98 [78]. Additionally, an experiment using a 4-qubit code designed to protect from photon loss errors in a single photon system recovered from induced photon loss errors with a fidelity of 0.80 [93].

A number of analogies are often drawn between quantum mechanical systems and classical analog systems [40]. A key distinction made with regard to computing is that, under certain assumptions, a scalable quantum computer is capable of satisfying the threshold theorem for fault tolerance [1]. In previous work we have shown how one may explicitly embed the same Hilbert space structure found in a gate-based quantum computer directly into a signal processing framework in which information is represented using complex, basebanded analog voltage signals [68]. This analogy allows for a rich set of connections to be drawn between problems in both signal processing and quantum computing applications. In a separate work, for example, we have shown how this mathematical connection can be leveraged to incorporate techniques developed for QEC to solve problems in digital wireless communications [73]. A prototype quantum emulation device (QED) that utilizes this embedding and physically performs the operations described in hardware has been developed and tested [67]. A natural question to ask given this device is whether it is possible to utilize techniques from QEC to enhance the performance of what is otherwise a purely classical analog device. On a practical level this is an interesting question for multiple reasons. Firstly it is believed that error correction in analog devices is very difficult, and the difficulty of this problem has long stymied advances in technologies that rely on analog data processing and collection [120]. Secondly, it is not clear that QEC should work on a classical analog device at all. Regardless of our embedding scheme, the device dynamics are governed purely by classical physics and, as such, the assumptions inherent in QEC's formulation, such a linearity of errors, are not necessarily justified. In Section 5.2 we discuss a simple example (additive white Gaussian noise) where it is possible to directly express the classical errors in the quantum formalism. In this work we demonstrate that in practice, despite the above caveats, QEC protocols do in fact provide additional robustness to noise in our system and improve its performance overall[1].

5.2 Modeling Classical Errors as Quantum Operations

In order to effectively make use of QEC techniques in our alternative setting it is useful to first recast the modeling of our system's error dynamics into the same mathematical framework used in the quantum mechanical setting. Quantum operations provide one such framework and are used to model the evolution of noisy quantum system dynamics. The quantum operations formalism provides the tools needed to describe the evolution of open quantum systems, those coupled to external environmental degrees of freedom, along with the apparent non-unitary system evolution that can occur. The mapping $\rho \mapsto \mathcal{E}(\rho)$ is a superoperator that maps the input density operator ρ acting on a Hilbert space $\mathcal{H}$ to the final density operator $\mathcal{E}(\rho)$, here taken to be also acting on $\mathcal{H}$, and is called the quantum operation or, for trace-preserving maps, the quantum channel [86].

Quantum operations can be described using the operator-sum representation in which the evolution of the system is specified by a discrete set $\{E_k\}$ of operators on the Hilbert space, called the Kraus operators [60]. In this formulation, the quantum operation takes the form

$$\mathcal{E}(\rho) = \sum_k E_k \rho E_k^\dagger \ . \tag{5.1}$$

where, for a trace-preserving quantum channel, $\sum_k E_k E_k^\dagger = I$ is the identity.

Operators from the Pauli group are an example of Kraus operators. The Pauli group for a system of n qubits is given by the set of all n-fold tensor products of the one-qubit Pauli matrices $\sigma_0 = I$, $\sigma_1 =$

---

[1] The results in this chapter are based on the research paper: C. Ostrove, B. La Cour, S.A. Lanham and G. Ott, *Improving performance of an analog electronic device using quantum error correction*, Journal of Physics Communications, **3**, 8 (2019). C. Ostrove designed the experiments, wrote the code for and performed the data analysis, generated the figures and performed a substantial portion of the writing. B. La Cour suggested the project, advised the developmental design and shared in the writing and revision process. S.A. Lanham and G. Ott contributed to the design and operation of the hardware prototype, including the implementation of the additional qubits needed for the larger experiments.

X, $\sigma_2 = Y$, $\sigma_3 = Z$. The Pauli group on n qubits forms a complete basis for $2^n \times 2^n$ matrices, so it is always possible to rewrite the operator-sum representation of a quantum operation in a canonical form by rewriting the operation elements as linear combinations of Pauli group elements [86].

The depolarizing channel is a prototypical channel within the QEC literature. Correcting depolarizing errors on a number of qubits is as hard as correcting arbitrary errors on those qubits and, so, it is a simple and useful stand-in [86]. For the purposes of error correction in classical analog systems, the depolarizing channel is of particular interest because it can be shown to directly correspond to the presence of additive Gaussian white noise (AWGN) in a system [66]. The depolarizing channel is a noise process in which with some probability p we lose all information about the state of our system and it is replaced with the maximally mixed state I/N where $N = 2^n$ is the dimension of the system. As a quantum operation we can write the generalized depolarizing channel as follows:

$$\mathcal{E}(\rho) = (1-p)\rho + \frac{p}{N} I \ . \tag{5.2}$$

Making use of the identity

$$I = \frac{1}{N} \sum_{m_1=0}^{3} \cdots \sum_{m_n=0}^{3} \sigma_{m_1} \otimes \cdots \otimes \sigma_{m_n} \, \rho \, \sigma_{m_1} \otimes \cdots \otimes \sigma_{m_n} \ , \tag{5.3}$$

the depolarizing channel can be written in the operator-sum representation. For the one-qubit case, this is given by

$$\mathcal{E}(\rho) = (1-p')I\rho I + \frac{p'}{3}\left(X\rho X + Y\rho Y + Z\rho Z\right) \ , \tag{5.4}$$

where $p' = 3p/4$.

To see the connection to AWGN suppose the quantum state $|\psi\rangle$ is represented by the time-domain signal ψ given by

$$\psi(t) = \sum_{x=0}^{N-1} \phi_x(t) \langle x|\psi\rangle = \sum_{x=0}^{N-1} \langle x|\psi\rangle \exp\left[i \sum_{k=1}^{n} (-1)^{x_k} \omega_k t \right] \ , \tag{5.5}$$

where $x = x_{n-1}2^{n-1} + \cdots + x_0 2^0$ and $\omega_k = 2^k \omega_0$ for some $\omega_0 > 0$. Additive noise produces a stochastic signal $\tilde{\psi} = \psi + w$, where w is a zero-mean complex white Gaussian noise process with spectral density σ^2 such that $\mathsf{E}[w^*(t)w(t')] = \sigma^2\delta(t-t')$, where E represents an expectation value. Note that $\tilde{\psi}$ is outside the Hilbert space of ψ since w is a broadband signal. Projecting $\tilde{\psi}$ back into this space, which is done by narrowband filtering, yields a quantum state of the form $\left|\tilde{\psi}\right\rangle \propto |\psi\rangle + |\nu\rangle$. Here, $|\nu\rangle$ is represented by a stochastic signal given by

$$\nu(t) = \sum_{x=0}^{N-1} \phi_x(t) \langle x|w\rangle = \sqrt{\frac{\sigma^2}{T}} \sum_{x=0}^{N-1} z_x \phi_x(t) \ , \tag{5.6}$$

where T is a multiple of $2\pi/\omega_0$, $\{z_x\}_x$ are independent standard complex Gaussian random variables, and we have used the inner product definition

$$\langle x|w\rangle = \frac{1}{T}\int_0^T \phi_x(t)^* w(t)\, dt \ . \tag{5.7}$$

The corresponding quantum channel may be found by taking the expectation value of the outer product $\left|\tilde{\psi}\right\rangle\left\langle\tilde{\psi}\right|$. Since

$$\mathsf{E}[\langle x|\tilde{\psi}\rangle \langle\tilde{\psi}|x'\rangle] = \langle x|\psi\rangle \langle\psi|x'\rangle + \frac{\sigma^2}{T}\mathsf{E}[z_x z_{x'}^*] = \langle x|\psi\rangle \langle\psi|x'\rangle + \frac{\sigma^2}{T}\delta_{xx'} \ , \tag{5.8}$$

we deduce that the quantum channel is given by

$$\mathcal{E}(\rho) = \left(1 + \frac{N\sigma^2}{T}\right)^{-1} \left[\rho + \frac{\sigma^2}{T} I\right] \ . \tag{5.9}$$

which is of the same form as equation 5.2. This shows how a classical noise process, in this case additive white Gaussian noise, can be described by an equivalent quantum operation.

5.3 Description of the QEC Protocol

For our experiment we used the 5-qubit Perfect code, which is the smallest code capable of correcting an arbitrary error on a single physical qubit [69]. The 5-qubit code is a stabilizer code with the generators given in table 5.1.

Table 5.1: Generators for the stabilizer group of the 5-qubit Perfect code.

$M_0 = Z_1 X_2 X_3 Z_4$

$M_1 = Z_0 Z_2 X_3 X_4$

$M_2 = X_0 Z_1 Z_3 X_4$

$M_3 = X_0 X_1 Z_2 Z_4$

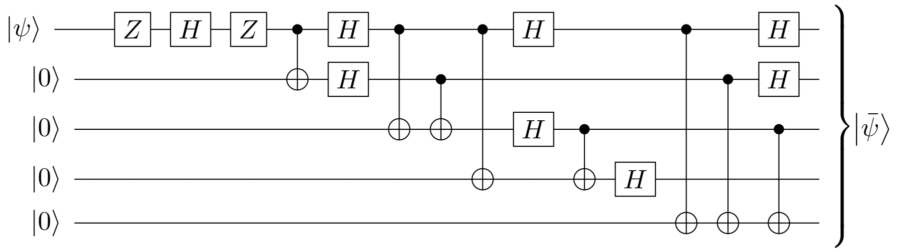

Figure 5.1: Circuit for encoding states into the 5-qubit Perfect code. The qubits are numbered 0 to 4 from top to bottom.

To encode the logical single-qubit state $|\psi\rangle = \alpha\,|0\rangle + \beta\,|1\rangle$ into the physical state $|\bar{\psi}\rangle = \alpha\,|\bar{0}\rangle + \beta\,|\bar{1}\rangle$, we use the code words

$$|\bar{0}\rangle = \frac{1}{4}(I + M_0)(I + M_1)(I + M_2)(I + M_3)\,|00000\rangle \tag{5.10}$$

$$|\bar{1}\rangle = \frac{1}{4}(I + M_0)(I + M_1)(I + M_2)(I + M_3)\,|11111\rangle\,, \tag{5.11}$$

where a little endian qubit numbering convention (0 to 4, read right to left) is adopted. The encoding circuit is given in figure 5.1.

In addition to the encoding circuit, we also need the corresponding syndrome detection circuit. To perform syndrome detection we use a fault-tolerant circuit construction introduced by DiVincenzo and in the form presented by Mermin [39, 83]. The circuit diagram for this is given in figure 5.2. This circuit construction, which uses four additional ancillary qubits, is not the most qubit-resource efficient fault-tolerant syndrome detection scheme but is easy to implement and understand. (For a more resource-efficient scheme, see [25, 123].) Table 5.2 gives the correspondence between the measurement results on the ancilla qubits in figure 5.2 and the error that was measured. Each controlled operation in figure 5.2 projects the system into the ±1 eigenspace of each of the stabilizer group generators, and the measurement on the corresponding ancilla tells into which of the two eigenspaces the state was projected. Since all of the Pauli operators are involutions, the correction operation is simply to apply the same Pauli operation indicated by the syndrome measurement.

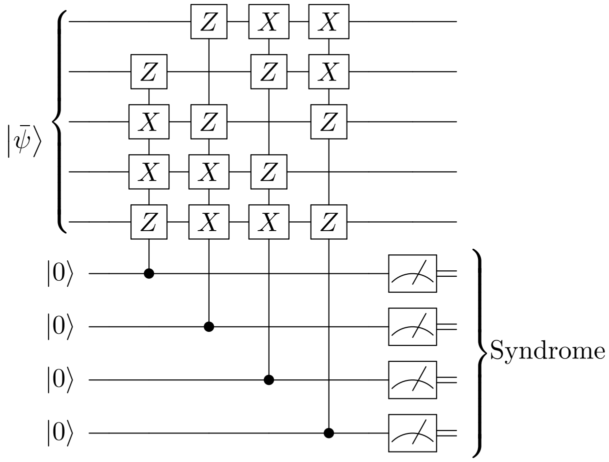

Figure 5.2: Circuit for fault tolerant error detection using the 5-qubit Perfect code. The encoding qubit are numbered 0 to 4 from top to bottom, and the ancilla qubits corresponding to the syndromes $M_0, \ldots, M_3$ are ordered from top to bottom as well. The mapping between the measurement results and corresponding errors is summarized in table 5.2.

Transverse (i.e., separable) gates are needed in order to implement fault-tolerant encoded gates on the encoded states. The 5-qubit Perfect code has transversal Pauli gates, with $\bar{\sigma}_m = \sigma_m^{\otimes 5}$, as well as a set of Clifford operations given by

$$K_{s_x,s_y,s_z} = \exp\left[\frac{i\pi}{3\sqrt{3}}\left(s_x X + s_y Y + s_z Z\right)\right] \text{ for } s_x, s_y, s_z \in \{-,+\} \tag{5.12}$$

that are also transversal, with $\bar{K}_{s_x,s_y,s_z} = K^{\otimes 5}_{s_x,s_y,s_z}$ [124]. This gives an easy way to implement a set of test gates with which to evaluate improved performance on our device. In the performance experiments described

Table 5.2: Syndrome-Error Correspondence for 5-Qubit Code

Syndrome $M_0M_1M_2M_3$	Error	Syndrome $M_0M_1M_2M_3$	Error
0000	No Error	1000	Z_2
0001	Z_1	1001	X_4
0010	X_3	1010	X_1
0011	Z_0	1011	Y_1
0100	X_0	1100	Z_3
0101	X_2	1101	Y_2
0110	Z_4	1110	Y_3
0111	Y_0	1111	Y_4

in section 5.4, the system is benchmarked using the Pauli Z and X gates as well as the Clifford SH gate. The SH gate is given by the product of the phase gate $S = \sqrt{Z}$ and the Hadamard gate $H = (X + Z)/\sqrt{(}2)$ and corresponds to $K_{+,+,+}$ in equation 5.12. Thus,

$$K_{+,+,+} = e^{i\pi/4} SH = \frac{1}{2} \begin{pmatrix} 1+i & 1+i \\ -1+i & 1-i \end{pmatrix} . \tag{5.13}$$

5.4 Experiments

To evaluate the performance of our hardware device we performed a series of tests to determine performance with and without the use of QEC protocols. We then compared the single-gate fidelity in each of the two cases using a random set of logical input states.

5.4.1 Experimental Design

The details of the hardware are described in the previous chapter. Two of the five encoding qubits were represented in the frequency domain using signals with four narrowband tonals at ±1000 Hz and ±3000 Hz. The other three qubits were represented in the time domain using a wavetrain of eight such signals [62]. (The classical signal representation requires time-frequency resources that will, of course, scale exponentially with the number of qubits.) Gate operations on frequency domain qubits were performed in hardware using analog filters, operational amplifiers, and four-quadrant multipliers. Likewise, the signal multiplication operations necessary for performing gates on the time-domain qubits was performed in hardware with the reordering operations handled digitally following an analog-to-digital converter (ADC). The configuration was chosen such that qubits 0 and 1 were represented in the frequency domain, while qubits 2 through 4 were represented in the time domain. The choice was arbitrary, and other configurations give similar results. For more information regarding the time domain encoding scheme and the corresponding gate operations see [62]. The general workflow of the experiments is detailed in the flowchart in figure 5.3.

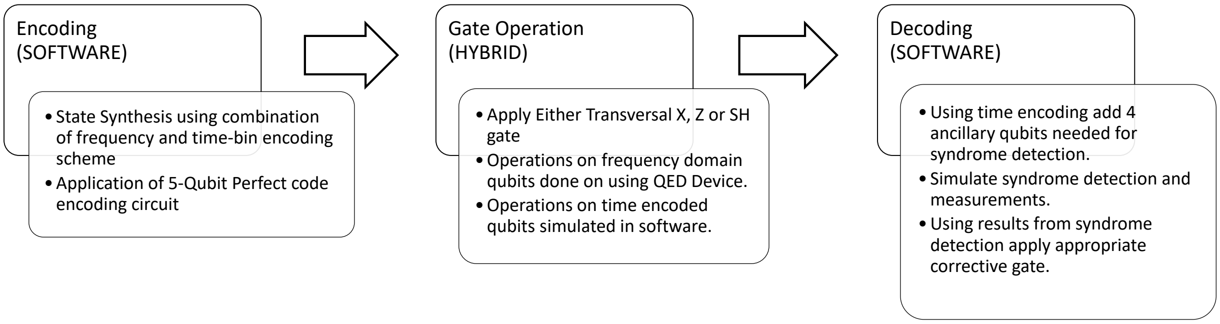

Figure 5.3: Flow-chart which describes general workflow for QEC experiment on QED.

The first stage of each of the experiments is a software pre-processing step in which we generate a set of 100 pure state inputs uniformly at random according to the Haar measure [86]. Each of these states is synthesized digitally and, in software, encoded into the 5-qubit code using the circuit given in figure 5.1. After this pre-processing stage, the physical analog signals are generated with a digital-to-analog converter (DAC), and a selected transversal gate is applied in hardware using analog electronics. The transformed signals are then sampled digitally using an ADC and buffered in memory. This digitized signal is converted back to the corresponding quantum state, upon which syndrome measurements may be performed using measurements based on the Born rule. Finally, a software-based post-processing stage occurs in which the transformed states have the syndrome detection circuit of figure 5.2 applied, along with the appropriate correction gate based on the syndrome measurement results as given in table 5.2. The decoding circuit is then applied (The circuit given in figure 5.1 but in reverse order) and the fidelity between the measured output state and the correct result is calculated. Note that only the encoded gate is performed in hardware — all encoding, error correction, and decoding is performed in software.

In addition to the encoded and error-corrected gate operations, a set of control runs was performed for each of the gates using the same set of input states and the same number of repetitions. This control run was performed directly on the one-qubit input states encoded in the frequency domain rather than on the logically encoded states.

5.4.2 Performance Metrics

A common metric used to quantify the performance of a quantum gate is the gate fidelity. Let $|\psi\rangle$ denote the notional input state for our gate, and let U denote the gate that we intend to apply. In practice what is actually implemented is a noisy version of U, which may be described by a quantum operation $\mathcal{E}$. The gate fidelity for a particular input state, defined as

$$F = \sqrt{\langle\psi|\, U^\dagger \, \mathcal{E}(|\psi\rangle\,\langle\psi|)\, U\, |\psi\rangle}\ , \tag{5.14}$$

measures how closely the noisy implementation of U approximates the desired one. A more general (input-independent) measure of the performance is the median gate fidelity, denoted $\bar{F}$, which is taken over an ensemble random input states and, for each one, several repetitions of a given gate operation. A median is preferred over the mean in order to characterize typical behavior in highly skewed data. Since fidelity is bounded above by 1, changes in the fidelity as a result of error-correction can be very small in absolute terms. The performance of a system in the long-term often has an exponential sensitivity to the infidelity $(1 - F)$ of the operations and, so, we define a metric that reflects this sensitivity, which we call the log-fidelity, denoted

f, and define it as

$$f = -\log_{10}(1 - F). \tag{5.15}$$

The choice of base 10 for the logarithm in equation 5.15 gives the log fidelity a simple interpretation in terms of a more common colloquial measure, the number of nines in the fidelity. As defined, the log-fidelity is equal to the number of nines plus an interpolation between an integer number of nines. We note that the definition of this measure draws analogy between the log-fidelity and the decibel scale used in classical systems for characterizing performance in terms of the signal-to-noise ratio (SNR). Use of the median fidelity also has the desirable property that median log-fidelity, $\bar{f}$, is equal to $-\log_{10}(1 - \bar{F})$, a property not shared by the mean fidelity.

5.4.3 Results

Starting with the Z gate we find that without QEC implemented, the median fidelity over the entire set of 100 input state randomizations and 1000 experimental runs was 0.99463 with an approximate 95% confidence interval of $(0.99460, 0.99467)$ obtained by bootstrapping over 10^4 random samples. Also useful for visualization of the performance statistics is the cumulative distribution function (cdf), which allows one to more easily compare the spread of the distributions. The results for the Z gate with QEC implemented tell a more interesting story. In figure 5.4 we compare the cdf and corresponding probability density functions (pdf) for the corrected and uncorrected Z gates. After error correction, it was found that the median fidelity for the Z gate increased to 0.9999764 $(0.9999761, 0.9999768)$. This was true despite the fact that the experimental error correction procedure tended to broaden the tail on the fidelity distribution, resulting in several outliers. This can be observed in the appearance of a bimodal clustering of low fidelity results that can be seen in the inset plot of figure 5.4. The reasons behind this tail broadening behavior will be expanded on further in section 5.5. Looking at the log-fidelities given in figure 5.4 shows, however, that despite the

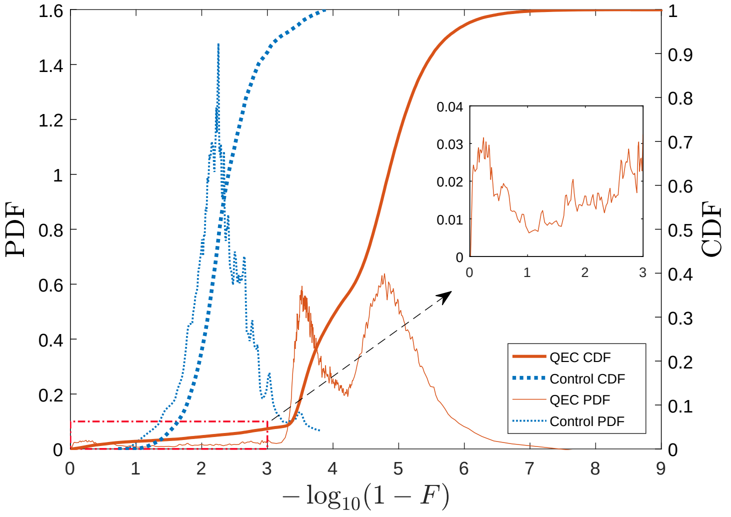

Figure 5.4: Plots of the cdf and pdf for the Z gate log-fidelity over all randomized input states and experimental realizations. The inset figure shows a zoomed-in section of the error-corrected data set's pdf within the log-fidelity range $[0, 4]$.

fact that QEC has a tendency to broaden the tails by periodically causing low fidelity outcomes, most of the time the procedure substantially improves the performance. This is further evidenced by looking at the change in the median log-fidelity, where we find, without error correction, the median log-fidelity for the Z gate is 2.270 $(2.267, 2.273)$ and, with error-correction, it improves to 4.628 $(4.622, 4.634)$.

The X and SH gate results are similar to those found for the Z gate, and a summary of the results can be found in figures 5.5 and 5.6 respectively. In figure 5.5 it can be seen in both cases that we again have a tail broadening effect in the error-corrected results with a similar bimodal clustering of the low-fidelity outcomes. However, the vast majority of events demonstrate a substantial improvement. For the X gate, despite the tail broadening, the median fidelity after error correction, 0.999426 $(0.999423, 0.999429)$, was significantly higher than that of the uncorrected gate, which was found to be 0.99739 $(0.99736, 0.99743)$. The median log-fidelity after QEC was found to be 3.241 $(3.239, 3.243)$, as compared to 2.584 $(2.578, 2.590)$ without error correction. Likewise, for the SH gate, the median fidelity of the uncorrected SH gate was found to be 0.99527 (0.99524, 0.99530), which was improved to 0.9999055 (0.9999048, 0.9999061) with QEC. The median log-fidelity of the uncorrected SH gate was found to be 2.325 (2.322, 2.328); after QEC this increased to 4.024 (4.022, 4.027).

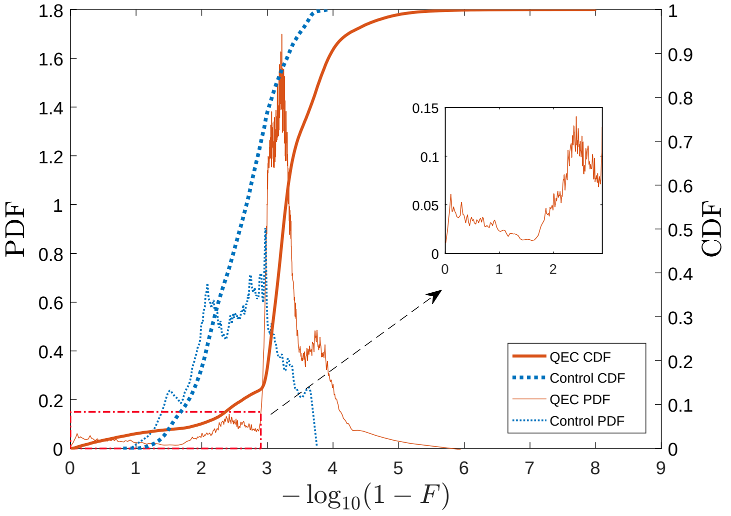

Figure 5.5: Plots of the cdf and pdf for the X gate log-fidelity over all randomized input states and all experimental realizations. The inset figure shows a zoomed-in section of the error-corrected data set's PDF within the log-fidelity range $[0, 4]$.

5.5 Discussion

One of the key issues raised by the experimental results with the application of QEC to the QED is the tail broadening effect that is observed on the fidelity. In order for QEC to be useful it is important to understand the conditions and noise processes which contribute this behavior. The device itself is subject to a myriad of classical noise sources including everything from Johnson noise, inherent to finite-temperature operation, to phase and frequency drift resulting from signal filtering in the gate and measurement operations. For the purposes of higher level modeling, however, it suffices to conceptually model the errors in the system as resulting from two main types of error. The first error source is gate errors caused by the

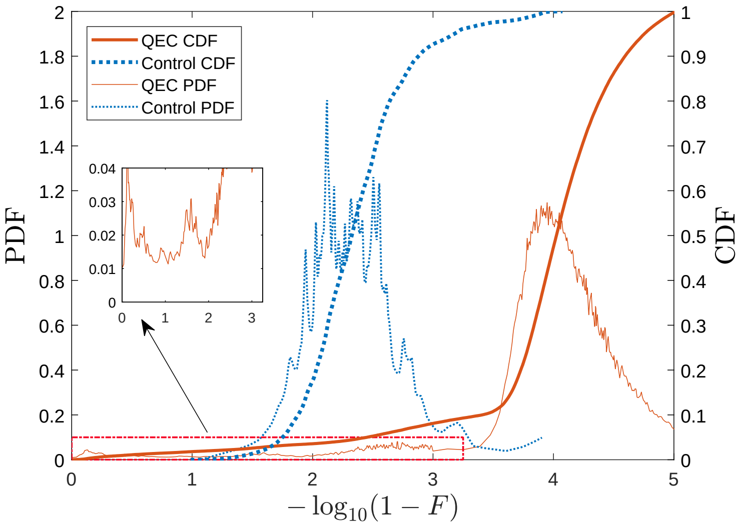

Figure 5.6: Plots of the cdf and pdf for the SH gate log-fidelity over all randomized input states and all experimental realizations. The inset figure shows a zoomed-in section of the error-corrected data set's PDF within the log-fidelity range $[0, 3.25]$.

imperfect implementation of the gate operations, and the second is due to general imperfections in the circuit construction, which puts a floor on the fidelity of our state representation even in the absence of any gate operation. Gate operations on the QED are implemented using analog multiplication operations with gate coefficients defined by a corresponding set of analog DC voltage values. The DC values that define the coefficients are inherently imperfect, however. Due to a combination of quantization error caused by the finite resolution of the digital-to-analog converters (DACs) and stochastic noise sources such as thermal noise, these DC values will fluctuate and be randomly distributed about the desired values. We suspect that different gates will have different fidelities due to the differing DC voltages needed to realize each in the hardware implementation. The Z gate, for example, has similiar DC voltages to an identity gate and would therefore be expected to perform better.

A key feature of all of the above noise processes is that they are inherently continuous, whereas the QEC corrections we apply are inherently discrete. In particular, codes such as the 5-qubit perfect code are constructed with a model in mind that is based on the idea that errors act on qubits within the state locally and independently. In cases where too many qubits are hit by the noise process it is possible to misidentify the error syndrome and in the correction process transform the state of the system into one nearly orthogonal to the original. From this we can see a likely candidate for the source of the bimodal clustering of low fidelity values in the experimental results presented in section 5.4.3. We can see a clear example of this in figure 5.4, where there are two modes of the QEC pdf at log-fidelities of about 3.5 and 5. This leaves open an interesting possibility for improving the performance of the QEC protocols in the device by designing decoding procedures which leverage the additional information we have access to from having an explicit representation of the state of the system and which performs corrections in a continuous manner. We explore this idea more directly in the context of applying QEC to wireless communication applications, and it is likely the ideas developed in that context would be similarly applicable to the QED device [73].

5.6 Conclusions

We have shown that the techniques of quantum error correction can be successfully applied in domains seemingly far removed from standard quantum mechanical systems. The QED device implements a classical representation of quantum states based on pairs of analog voltage signals to perform its information processing. As a classical device it is in principle subject to a whole myriad of errors, some of which, as in the case of AWGN, are representable as quantum operations. Yet, in practice, it is found that QEC nonetheless yields a practical performance boost. All three gates studied — the X, Z and SH gates — showed marked improvement in their operating characteristics, with an average increase in log-fidelity over the three gates of about 1.57. Given the general effectiveness of QEC at improving the device's performance it seems reasonable to suppose that in the above experiments the device is operating in a regime in which the errors are dominated by those in which there is a quantum analogue amenable to QEC, even if our models have not fully captured the details of those analogues yet. The results of this work may have applicability beyond computing and could serve as a basis for advanced techniques in robust, fault-tolerant classical communication through the use of quantum error correction protocols on classical messages.

Acknowledgements

This work was supported by the Office of Naval Research under Grant Nos. N00014-14-1-0323 and N00014-17-1-2107.

Chapter 6

Summary and Conclusions

In the first part of this dissertation we have explored the behavior of superconducting heterostructures, a field with deep connections to condensed matter physics, theoretical superconductivity, and the design and function of quantum information processing platforms. Tying all of our investigations together in the field of superconducting heterostructures has been the use of a scattering theory methodology based on the Bogoliubov-de Gennes equations, which describes the spectrum for quasiparticle excitations in spatially inhomogenous superconductors [35]. This, together with techniques modified from classic work by Demers and Griffin [36] as well as Blonder, Tinkham and Klapwijk [16], allowed us to study the local and nonlocal noise correlations without the application of the Andreev approximation and with material parameters in the high-T_c regime for the NSN and NSNSN geometries. This theory was developed in detail in Chapter 1.

In Chapter 2 we began by calculating the the full scattering matrix for a quasi-1D NSN geometry without the Andreev approximation applied (the exact expressions are in Appendix A). The scattering through an NSN geometry superconducting heterostructure is particularly interesting because of it's connection to the field of Cooper pair splitting devices, where the sign of the noise cross-correlations can indicate the presence of electron bunching and the generation of electronic entanglement. The scattering results were used to generate energy distributions for the local shot noise in the short, medium and long junction regimes where, because of the positivity of the noise correlations, we found signatures of electron anti-bunching in the left lead. For the energy distributions of the nonlocal noise correlations we found that, while overall the noise cross-correlations were negative, there were positive contributions from correlations between electrons and holes in the two normal leads. We also looked at the dependence of the total nonlocal shot noise, as well as its separate contributions, on the size of the central superconducting region finding a peak in the positive particle-hole contributions at short lengths.

In Chapter 3 we extended the scattering theory methods to the more complicated NSNSN geometry. The NSNSN geometry has not been widely studied in the superconducting heterostructure community, but introduces very interesting new features related to the presence of sub-gap quasibound states in the central normal region of the system. We began by again solving for the full scattering matrix of the system, without the application of the Andreev approximation. Resonances in the plots of the scattering elements show clear evidence for the presence of sub-gap quasibound states, which is further corroborated by the presence of scattering matrix poles in the complex energy domain. Additionally, we observed that for energies close to that of the quasibound states there was a substantial enhancement in the magnitude of the particle-hole transmission term (also, called crossed Andreev reflection) causing it to, for certain sets of parameters, become the largest transmission channel in the system. This already differs quite a bit from the results we obtained in Chapter 2, where we found the particle-hole transmission amplitude was an order of magnitude smaller than the normal transmission channels.

We used the scattering matrix elements to calculate the cross-correlated shot noise energy distributions and found a robust, one-to-one, correspondence between the energies of quasibound states and regions of positive correlations in the cross-correlated shot noise distributions. We then repeated this analysis using the Andreev approximation and found that the predicted cross-correlated noise distribution breaks down at the quasibound state energies. An analysis of the dependence of the magnitude of the positive noise cross-correlations on the size of the central normal and two superconducting regions was performed. Resultingly we found both the existence of a "sweet spot" for the size of the superconducting normal regions, as well as a periodic-like behavior of the positive noise correlations with the size of the central normal region. Finally, we studied what happened as you lowered the temperature of the system down to zero and found a crossover in the noise distributions between quasibound state dominated behavior at high and intermediate temperatures and the low-temperature limit where the positive correlations are instead related to a higher-order process called synchronized Andreev and inverse Andreev reflection.

In the second part of this dissertation I focused on work I performed related to the development of a special purpose signal-processing based hardware platform for performing quantum circuit simulation. In Chapter 4 we introduced the theoretical basis for this approach and the method for encoding the Hilbert space structure of a quantum circuit into the frequency domain of a complex analog voltage signal. We also introduced the mapping between gate operations and measurements in a quantum circuit and the corresponding signal-processing operations used to simulate them. Also in this chapter we presented experimental results based on an early two-qubit hardware prototype in which we measured the fidelity of performing state synthesis and the fidelity of random 1-qubit gate operations.

In Chapter 5 we explored whether we could make use of standard stabilizer-code based quantum error correction protocols for improving the performance of our prototype signal-processing based quantum simulation device. An important aspect was demonstrating that, at least for certain specific classical noise sources, it is possible to map the noise in the underlying classical hardware to a corresponding quantum channel in our simulation which is amenable to correction using standard QEC codes. For our experiments measuring the performance of this approach, we used the 5-qubit perfect code to encode a state, performed a transversal gate operation, and then digitized our signal and performed syndrome detection as a post-processing step. We found an improvement in the median fidelity of 1 to 2 orders of magnitude, depending on the particular gate we applied. The results of this work inspired us to look beyond just applications in computing and informed our investigations into the applications of the theory of quantum error correction for the development of new coding schemes for performing channel-blind wireless classical communication [73].

Appendices

A NSN Junction Transmission and Reflection Amplitudes

$$
\begin{aligned}
r_{pp}^{LL} = & -\frac{1}{\mathrm{DEN}}\Big[8k_hk_pu_o^2v_o^2(q_h^L-q_p^L)(q_h^R+q_p^R) \\
& + e^{iL_Sk_h-iL_Sk_p}\left(u_o^2P_{hh}^LM_{pp}^L-v_o^2P_{hp}^LM_{ph}^L\right)\left(u_o^2P_{hh}^RP_{pp}^R-v_o^2M_{hp}^RM_{ph}^R\right) \\
& + e^{iL_Sk_h+iL_Sk_p}\left(\mathrm{vo}^2P_{hp}^LP_{ph}^L-u_o^2P_{hh}^LP_{pp}^L\right)\left(u_o^2P_{hh}^RM_{pp}^R-v_o^2M_{hp}^RP_{ph}^R\right) \\
& + e^{-iL_Sk_h-iL_Sk_p}\left(v_o^2M_{hp}^LM_{ph}^L-u_o^2M_{hh}^LM_{pp}^L\right)\left(u_o^2M_{hh}^RP_{pp}^R-v_o^2P_{hp}^RM_{ph}^R\right) \\
& + e^{iL_Sk_p-iL_Sk_h}\left(u_o^2M_{hh}^LP_{pp}^L-v_o^2M_{hp}^LP_{ph}^L\right)\left(u_o^2M_{hh}^RM_{pp}^R-v_o^2P_{hp}^RP_{ph}^R\right)\Big]
\end{aligned}
\tag{1}
$$

where $P_{y,z}^X = k_y + q_z^X$ and $M_{y,z}^X = k_y - q_z^X$, where $X = L, R$, $y = p, h$ and $z = p, h$. For example, $P_{p,h}^L = k_p + q_h^L$ and $M_{p,p}^R = k_p - q_p^R$.

$$
\begin{aligned}
r_{ph}^{LL} = & \frac{2u_ov_o}{\mathrm{DEN}}\sqrt{q_h^L}\sqrt{q_p^L}\Big[\,4k_hk_p(q_h^R+q_p^R)\left(u_o^2+v_o^2\right) \\
& + (k_h+k_p)e^{iL_Sk_p-iL_Sk_h}\left(u_o^2M_{hh}^RM_{pp}^R-v_o^2P_{hp}^RP_{ph}^R\right) \\
& + (k_h-k_p)e^{-iL_Sk_h-iL_Sk_p}\left(u_o^2M_{hh}^RP_{pp}^R-v_o^2P_{hp}^RM_{ph}^R\right) \\
& - (k_h+k_p)e^{iL_Sk_h-iL_Sk_p}\left(u_o^2P_{hh}^RP_{pp}^R-v_o^2M_{hp}^RM_{ph}^R\right) \\
& - (k_h-k_p)e^{iL_Sk_h+iL_Sk_p}\left(u_o^2P_{hh}^RM_{pp}^R-v_o^2M_{hp}^RP_{ph}^R\right)\Big]
\end{aligned}
\tag{2}
$$

$$
\begin{aligned}
r_{hp}^{LL} = & \frac{u_ov_o}{\mathrm{DEN}}\sqrt{q_h^L}\sqrt{q_p^L}\Big[8k_hk_p(q_h^R+q_p^R)\left(u_o^2+v_o^2\right) \\
& - 2(k_h-k_p)e^{iL_Sk_h+iL_Sk_p}\left(u_o^2P_{hh}^RM_{pp}^R-v_o^2M_{hp}^RP_{ph}^R\right) \\
& + 2(k_h+k_p)e^{iL_Sk_p-iL_Sk_h}\left(u_o^2M_{hh}^RM_{pp}^R-v_o^2P_{hp}^RP_{ph}^R\right) \\
& - 2(k_h+k_p)e^{iL_Sk_h-iL_Sk_p}\left(u_o^2P_{hh}^RP_{pp}^R-v_o^2M_{hp}^RM_{ph}^R\right) \\
& + 2(k_h-k_p)e^{-iL_Sk_h-iL_Sk_p}\left(u_o^2M_{hh}^RP_{pp}^R-v_o^2P_{hp}^RM_{ph}^R\right)\Big]
\end{aligned}
\tag{3}
$$

$$
\begin{aligned}
r_{hh}^{LL} = \frac{1}{\mathrm{DEN}}\Big[\; & 8k_h k_p u_o^2 v_o^2 (q_h^L - q_p^L)(q_h^R + q_p^R) \\
& + e^{iL_S k_h + iL_S k_p} \left(v_o^2 M_{hp}^L M_{ph}^L - u_o^2 M_{hh}^L M_{pp}^L\right)\left(u_o^2 P_{hh}^R M_{pp}^R - v_o^2 M_{hp}^R P_{ph}^R\right) \\
& + e^{iL_S k_p - iL_S k_h} \left(u_o^2 P_{hh}^L M_{pp}^L - v_o^2 P_{hp}^L M_{ph}^L\right)\left(u_o^2 M_{hh}^R M_{pp}^R - v_o^2 P_{hp}^R P_{ph}^R\right) \\
& + e^{iL_S k_h - iL_S k_p} \left(u_o^2 M_{hh}^L P_{pp}^L - v_o^2 M_{hp}^L P_{ph}^L\right)\left(u_o^2 P_{hh}^R P_{pp}^R - v_o^2 M_{hp}^R M_{ph}^R\right) \\
& + e^{-iL_S k_h - iL_S k_p} \left(v_o^2 P_{hp}^L P_{ph}^L - u_o^2 P_{hh}^L P_{pp}^L\right)\left(u_o^2 M_{hh}^R P_{pp}^R - v_o^2 P_{hp}^R M_{ph}^R\right)\Big]
\end{aligned} \tag{4}
$$

$$
\begin{aligned}
t_{pp}^{RL} = & \frac{4}{\mathrm{DEN}}\; \left(u_o^2 - v_o^2\right)\sqrt{q_p^L}\sqrt{q_p^R} \\
& \times\Big(e^{iL_S k_p - iL_S q_p^R}\; k_h\; v_o^2 P_{ph}^L P_{ph}^R \;- e^{iL_S k_h - iL_S q_p^R}\; k_p\; u_o^2 P_{hh}^L P_{hh}^R \\
& + e^{-iL_S k_h - iL_S q_p^R}\; k_p\; u_o^2 M_{hh}^L M_{hh}^R - e^{-iL_S k_p - iL_S q_p^R}\; k_h\; v_o^2 M_{ph}^L M_{ph}^R\Big)
\end{aligned} \tag{5}
$$

$$
\begin{aligned}
t_{ph}^{RL} = & \frac{4}{\mathrm{DEN}}\; \sqrt{q_h^L}\sqrt{q_p^R}\; u_o v_o \left(u_o^2 - v_o^2\right) \\
& \Big(- e^{iL_S k_h - iL_S q_p^R}\; k_p\; M_{hp}^L P_{hh}^R \;+ e^{iL_S k_p - iL_S q_p^R}\; k_h\; M_{pp}^L P_{ph}^R \\
& + e^{-iL_S k_h - iL_S q_p^R}\; k_p\; P_{hp}^L M_{hh}^R \;- e^{-iL_S k_p - iL_S q_p^R}\; k_h\; P_{pp}^L M_{ph}^R\Big)
\end{aligned} \tag{6}
$$

$$
\begin{aligned}
t_{hp}^{RL} = & \frac{4}{\mathrm{DEN}}\; \sqrt{q_p^L}\sqrt{q_h^R} u_o v_o \left(u_o^2 - v_o^2\right) \\
& \Big(- e^{iL_S k_h + iL_S q_h^R}\; k_p\; P_{hh}^L M_{hp}^R + e^{iL_S q_h^R - iL_S k_h}\; k_p\; M_{hh}^L P_{hp}^R \\
& + e^{iL_S k_p + iL_S q_h^R}\; k_h\; P_{ph}^L M_{pp}^R - e^{iL_S q_h^R - iL_S k_p}\; k_h\; M_{ph}^L P_{pp}^R\Big)
\end{aligned} \tag{7}
$$

$$
\begin{aligned}
t_{hh}^{RL} = & \frac{4}{\mathrm{DEN}}\; \sqrt{q_h^L}\sqrt{q_h^R}\left(u_o^2 - v_o^2\right) \\
& \Big(- e^{iL_S k_h + iL_S q_h^R}\; k_p\; v_o^2 M_{hp}^L M_{hp}^R \;+ e^{iL_S q_h^R - iL_S k_h}\; k_p\; v_o^2 P_{hp}^L P_{hp}^R \\
& + e^{iL_S k_p + iL_S q_h^R}\; k_h\; u_o^2 M_{pp}^L M_{pp}^R - e^{iL_S q_h^R - iL_S k_p}\; k_h\; u_o^2 P_{pp}^L P_{pp}^R\Big)
\end{aligned} \tag{8}
$$

The denominator DEN is given by

$$\begin{aligned} DEN =& 8k_h k_p u_o^2 v_o^2 (q_h^L + q_p^L)(q_h^R + q_p^R) \\ &+ e^{iL_S k_p - iL_S k_h} \left(P_{hp}^L P_{ph}^L v_o^2 - M_{hh}^L M_{pp}^L u_o^2\right) \left(M_{hh}^R M_{pp}^R u_o^2 - P_{hp}^R P_{ph}^R v_o^2\right) \\ &+ e^{iL_S k_h + iL_S k_p} \left(M_{pp}^L P_{hh}^L u_o^2 - M_{hp}^L P_{ph}^L v_o^2\right) \left(M_{pp}^R P_{hh}^R u_o^2 - M_{hp}^R P_{ph}^R v_o^2\right) \\ &+ e^{iL_S k_h - iL_S k_p} \left(M_{hp}^L M_{ph}^L v_o^2 - P_{hh}^L P_{pp}^L u_o^2\right) \left(P_{hh}^R P_{pp}^R u_o^2 - M_{hp}^R M_{ph}^R v_o^2\right) \\ &+ e^{-iL_S k_h - iL_S k_p} \left(M_{hh}^L P_{pp}^L u_o^2 - M_{ph}^L P_{hp}^L v_o^2\right) \left(M_{hh}^R P_{pp}^R u_o^2 - M_{ph}^R P_{hp}^R v_o^2\right) \end{aligned} \tag{9}$$

B Expressions for Scattering Coefficients and Noise for the NSNSN System Using the Andreev Approximation

In Equations 10 and 11 below we give the expressions for t_{pp}^{RL} and t_{hh}^{RL} respectively using the Andreev approximation.

$$t_{pp}^{RL} = -\frac{(u-v)^2(u+v)^2 e^{i((h_2+h_4)(k_h+k_p)+h_3(q_h+q_p)-h_4 q_p)}}{\text{Den}_{pp}} \tag{10}$$

$$t_{hh}^{RL} = -\frac{(u-v)^2(u+v)^2 e^{i(h_2(q_h+q_p)+h_3(k_h+k_p)+h_4 q_h+\phi)}}{\text{Den}_{hh}} \tag{11}$$

$$\begin{aligned}\text{Den}_{pp} =& u^2v^2\left(e^{i(h_2k_h)} - e^{i(h_2k_p)}\right)\left(e^{i(h_3k_p+h_4k_h)} - e^{i(h_3k_h+h_4k_p)}\right)e^{i(h_2q_h+h_3q_p+\phi)} \\ & - e^{i(h_2q_p+h_3q_h)}\left(u^2e^{i(h_2k_h)} - v^2e^{i(h_2k_p)}\right)\left(u^2e^{i(h_3k_p+h_4k_h)} - v^2e^{i(h_3k_h+h_4k_p)}\right)\end{aligned} \tag{12}$$

$$\begin{aligned}\text{Den}_{hh} =& u^2v^2\left(e^{i(h_2k_h)} - e^{i(h_2k_p)}\right)\left(e^{i(h_3k_p+h_4k_h)} - e^{i(h_3k_h+h_4k_p)}\right)e^{i(h_2q_h+h_3q_p)} \\ & - e^{i(h_2q_p+h_3q_h+\phi)}\left(u^2e^{i(h_2k_h)} - v^2e^{i(h_2k_p)}\right)\left(u^2e^{i(h_3k_p+h_4k_h)} - v^2e^{i(h_3k_h+h_4k_p)}\right)\end{aligned} \tag{13}$$

The expressions for the different contributions to the cross-correlated shot noise also simplify under the Andreev approximation due to the setting of $r_{pp}^{LL} = r_{hh}^{LL} = r_{pp}^{RR} = r_{hh}^{RR} = 0$ and $t_{hp}^{LR} = t_{ph}^{LR} = t_{hp}^{RL} = t_{hp}^{RL} = 0$

$$\text{S}_{pp}^{LR} = \frac{m_L m_R}{\pi^2\hbar^4} \int de\left[F_p^L N_P^L(-|r_{hp}^{LL}|^2 - 1)\ |t_{pp}^{RL}|^2 + F_p^R N^R + p(-|r_{hp}^{RR}|^2 - 1)|t_{pp}^{LR}|^2\right] \tag{14}$$

$$\text{S}_{hh}^{LR} = \frac{m_L m_R}{\pi^2\hbar^4} \int de\ \left[F_h^L N_h^L(-|r_{ph}^{LL}|^2 - 1)|t_{hh}^{RL}|^2 + F_h^R N_h^R(-|r_{ph}^{RR}|^2 - 1)(|t_{hh}^{LR}|^2)\right] \tag{15}$$

$$\mathrm{S}_{ph}^{LR} = \frac{m_L m_R}{\pi^2 \hbar^4} \int de \Big[-(F^L N^R + F^R N^L) \big(\mathrm{Re} \left[r_{ph}^{LL*} r_{hp}^{RR*} t_{hh}^{RL} t_{pp}^{LR} \right] + \mathrm{Re} \left[r_{hp}^{LL*} r_{ph}^{RR*} t_{pp}^{RL} t_{hh}^{LR} \ \right] \big) \Big] \tag{16}$$

Bibliography

[1] S. Aaronson, *Quantum computing since democritus*, Cambridge University Press, 2013.

[2] Scott Aaronson and Alex Arkhipov, *The computational complexity of linear optics*, Proceedings of the forty-third annual ACM symposium on Theory of computing, 2011, pp. 333–342.

[3] Scott Aaronson and Lijie Chen, *Complexity-theoretic foundations of quantum supremacy experiments*, arXiv preprint arXiv:1612.05903 (2016).

[4] Scott Aaronson and Sam Gunn, *On the classical hardness of spoofing linear cross-entropy benchmarking*, arXiv preprint arXiv:1910.12085 (2019).

[5] J. B. Altepeter, E. R. Jeffrey, and P. G. Kwiat, *Advances in atomic, molecular and optical physics*, vol. **52**, ch. Photonic State Tomography, Elsevier, 2006.

[6] MP Anantram and S Datta, *Current fluctuations in mesoscopic systems with andreev scattering*, Physical Review B **53** (1996), no. 24, 16390.

[7] AF Andreev, *Thermal conductivity of the intermediate state of superconductors II*, Sov. Phys. JETP **20** (1965), 1490.

[8] Takao Aoki, Go Takahashi, Tadashi Kajiya, Jun-ichi Yoshikawa, Samuel L Braunstein, Peter van Loock, and Akira Furusawa, *Quantum error correction beyond qubits.*, Nature Physics **5** (2009), 541.

[9] Riccardo Arpaia, Marco Arzeo, Shahid Nawaz, Sophie Charpentier, Floriana Lombardi, and Thilo Bauch, *Ultra low noise* $YBa_2Cu_3O_{7-\delta}$ *nano superconducting quantum interference devices implementing nanowires*, Applied Physics Letters **104** (2014), no. 7, 072603.

[10] Frank Arute, Kunal Arya, Ryan Babbush, Dave Bacon, Joseph C Bardin, Rami Barends, Rupak Biswas, Sergio Boixo, Fernando GSL Brandao, David A Buell, et al., *Quantum supremacy using a programmable superconducting processor*, Nature **574** (2019), no. 7779, 505–510.

[11] Holger Bartolf, Andreas Engel, Andreas Schilling, Konstantin Il'in, Michael Siegel, H-W Hübers, and A Semenov, *Current-assisted thermally activated flux liberation in ultrathin nanopatterned nbn superconducting meander structures*, Physical Review B **81** (2010), no. 2, 024502.

[12] J George Bednorz and K Alex Müller, *Possible high T_c superconductivity in the Ba La Cu O system*, Zeitschrift für Physik B Condensed Matter **64** (1986), no. 2, 189–193.

[13] CWJ Beenakker, *Three "universal" mesoscopic josephson effects*, Transport Phenomena in Mesoscopic Systems, Springer, 1992, pp. 235–253.

[14] P. Benioff, *The computer as a physical system: A microscopic quantum mechanical Hamiltonian model of computers as represented by Turing machines*, Journal of Statistical Physics **22** (1980), 563.

[15] Ya M Blanter and Markus Büttiker, *Shot noise in mesoscopic conductors*, Physics reports **336** (2000), no. 1-2, 1–166.

[16] GE Blonder, M Tinkham, and TM Klapwijk, *Transition from metallic to tunneling regimes in superconducting microconstrictions: Excess current, charge imbalance, and supercurrent conversion*, Physical Review B **25** (1982), no. 7, 4515.

[17] IV Borzenets, Y Shimazaki, GF Jones, Monica F Craciun, Saverio Russo, Michihisa Yamamoto, and Seigo Tarucha, *High efficiency cvd graphene-lead (Pb) cooper pair splitter*, Scientific reports **6** (2016), 23051.

[18] V Bouchiat, N Chtchelkatchev, D Feinberg, GB Lesovik, Th Martin, and J Torres, *Single-walled carbon nanotube–superconductor entangler: noise correlations and einstein–podolsky–rosen states*, Nanotechnology **14** (2002), no. 1, 77.

[19] Nicolas Boulant, Lorenza Viola, Evan M Fortunato, and David G Cory, *Experimental implementation of a concatenated quantum error-correcting code*, Physical Review Letters **94** (2005), 130501.

[20] P Burset, WJ Herrera, and A Levy Yeyati, *Microscopic theory of cooper pair beam splitters based on carbon nanotubes*, Physical Review B **84** (2011), no. 11, 115448.

[21] Piotr Busz, Damian Tomaszewski, and Jan Martinek, *Spin correlation and entanglement detection in cooper pair splitters by current measurements using magnetic detectors*, Phys. Rev. B **96** (2017), 064520.

[22] Markus Büttiker, *Scattering theory of current and intensity noise correlations in conductors and wave guides*, Physical Review B **46** (1992), no. 19, 12485.

[23] Markus Büttiker, *Reversing the sign of current-current correlations*, Quantum noise in mesoscopic physics, Springer, 2003, pp. 3–31.

[24] J Cayssol, *Crossed andreev reflection in a graphene bipolar transistor*, Physical review letters **100** (2008), no. 14, 147001.

[25] Rui Chao and Ben W Reichardt, *Quantum error correction with only two extra qubits*, Physical Review Letters **121** (2017), 050502.

[26] D. Chevallier, J. Rech, T. Jonckheere, and T. Martin, *Current and noise correlations in a double-dot cooper-pair beam splitter*, Phys. Rev. B **83** (2011), 125421.

[27] J Chiaverini et al., *Realization of quantum error correction*, Nature **432** (2004), 602.

[28] Nikolai M Chtchelkatchev, Gianni Blatter, Gordey B Lesovik, and Thierry Martin, *Bell inequalities and entanglement in solid-state devices*, Physical Review B **66** (2002), no. 16, 161320.

[29] Karen Y Constantinian, Gennady A Ovsyannikov, Igor V Borisenko, Jesper Mygind, and Niels F Pedersen, *Shot noise in YBCO bicrystal josephson junctions*, IEEE transactions on applied superconductivity **13** (2003), no. 2, 610–613.

[30] Karen Y Constantinian, Gennady A Ovsyannikov, Igor V Borisenko, Nubar G Pogosyan, Arsen A Hakhoumian, Pavel Yagoubov, Jesper Mygind, and Niels Falsig Pedersen, *Experimental study of noise and josephson oscillation linewidths in bicrystal YBCO junctions*, Superconductor Science and Technology **14** (2001), no. 12, 1035.

[31] Brian R. La Cour and Granville E. Ott, *Signal-based classical emulation of a universal quantum computer*, New J. Phys. **17** (2015), 053017.

[32] Julia Cramer, Norbert Kalb, M Adriaan Rol, Bas Hensen, Machiel S Blok, Matthew Markham, Daniel J Twitchen, Ronald Hanson, and Tim H Taminiau, *Repeated quantum error correction on a continuously encoded qubit by real-time feedback*, Nature Communications **7** (2016), 11526.

[33] JC Cuevas and M Fogelström, *Shot noise and multiple andreev reflections in d-wave superconductors*, Physical review letters **89** (2002), no. 22, 227003.

[34] Michel Cyrot and Davor Pavuna, *Introduction to superconductivity and high-T_c materials*, World Scientific Publishing Company, 1992.

[35] Pierre-Gilles De Gennes, *Superconductivity of metals and alloys*, CRC Press, 2018.

[36] Jacques Demers and Allan Griffin, *Scattering and tunneling of electronic excitations in the intermediate state of superconductors*, Canadian Journal of Physics **49** (1971), no. 3, 285–295.

[37] D. Deutsch, *Quantum theory, the Church-Turing principle and the universal quantum computer*, Proceedings of the Royal Society of London, Series A **400** (1985), no. 1818, 97–117.

[38] Guy Deutscher and Denis Feinberg, *Coupling superconducting-ferromagnetic point contacts by andreev reflections*, Applied Physics Letters **76** (2000), no. 4, 487–489.

[39] David P DiVincenzo and Peter W Shor, *Fault-tolerant error correction with efficient quantum codes*, Physical Review Letters **77** (1996), 3260.

[40] D. Dragoman and M. Dragoman, *Quantum-classical analogies*, Springer, 2004.

[41] Edgar A Duarte, Pedro A Quintero, Mark W Meisel, and Juan C Nino, *Electrospinning synthesis of superconducting BSCCO nanowires*, Physica C: Superconductivity **495** (2013), 109–113.

[42] Martina Flöser, *From local to non-local transport : Percolation in quantum hall systems, cross-correlations in superconducting hybrid structures*, Ph.D. thesis, The University of Grenoble, 10 2012.

[43] Axel Freyn, Martina Flöser, and Régis Mélin, *Positive current cross-correlations in a highly transparent normal-superconducting beam splitter due to synchronized andreev and inverse andreev reflections*, Physical Review B **82** (2010), no. 1, 014510.

[44] G. Fülöp, S. d'Hollosy, A. Baumgartner, P. Makk, V. A. Guzenko, M. H. Madsen, J. Nygård, C. Schönenberger, and S. Csonka, *Local electrical tuning of the nonlocal signals in a cooper pair splitter*, Phys. Rev. B **90** (2014), 235412.

[45] G. Fülöp, F. Domínguez, S. d'Hollosy, A. Baumgartner, P. Makk, M. H. Madsen, V. A. Guzenko, J. Nygård, C. Schönenberger, A. Levy Yeyati, and S. Csonka, *Magnetic field tuning and quantum interference in a cooper pair splitter*, Phys. Rev. Lett. **115** (2015), 227003.

[46] JA Celis Gil, William J Herrera, et al., *Noise cross-correlation and cooper pair splitting efficiency in multi-teminal superconductor junctions*, Solid State Communications **258** (2017), 25–32.

[47] Dmitry S. Golubev and Andrei D. Zaikin, *Cross-correlated shot noise in three-terminal superconducting hybrid nanostructures*, Phys. Rev. B **99** (2019), 144504.

[48] Craig S Hamilton, Regina Kruse, Linda Sansoni, Sonja Barkhofen, Christine Silberhorn, and Igor Jex, *Gaussian boson sampling*, Physical review letters **119** (2017), no. 17, 170501.

[49] Reinier W Heeres, Philip Reinhold, Nissim Ofek, Luigi Frunzio, Liang Jiang, Michel H Devoret, and Robert J Schoelkopf, *Implementing a universal gate set on a logical qubit encoded in an oscillator*, Nature Communications **8** (2017), 94.

[50] M Henny, Stefan Oberholzer, Christoph Strunk, T Heinzel, K Ensslin, M Holland, and C Schönenberger, *The fermionic hanbury brown and twiss experiment*, Science **284** (1999), no. 5412, 296–298.

[51] LG Herrmann, Fabien Portier, Patrice Roche, A Levy Yeyati, Takis Kontos, and Christoph Strunk, *Carbon nanotubes as cooper-pair beam splitters*, Physical review letters **104** (2010), no. 2, 026801.

[52] L Hofstetter, S Csonka, A Baumgartner, G Fülöp, S d'Hollosy, Jesper Nygård, and C Schönenberger, *Finite-bias cooper pair splitting*, Physical review letters **107** (2011), no. 13, 136801.

[53] Lukas Hofstetter, Sa Csonka, Jesper Nygård, and C Schönenberger, *Cooper pair splitter realized in a two-quantum-dot Y-junction*, Nature **461** (2009), no. 7266, 960–963.

[54] Xiao-Li Huang and Yuli V Nazarov, *Interaction-induced supercurrent in quantum hall setups*, Physical Review B **100** (2019), no. 15, 155411.

[55] SK Firoz Islam and Arijit Saha, *Amplification of cooper pair splitting current in a graphene-based cooper pair beam splitter geometry*, Phys. Rev. B **96** (2017), 125406.

[56] R. Jozsa, *Fidelity for mixed quantum states*, J. Mod. Optics **41** (1994), 2315.

[57] R. Jozsa and N. Linden, *On the role of entanglement in quantum-computational speed-up*, Proc. R. Soc. Lond. A **459** (2003), 2011–2032.

[58] Satoshi Kashiwaya and Yukio Tanaka, *Tunnelling effects on surface bound states in unconventional superconductors*, Reports on Progress in Physics **63** (2000), no. 10, 1641.

[59] Julian Kelly et al., *State preservation by repetitive error detection in a superconducting quantum circuit*, Nature **519** (2015), 66.

[60] Karl Kraus, *States, effects and operations: fundamental notions of quantum theory*, Springer, 1983.

[61] M Yu Kupriyanov and VF Lukichev, *Proximity effect in electrodes and the steady-state properties of josephson SNS structures*, Fizika Nizkikh Temperatur **8** (1982), no. 10, 1045–1052.

[62] B. R. La Cour, S. A. Lanham, and C. I. Ostrove, *Parallel quantum computing emulation*, 2018 IEEE International Conference on Rebooting Computing (McLean, VA, USA), IEEE, 2018.

[63] B. R. La Cour and E. C. G. Sudarshan, *Classical model for measurements of an entanglement witness*, Phys. Rev. A **92** (2015), 032302.

[64] Brian R. La Cour, *Quantum contextuality in the Mermin-Peres square: A hidden variable perspective*, Phys. Rev. A **79** (2009), 012102.

[65] Brian R. La Cour, *A locally deterministic, detector-based model of quantum measurement*, Foundations of Physics **44** (2014), no. 10, 1059–1084.

[66] Brian R La Cour and Corey I Ostrove, *Subspace projection method for unstructured searches with noisy quantum oracles using a signal-based quantum emulation device*, Quantum Information Processing **16** (2017), 7.

[67] Brian R La Cour, Corey I Ostrove, Granville E Ott, Michael J Starkey, and Gary R Wilson, *Classical emulation of a quantum computer*, International Journal of Quantum Information **14** (2016), 1640004.

[68] Brian R La Cour and Granville E Ott, *Signal-based classical emulation of a universal quantum computer*, New Journal of Physics **17** (2015), 053017.

[69] Raymond Laflamme, Cesar Miquel, Juan Pablo Paz, and Wojciech Hubert Zurek, *Perfect quantum error correcting code*, Physical Review Letters **77** (1996), 198.

[70] R Landauer and Th Martin, *Equilibrium and shot noise in mesoscopic systems*, Physica B: Condensed Matter **175** (1991), no. 1-3, 167–177.

[71] G De Lange, B Van Heck, A Bruno, D J Van Woerkom, A Geresdi, S R Plissard, E P A M Bakkers, A R Akhmerov, and L Dicarlo, *Realization of Microwave Quantum Circuits Using Hybrid Superconducting-Semiconducting Nanowire Josephson Elements*, Physical Review Letters **127002** (2015), no. September, 1–5.

[72] James S Langer and Vinay Ambegaokar, *Intrinsic resistive transition in narrow superconducting channels*, Physical Review **164** (1967), no. 2, 498.

[73] S. A. Lanham, T. C. Cuvelier, C. Ostrove, B. La Cour, G. Ott, and R. Heath Jr., *A noncoherent space-time code from quantum error correction*, 53$^{\text{rd}}$ Annual Conference on Information Science and Systems (CISS) (Baltimore, MD, USA), IEEE, 2019.

[74] T W Larsen, K D Petersson, F Kuemmeth, T S Jespersen, P Krogstrup, J Nygård, and C M Marcus, *Semiconductor-Nanowire-Based Superconducting Qubit*, Physical Review Letters **127001** (2015), no. SEPTEMBER, 1–5.

[75] Daniel A. Lidar and Todd A. Brun (eds.), *Quantum error correction*, Cambridge University Press, 2013.

[76] KK Likharev, *Superconducting weak links*, Reviews of Modern Physics **51** (1979), no. 1, 101.

[77] Nicholas E Litombe, AT Bollinger, Jennifer Eve Hoff n, and I Božović, *$La_{2-x}Sr_xCuO_4$ superconductor nanowire devices*, Physica C: Superconductivity and its Applications **506** (2014), 169–173.

[78] Chao-Yang Lu, Wei-Bo Gao, Jin Zhang, Xiao-Qi Zhou, Tao Yang, and Jian-Wei Pan, *Experimental quantum coding against qubit loss error*, Proceedings of the National Academy of Sciences **105** (2008), 11050.

[79] Kazumi Maki, *Introduction to d-wave superconductivity*, AIP Conference Proceedings, vol. 438, AIP, 1998, pp. 83–128.

[80] Andrew Martin and CJ Lambert, *Self-consistent current-voltage characteristics of superconducting nanostructures*, Physical Review B **51** (1995), no. 24, 17999.

[81] DE McCumber and BI Halperin, *Time scale of intrinsic resistive fluctuations in thin superconducting wires*, Physical Review B **1** (1970), no. 3, 1054.

[82] WL McMillan, *Theory of superconductor—normal-metal interfaces*, Physical Review **175** (1968), no. 2, 559.

[83] N David Mermin, *Quantum computer science: an introduction*, Cambridge University Press, 2007.

[84] G. J. Murphy, *c^*-algebras and operator theory*, Academic Press, New York, 1990.

[85] M. A. Nielsen and I. L. Chuang, *Quantum computation and quantum information*, Cambridge University Press, Cambridge, 2000.

[86] Michael A Nielsen and Isaac Chuang, *Quantum computation and quantum information*, 2002.

[87] Nissim Ofek et al., *Extending the lifetime of a quantum bit with error correction in superconducting circuits*, Nature **536** (2016), 441.

[88] William D Oliver, Jungsang Kim, Robert C Liu, and Yoshihisa Yamamoto, *Hanbury brown and twiss-type experiment with electrons*, Science **284** (1999), no. 5412, 299–301.

[89] Corey Ostrove and Linda E Reichl, *Local and nonlocal shot noise in high-tc superconducting nanowires*, Physica B: Condensed Matter **561** (2019), 79–89.

[90] Corey Ostrove and Linda E. Reichl, *Positive cross-correlated shot noise and quasibound states in an NSNSN geometry*, Physical Review B (Under Review).

[91] GA Ovsyannikov and KY Constantinian, *Josephson effect in cuprate superconducting structures*, Low Temperature Physics **38** (2012), no. 4, 333–340.

[92] Edwin Pednault, John A Gunnels, Giacomo Nannicini, Lior Horesh, and Robert Wisnieff, *Leveraging secondary storage to simulate deep 54-qubit sycamore circuits*, arXiv preprint arXiv:1910.09534 (2019).

[93] TB Pittman, BC Jacobs, and JD Franson, *Demonstration of quantum error correction using linear optics*, Physical Review A **71** (2005), 052332.

[94] Anthony Ralston, *Error detection and error correction in real-time digital computers*, 1957 Western Computer Proceedings, 1957, pp. 179–188.

[95] MD Reed, L Dicarlo, SE Nigg, L Sun, L Frunzio, SM Girvin, and RJ Schoelkopf, *Realization of three-qubit quantum error correction with superconducting circuits.*, Nature **482** (2012), 382.

[96] Diego Ristè, Stefano Poletto, M-Z Huang, Alessandro Bruno, Visa Vesterinen, O-P Saira, and Leonardo DiCarlo, *Detecting bit-flip errors in a logical qubit using stabilizer measurements*, Nature Communications **6** (2015), 6983.

[97] J Sánchez-Canizares and F Sols, *Self-consistent scattering description of transport in normal-superconductor structures*, Physical Review B **55** (1997), no. 1, 531.

[98] J Sánchez-Cañizares and F Sols, *Transport in normal–superconductor–normal structures with local conservation of current*, Physica B: Condensed Matter **252** (1998), no. 4, 304–311.

[99] J Sanchez-Canizares and F Sols, *Self-consistent theory of transport in quasi–one-dimensional superconducting wires*, Journal of low temperature physics **122** (2001), no. 1, 11–35.

[100] J Schindele, A Baumgartner, and C Schönenberger, *Near-unity cooper pair splitting efficiency*, Physical review letters **109** (2012), no. 15, 157002.

[101] Philipp Schindler, Julio T Barreiro, Thomas Monz, Volckmar Nebendahl, Daniel Nigg, Michael Chwalla, Markus Hennrich, and Rainer Blatt, *Experimental repetitive quantum error correction*, Science **332** (2011), 1059.

[102] Tobias Schwarz, Roman Wölbing, Christopher F Reiche, Benedikt Müller, Maria-José Martínez-Pérez, Thomas Mühl, Bernd Büchner, Reinhold Kleiner, and Dieter Koelle, *Low-noise $YBa_2Cu_3O_7$ nano-squids for performing magnetization-reversal measurements on magnetic nanoparticles*, Physical Review Applied **3** (2015), no. 4, 044011.

[103] P. W. Shor, *Algorithms for quantum computation: discrete logarithms and factoring*, 35th Annual Symposium on Foundations of Computer Science, 1994 Proceedings, 1994, pp. 124–134.

[104] P. W. Shor, *Scheme for reducing decoherence in quantum computer memory*, Physical Review A **52** (1995), R2493–R2496.

[105] Manfred Sigrist, *Introduction to unconventional superconductivity*, AIP Conference Proceedings, vol. 789, AIP, 2005, pp. 165–243.

[106] Martin Stehno, *Investigations of nonlocal transport and current noise in mesoscopic normal metal-superconductor hybrid structures*, Ph.D. thesis, University of Illinois at Urbana-Champaign, 2013.

[107] Francesco Tafuri and John R Kirtley, *Weak links in high critical temperature superconductors*, Reports on Progress in Physics **68** (2005), no. 11, 2573.

[108] Yukio Tanaka and Satoshi Kashiwaya, *Theory of tunneling spectroscopy of d-wave superconductors*, Physical review letters **74** (1995), no. 17, 3451.

[109] Yukio Tanaka and Satoshi Kashiwaya, *Theory of the josephson effect in d-wave superconductors*, Physical Review B **53** (1996), no. 18, R11957.

[110] M. W. Johnson *et al.*, *Quantum annealing with manufactured spins*, Nature **473** (2011), 194–198.

[111] Piotr Trocha and Ireneusz Weymann, *Spin-resolved andreev transport through double-quantum-dot cooper pair splitters*, Phys. Rev. B **91** (2015), 235424.

[112] Piotr Trocha and Kacper Wrześniewski, *Cross-correlations in a quantum dot cooper pair splitter with ferromagnetic leads*, Journal of Physics: Condensed Matter **30** (2018), no. 30, 305303.

[113] CC Tsuei and JR Kirtley, *Pairing symmetry in cuprate superconductors*, Reviews of Modern Physics **72** (2000), no. 4, 969.

[114] A. M. Turing, *On computable numbers, with an application to the Entscheidungsproblem*, Proceedings of the London Mathematical Society, Series 2 **42** (1936), 230–265.

[115] PC Van Son, H Van Kempen, and P Wyder, *Andreev reflection and geometrical resonance effects for a gradual variation of the pair potential near the normal-metal–superconductor interface*, Physical Review B **37** (1988), no. 10, 5015.

[116] M Veldhorst and Alexander Brinkman, *Nonlocal cooper pair splitting in a pSn junction*, Physical review letters **105** (2010), no. 10, 107002.

[117] G Wendin, *Quantum information processing with superconducting circuits: a review*, Reports on Progress in Physics **80** (2017), no. 10, 106001.

[118] Rainer Wesche, *Physical properties of high-temperature superconductors*, John Wiley & Sons, 2015.

[119] Kacper Wrześniewski, Piotr Trocha, and Ireneusz Weymann, *Current cross-correlations in double quantum dot based cooper pair splitters with ferromagnetic leads*, Journal of Physics: Condensed Matter **29** (2017), no. 19, 195302.

[120] Kai Xie, *Advanced digital and analog error correction codes*, Ph.D. thesis, Lehigh University, 2011.

[121] Ke Xu and James R Heath, *Long, highly-ordered high-temperature superconductor nanowire arrays*, Nano letters **8** (2008), no. 11, 3845–3849.

[122] A Levy Yeyati, FS Bergeret, A Martin-Rodero, and TM Klapwijk, *Entangled andreev pairs and collective excitations in nanoscale superconductors*, Nature Physics **3** (2007), no. 7, 455.

[123] Theodore J Yoder and Isaac H Kim, *The surface code with a twist*, Quantum **1** (2017), 2.

[124] Theodore J. Yoder, Ryuji Takagi, and Isaac L. Chuang, *Universal fault-tolerant gates on concatenated stabilizer codes*, Physical Review X **6** (2016), 031039.

[125] Jingfu Zhang, Raymond Laflamme, and Dieter Suter, *Experimental implementation of encoded logical qubit operations in a perfect quantum error correcting code*, Physical Review Letters **109** (2012), 100503.

[126] Han-Sen Zhong, Hui Wang, Yu-Hao Deng, Ming-Cheng Chen, Li-Chao Peng, Yi-Han Luo, Jian Qin, Dian Wu, Xing Ding, Yi Hu, et al., *Quantum computational advantage using photons*, Science **370** (2020), no. 6523, 1460–1463.